Supplementary Information

Switching effective oxygen reduction and evolution performance by controlled graphitization of a cobalt-nitrogen-carbon framework system

Srinivas Gadipelli,* Tingting Zhao, Stephen A. Shevlin and Zhengxiao Guo*

Department of Chemistry, University College London, 20 Gordon Street, London, WC1H 0AJ, UK.

*Corresponding authors: gsrinivasphys@gmail.com (SG) and z.x.guo@ucl.ac.uk (ZG)

List of Abbreviations

ORR	-Oxygen reduction reaction
OER	-Oxygen evolution reaction
SCNCS	-Self-modulated cobalt-nitrogen-carbon system
NPCs	-Nanoporous carbons
SSA	-Specific surface area
PSD	-Pore-size distribution
Vp	-Pore volume
MOFs	-Metal-organic frameworks
ZIFs	-Zeolitic imidazolate frameworks
Co_xZn_{100-x}–C	-Carbonized Co_xZn_{100-x}–ZIF–8
Co_xZn_{100-x}–Cxxx	-Carbonized Co_xZn_{100-x}–ZIF–8 at particular temperature, example 900 °C as Co_xZn_{100-x}–C900 (normally for 10 h carbonization period unless otherwise specified, example, 2 h carbonized sample is identified as Co_xZn_{100-x}–C900-2h)
Co/C	-Samples obtained under inert atmosphere carbonization
Co_3O_4/C (or NPCs)	-Samples obtained under controlled oxidation during carbonization
CoO(II)@Co/C	-Surface oxidized Co/C by post-synthesis hydrothermal treatment
PXRD	-Powder X-ray diffraction
XPS	-X-ray Photoemission spectroscopy
SEM	-Scanning electron microscopy
TEM	-Transmission electron microscopy
TG	-Thermogravimetry
CV	-Cyclic voltammetry
LSV	-Linear sweep voltammetry

Methods

Synthesis of Co_xZn_{100-x}-ZIF-8s: In a typical synthesis of Zn-ZIF-8 (or Co-ZIF-8, also called ZIF-67), 7.344 g of $Zn(NO_3)_2.6H_2O$ (or $Co(NO_3)_2.6H_2O$) was dissolved in a 500 ml methanol. Then, 8.106 g of 2-methyl imidazole was dissolved in another 500 ml methanol by adding ~4 ml of a moderator, 1-methylimidazole. The later solution was slowly added to the former in a 1 L wide mouth jar while stirring at room temperature. After a few minutes a milky (for Zn-ZIF-8) solution was formed from the clear solution of the precursors, which was then left for 24 h to settle. The top clear solution was drained out and the white (or purple in case of Co-ZIF-8) precipitates were collected by centrifugation with further methanol washing. All the as-synthesized ZIF-8 samples were dried for a day at 80 °C oven. The mixed metal Co/Zn-ZIF-8s were synthesized in a similar method but by replacing the portion of zinc-nitrate precursor with cobalt-nitrate. For example, the sample made with 10%, 25% and 50% by mass of the cobalt-nitrate replacing the zinc-nitrate (more precisely, for 10%: 0.7344 g of cobalt-nitrate + 6.6096 g of zinc -nitrate; for 25%: 1.836 g of cobalt-nitrate + 5.508 g of zinc-nitrate; for 50%: 3.672 g of cobalt-nitrate + 3.672 g of zinc-nitrate) are named as $Co_{10}Zn_{90}$-ZIF-8, $Co_{25}Zn_{75}$-ZIF-8 and $Co_{50}Zn_{50}$-ZIF-8, respectively. The sample yield was of over 2.2 g.

Synthesis of Co_xZn_{100-x}-C NPCs: In a carbonization process, a suitable amount, between (100–300) mg of Co_xZn_{100-x}-ZIF-8 was placed in an alumina boat (of 1 cm x 1 cm x 5 cm) and then transferred into a horizontal tube furnace. The furnace tube was closed with a gas feed through end seals and sample area was thoroughly purged with nitrogen. The nitrogen flow was maintained throughout the reaction. The carbonization between (700-1100) °C was carried out for (2 to 10) h at a given temperature after heating at 5 °C per min. The carbons obtained at different carbonization conditions were named as Co_xZn_{100-x}-Cy-z, where y (= 700, 800, 900, 1000 and 1100) and z, respectively represents the carbonization temperature in °C and time in h. All the samples for further characterizations were handled in ambient air without further chemical treatment or acid washing unless stated.

Synthesis of Co_3O_4/C NPCs: The Co_3O_4/C NPCs were synthesized in a similar way as Co_xZn_{100-x}-C NPCs, but with leaking a small amount of air during the synthesis. Note that the long-time air introduction would lead to loss of carbon due to gasification. Thus controlled oxidation has been carried out at limited time of 2 h and 5 h, maximum.

Hydrothermal treatment of Co_xZn_{100-x}-C NPCs, i.e., CoO@Co/C NPCs (named as Co_xZn_{100-x}-Cy-HTT): The carbonized samples were further subjected to a hydrothermal treatment with 20 ml water at 180 °C for 6 h to 30 h in a 50 ml capacity Teflon lined stainless steel autoclave.

Structure & Porosity Characterization: Powder X-ray diffraction (PXRD, on Stoe Stadi-P, Cu-K-alpha) was carried out by filling the sample in a 0.5 mm diameter borosilicate glass capillary under ambient conditions. Raman spectroscopy (514.5 nm laser, Renishaw) was carried out on hand pressed powder samples on a glass slide. X-ray Photoemission spectroscopy (XPS, on Al-K-alpha, Thermo Scientific) data, scanning electron microscopy

(SEM, Jeol) and transmission electron microscopy (TEM, Jeol) measurements were carried out on the samples supported on a carbon tape or a carbon coated copper TEM grid. The porosity and gas adsorption-desorption isotherms up to 1 bar were determined at 77 K and 298 K using liquid nitrogen and water bath, respectively, on a Quantachrome Autosorb-iQC. The specific surface area was measured from the 77 K N_2 isotherm in a relative pressure range between 0.01 and 0.2, according to the Brunauer-Emmett-Teller (BET) method. The QSDFT (quenched solid density functional theory) method with slit/cylindrical pores was applied to desorption isotherm (10^{-2} to 0.99, P/Po) to obtain pore size distribution and cumulative pore volume. The sample was degassed at 180 °C overnight under dynamic vacuum prior to the actual gas adsorption measurement. Combined thermogravimetric (TG, on Setsys from Setaram) and mass spectrometry (MS, on OmniStar from Pfeiffer Vacuum) up to 1000 °C measurements were carried out on a dry sample under Ar flow with a heating rate of 5 °C per min and isothermal step of 1 h at 1000 °C. The TG mass-loss was recorded after background correction to empty alumina crucible.

The TG measurements on as-synthesized NPCs were carried out under oxidative atmosphere, flowing air with a heating rate of 3 °C per min up to 700 °C. The cobalt mass concentration is estimated from the residual mass after complete burn-off the carbon.

Electrochemical Tests: All the tests were carried out using Autolab (Metrohm PGSTAT302N) electrochemical station, by a three electrode method with a glassy carbon rotating disk as working electrode, and (1×1) cm^2 Pt and Ag/AgCl/saturated KCl as counter and reference electrode, respectively in O_2 saturated (or N_2 purged) alkaline (0.1M KOH) or acidic (0.1M & 1.0M $HClO_4$) electrolyte at room temperature. The O_2 or N_2 saturation is maintained by continuous gas bubbling. All the measurements were carried out with a fixed catalyst deposition of ~0.28 mg cm^{-2} on a 3 mm dia (or area of 0.0707 cm^2) glassy carbon disk electrode (GCDE). The catalyst was prepared as follows; 2 mg of NPC sample was dispersed in a total 500 µl solution consisting 482 µl of deionized water plus 18 µl of Nafion (5% solution) under sonication. The sonication was carried out up to an hour to get uniform catalyst dispersion ink. Of which 5 µl was micropipetted and dropped on to a GCDE followed by drying at 60 °C oven prior to the electrochemical tests. All the electrochemical test results were reported with respect to the reference, Ag/AgCl. In all the cases CV (Cyclic Voltammetry) and LSV (Linear Sweep Voltammetry) curves were recorded with a voltage sweeping at 10 mV s^{-1} in the potential range of +0.2 V to −0.8 V for ORR and +0.2 V to +1.0 V for OER in a 0.1M KOH. Before actual measurements, the catalyst was subjected to a number of CV cycles until a stable CV was obtained. The stability (i vs t) tests were carried out at a fixed potential of −0.20 V for ORR and +0.70 & +0.75V for OER and the response current recorded against time up to 20 h in O_2 saturated 0.1M KOH. In case of $HClO_4$, the current vs time response curves were measured at +0.3 V. The ORR and OER LSV curves were measured at different disk rotating speeds in fixed intervals of (800, 1200, 1600 and 2000) rpm. The electron transfer number during ORR is estimated using Koutechy-Levich relation [ref. Sa3];

$$\frac{1}{J} = \frac{1}{J_L} + \frac{1}{J_K} = \frac{1}{B\omega^{1/2}} + \frac{1}{J_K}$$

$$B = 0.62nFC_0(D_0)^{2/3}v^{-1/6}$$

$$J_K = nFkC_0$$

J is the measured current density, J_L and J_K are diffusion and kinetic limiting current densities, respectively, ω is angular velocity, n is electron transfer number, F is Faraday constant (96485 C mol^{-1}), C_0 is O_2 bulk concentration (1.26×10^{-6} mol cm^{-3}), D_0 is O_2 diffusion coefficient in the electrolyte (1.9×10^{-5} cm^2 s^{-1}) and v is kinetic viscosity of 0.1M KOH (0.01 cm^2 s^{-1}).

B, basically a slope of a straight line is determined from the linear fittings of the plots from measured current density (inverse of it on the y-axis) in the equilibrium region, between −0.3 V to −0.8 V of ORR LSV curves at different disk rotating speed (in rad s^{-1} ; i.e., $\frac{2\pi}{60} \times rpm$; again inverse of it on the x-axis).

The measured potentials against Ag/AgCl is converted to RHE using the relation, In 0.1M KOH, V vs (RHE) = V vs (Ag/AgCl) + 0.95 V [Ref. Sa4].

The overpotential V = V vs (RHE) – 1.23 V.

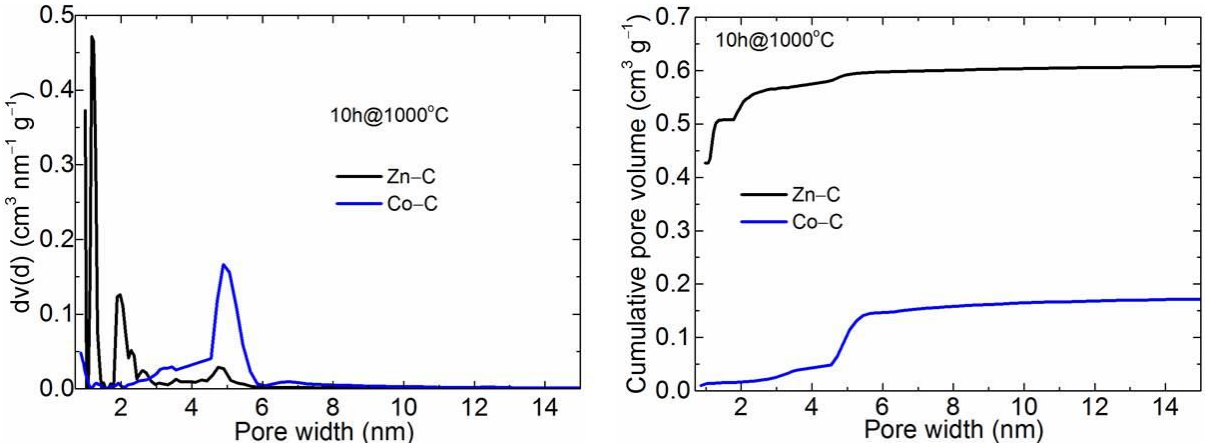

Figure S1. Pore-size distribution (left) and cumulative pore volume (right) plots of Zn_{100}-C1000 and Co_{100}-C1000. See that Zn_{100}-C1000 shows a highly microporous nature of carbon with most of the pores situated at ≤2 nm pore widths, whereas due to Co-induced graphitization Co_{100}-C1000 shows a smeared out porosity with a small fraction of mesopore development at pore width of ~5 nm.

Table S1. Porosity (BET specific surface area and total pore volume) of NPCs derived from ZIF-8 and ZIF-67 at different carbonization temperatures. See that both the ZIF-8 and -67 show similar porosity but compared to the ZIF-8 derived NPCs, ZIF-67 derived NPCs show a considerable reduction in the porosity with increased carbonization temperature. Also ZIF-67 NPCs are mesoporous in nature with a single pore width of ~5.0 nm than the high microporosity exhibited by ZIF-8 derived NPCs. Note that the increased porosity with temperature in ZIF-8 NPCs is attributed to the continuous decomposition of framework ligand together with Zn evaporation above 900 °C. Whereas, the catalytic Co-induced stitching of ligand carbons to crystallized graphitic structure leaves a largely smeared out open pore structure from ZIF-67. The post-synthesis acid etching of Co clusters results in a little improvement in the porosity.

Sample description	**BET Specific surface area (m^2 g^{-1})**	**Total pore volume (cm^3 g^{-1})**
ZIF-8	1795	0.746
Co-ZIF-8	1800	0.748
Zn_{100}-C900-6h	1330	0.578
Zn_{100}-C1000-10h	1455	0.671
Co_{100}-C900-6h	300	0.301
Co_{100}-C1000-10h	96	0.195
Co_{100}-C1000-10h-acid clean	212	1.086

Table S2. XPS elemental contents in Zn-ZIF-8 and Co-ZIF-8 derived carbons. Co_{100}-C shows high content of carbon.

Sample	**C (at%)**	**N (at%)**	**O (at%)**	**Co (at%)***	**Zn (at%)**
Co_{100}-C1000-10h	95.5	0.2	4.0	0.3	-
Zn_{100}-C1000-10h	86.0	5.5	9.0	-	0.5
Co_{100}-C900-6h	90.0	2.0	7.5	0.5	-
Zn_{100}-C900-6h	82.0	11.0	6.0	-	1.0

* Due to the formation of cobalt-core and carbon-shell the XPS cannot report true cobalt content in the samples, mainly because of the carbon shielding effect. But the actual cobalt-content in the carbonized samples is reported with thermogravimetric analysis at **Figure S10**.

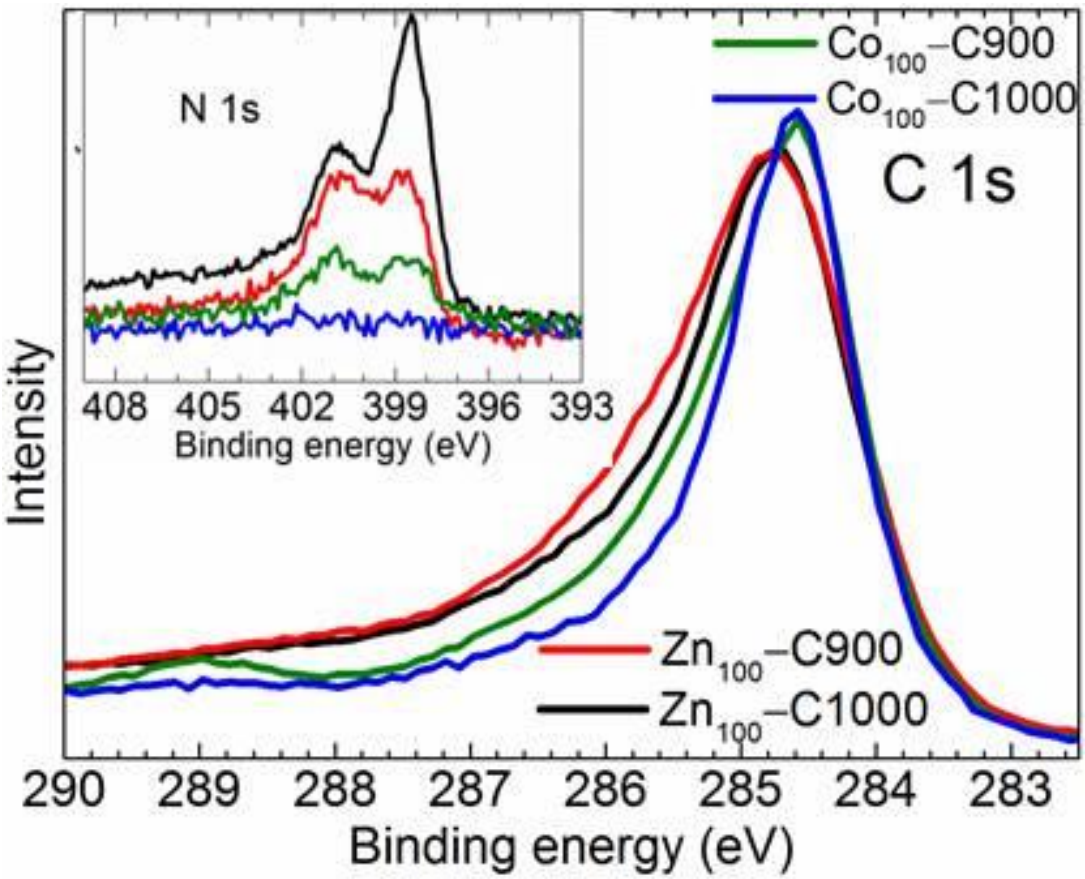

Figure S2. XPS C 1s and N 1s (inset) core level spectra of NPCs derived from ZIF–8 (Zn_{100}-C) and –67 (Co_{100}-C) alone at 900 °C for 6 h and 1000 °C for 10 h. The C 1s peak narrowing and shift to the low binding energy indicates the cobalt induced graphitization and loss of nitrogen content [Ref. Sa5]. The loss of nitrogen content is also clearly observed at N 1s spectra (inset). See **Table S2** for elemental composition.

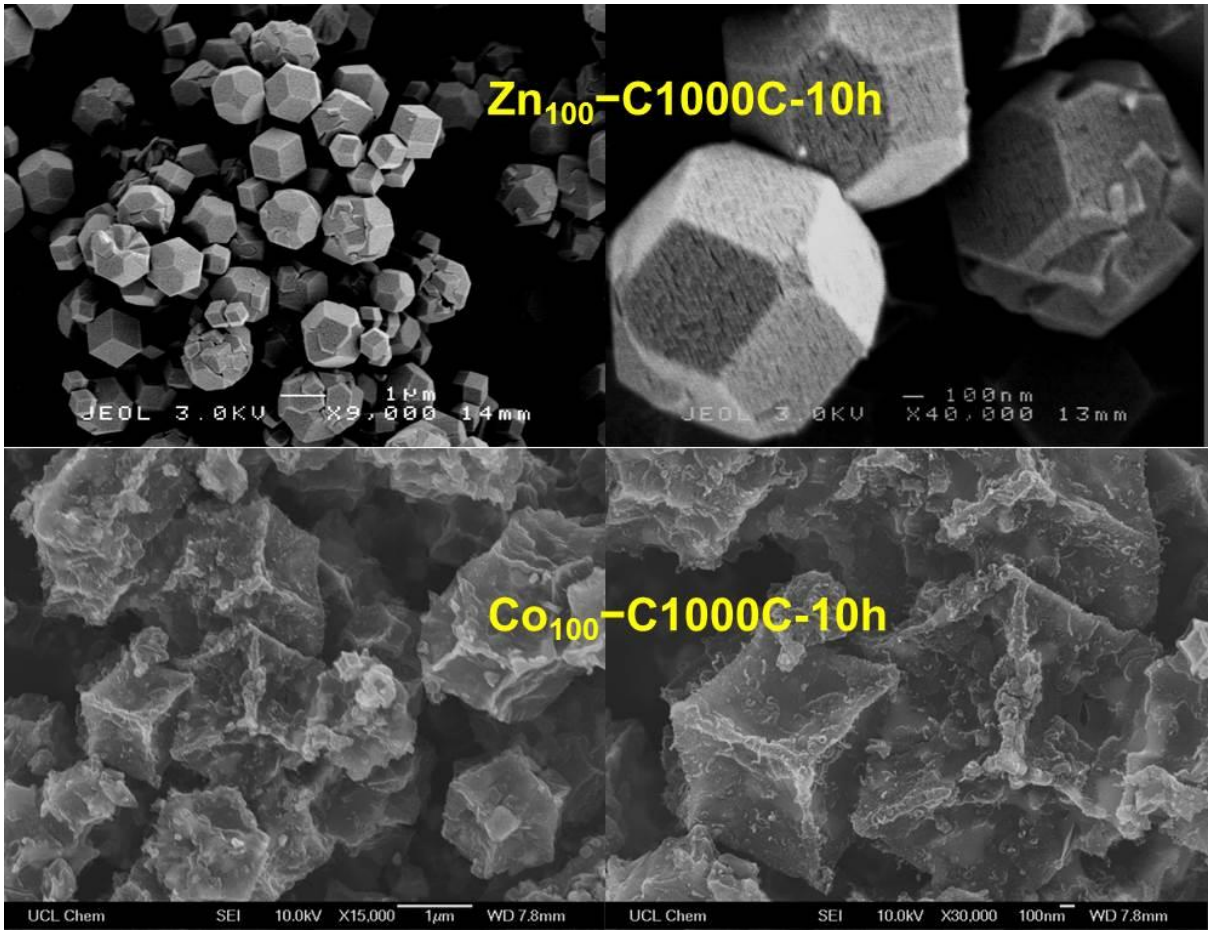

Figure S3. SEM images of NPCs derived at 1000 °C & 10 h carbonization of ZIF-8 (above) and ZIF-67 (below). Clearly, the structure and surface morphology of ZIF-8 crystals remains in its Zn_{100}-C1000; however the cobalt-induced graphitization is seen with considerable surface plane shrinkage of Co_{100}-C1000 crystallites. The left & right images are taken at different magnification levels.

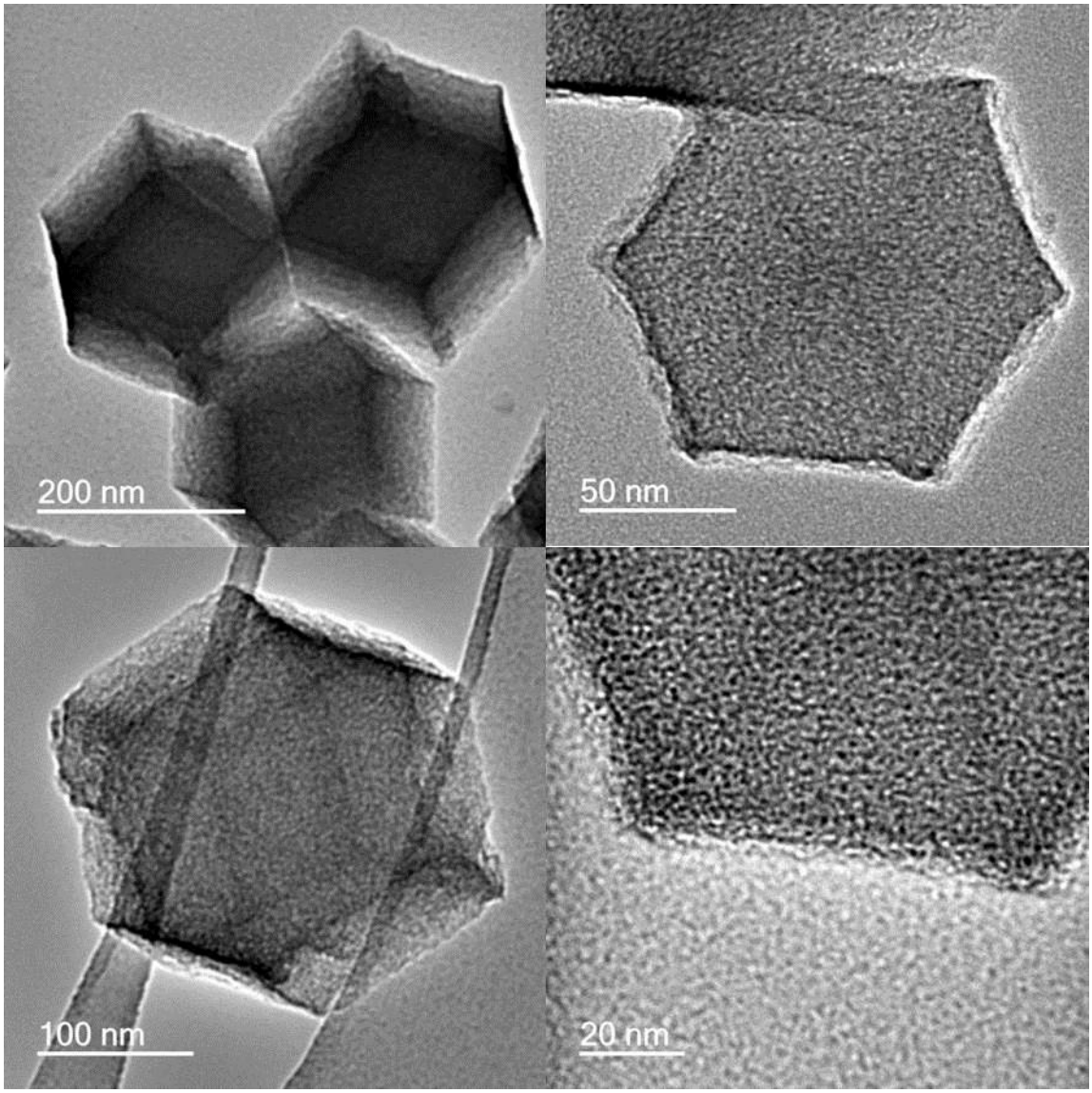

Figure S4. TEM images at different magnifications of NPCs derived at 1000 °C & 10 h carbonization of ZIF-8. See that carbon is highly microporous and amorphous in nature.

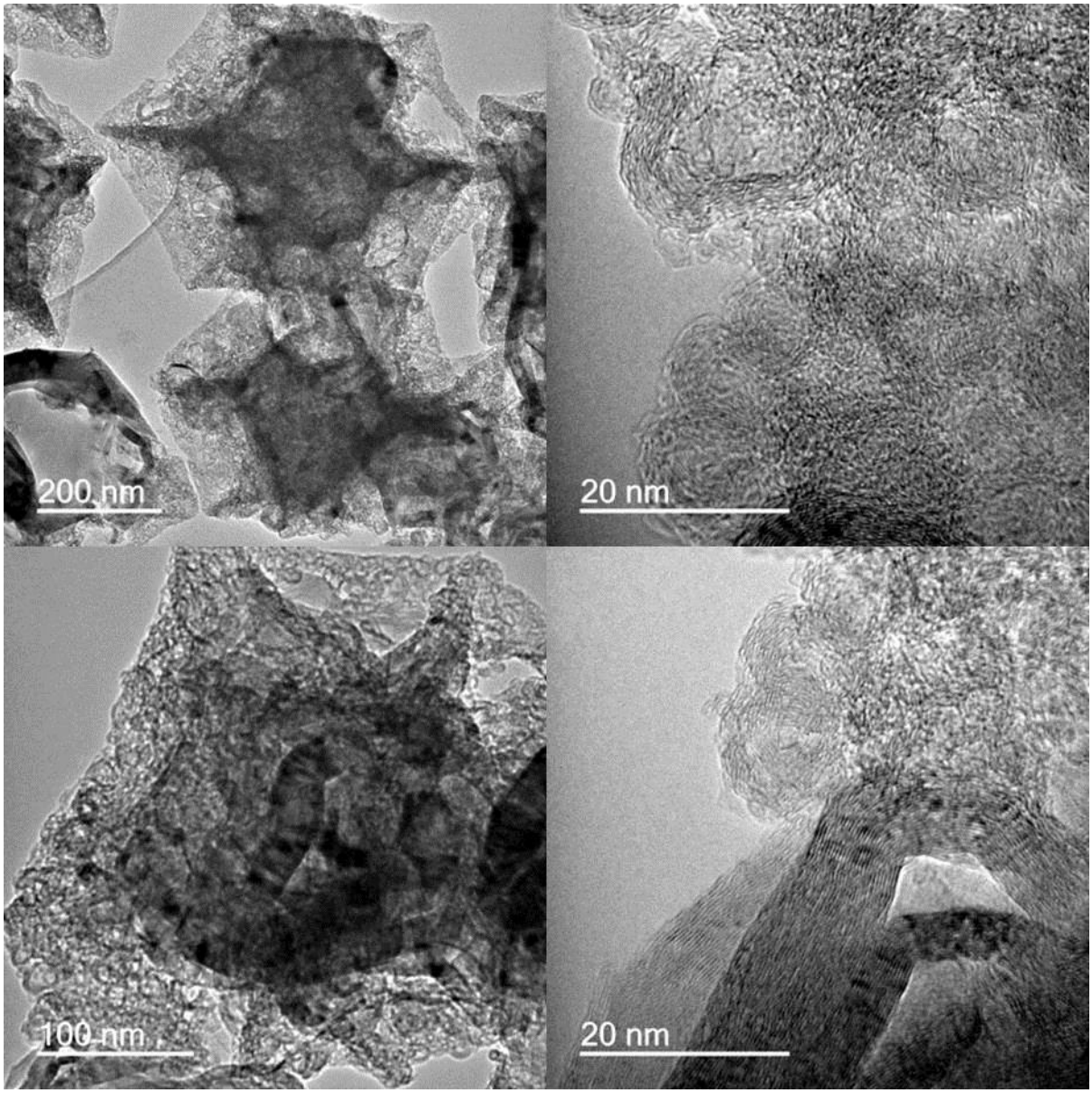

Figure S5. TEM images at different magnifications of NPCs after acid cleaning of magnetic cobalt clusters (these are not compatible for TEM measurement), derived at 1000 °C & 10 h carbonization of ZIF-67. See that a clear cobalt induced graphitization with the formation of a graphitic ribbon structures. The removal of cobalt clusters also leaves big pores.

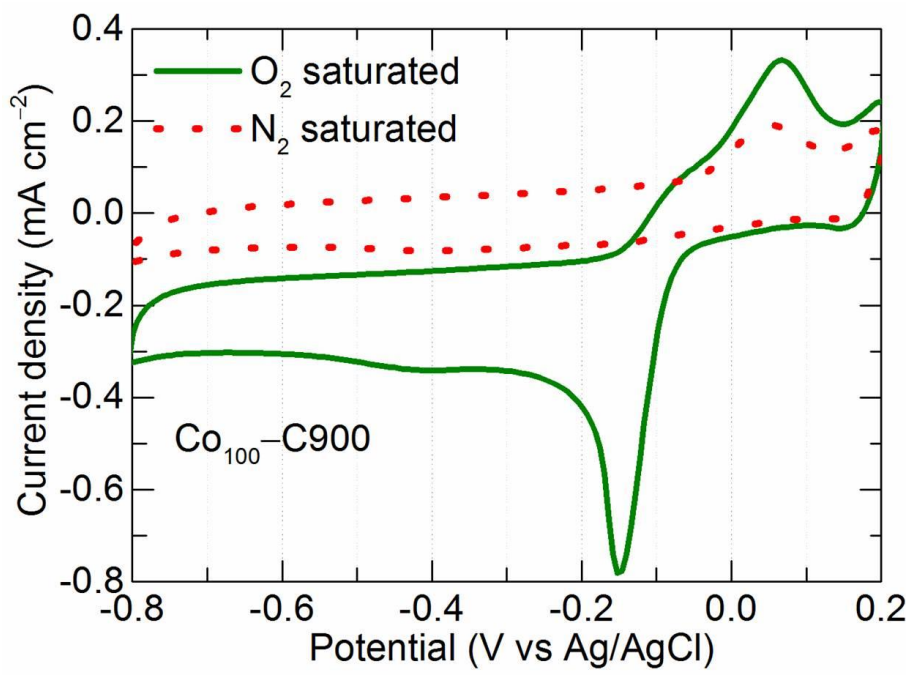

Figure S6. CV curves of Co_{100}-C900-6h, recorded in both O_2 and N_2 saturated 0.1M KOH electrolyte. See that ORR activity current peak is not observed in N_2 saturated electrolyte.

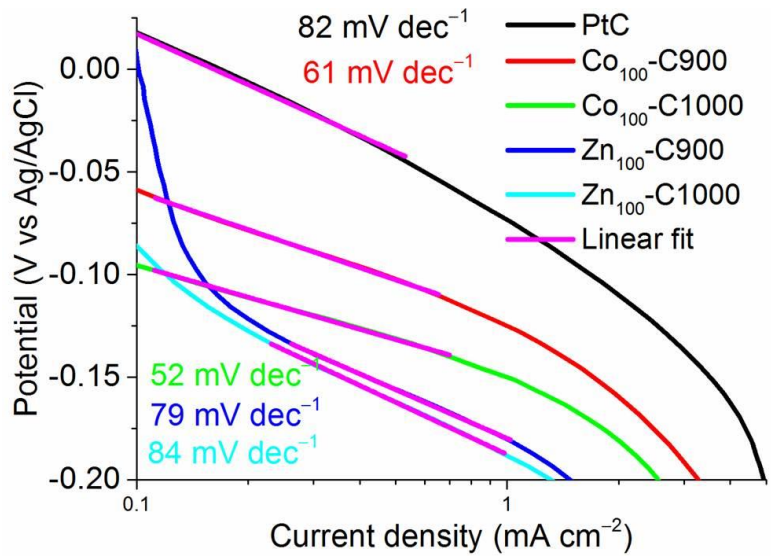

Figure S7. Tafel plots (applied potential vs log(current density)) of ZIF–8 and ZIF–67 derived NPCs at (900 & 1000) °C and (6 & 10) h, respectively with Pt/C standard. The Tafel slopes are identified with linear fittings in purple colour. See that both Co_{100}–C900 and Co_{100}–C1000 exhibit much smaller slopes, (61 & 52) mV decade^{-1} than Zn_{100}–NPCs and also Pt/C standard (82 mV decade^{-1}), indicating a fast reduction kinetics.

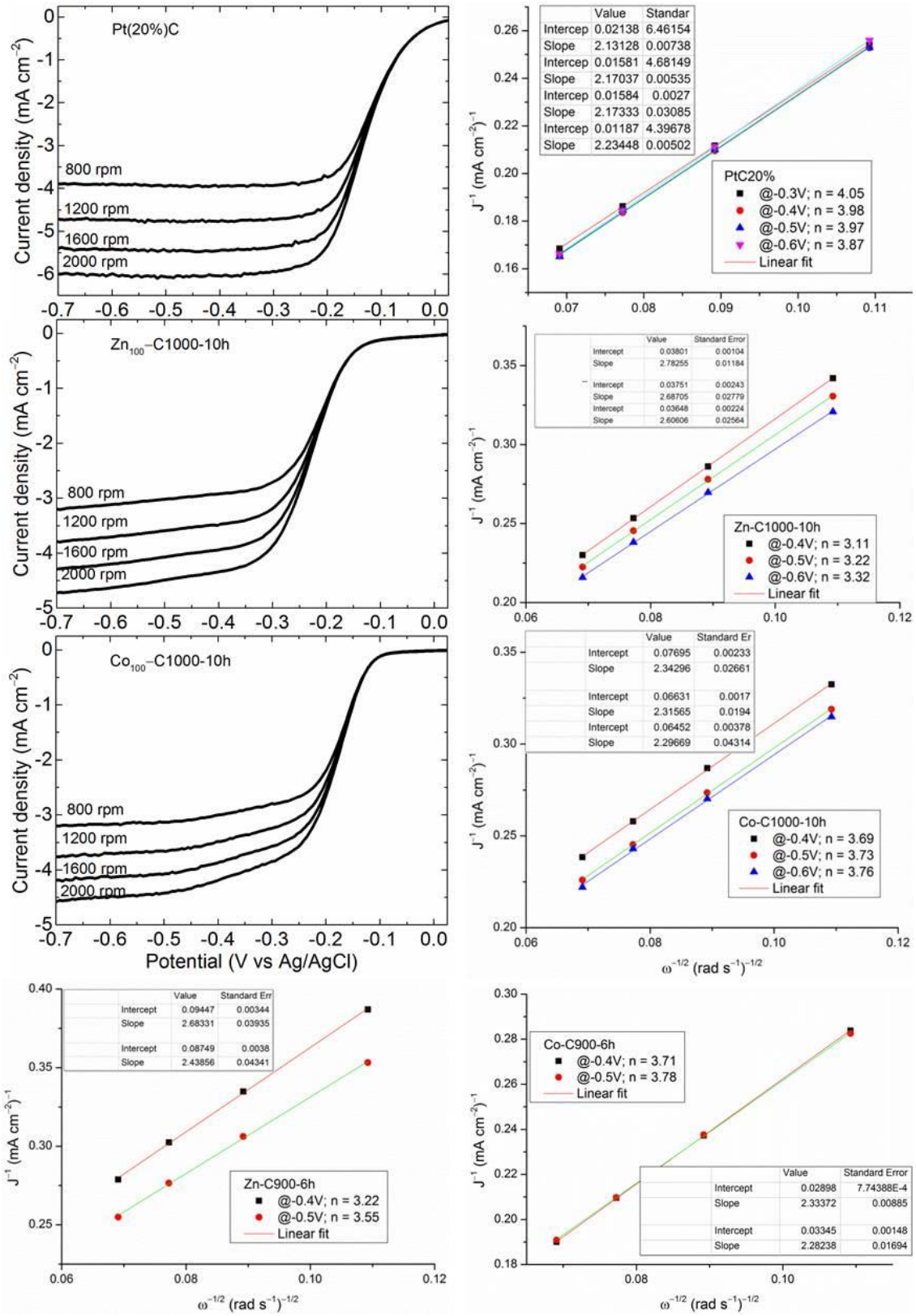

Figure S8. Top three: ORR LSV curves at different rotating speeds (left panel) and its derived Koutechy-Levich plot linear fittings (right panel) for Pt/C, Zn_{100}-C1000-10h and Co_{100}-C1000-10h. Bottom two: shows Koutechy-Levich plot linear fittings for Zn_{100}-C900-6h and Co_{100}-C900-6h. The calculated electron transfer number, n at different potentials between −(0.3-0.6) V vs Ag/AgCl is given in each plot.

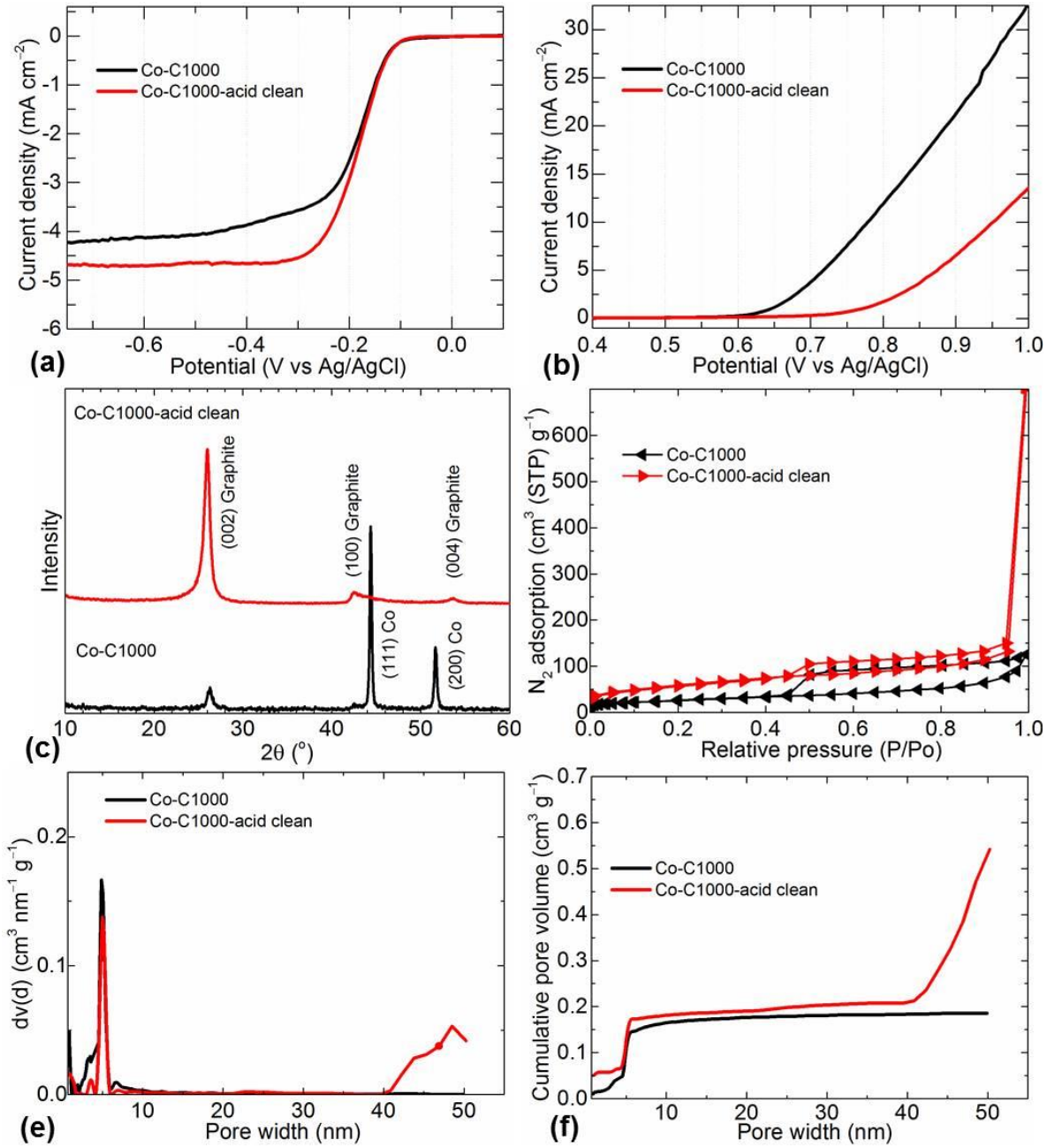

Figure S9. Comparative characteristics of Co_{100}-C1000-10h; as synthesized (black data) and acid clean to remove cobalt (red data). a) LSV curves of ORR show enhancement in the limiting current density after acid etching out the cobalt, no change in both onset potential and slope of reduction is seen. b) LSV curves of OER show considerable decrease in the current density and increased onset potential after etching out the cobalt. c) PXRD pattern of acid etching sample is reminiscent of graphitic structure, without any traces of crystalline cobalt as observed in as synthesized one. d) Isotherm shows enhanced uptake of N_2 (77 K) after acid etching of cobalt indicating the enhanced porosity, specifically at higher relative pressure is attributed to a removal of cobalt clusters in the structure. e) Pore size distribution shows that new pore development at or above 40 nm pore width. f) Cumulative pore volume shows considerably enhanced pore volume at pore widths above 40 nm. d-f) Indicating that the crystalline cobalt clusters are in the size of ≥40 nm.

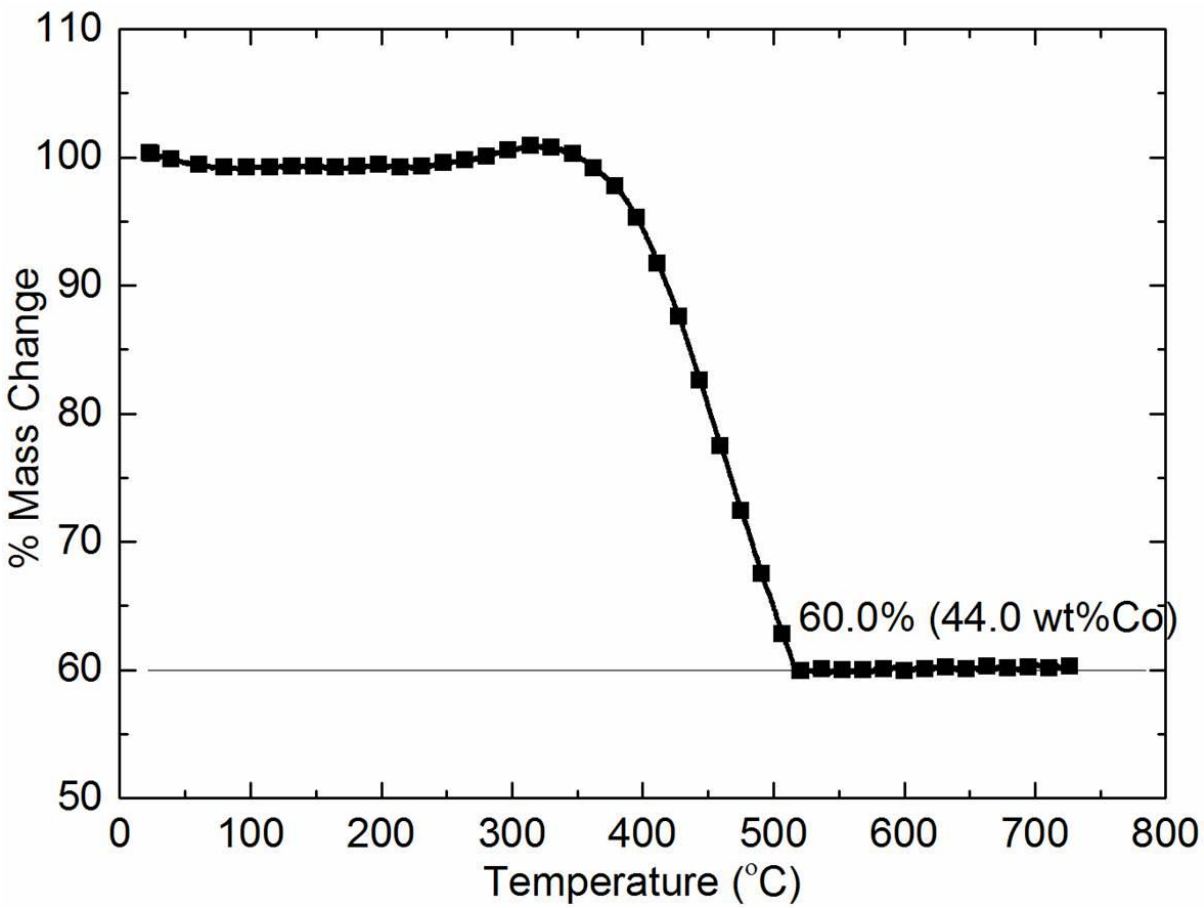

Figure S10. TG analysis plot of Co_{100}–C1000-10h. The measurement was carried out in a flowing air to burnout the carbon to get true cobalt concentration that is embedded in the carbon matrix. The residual weight at above 500 °C corresponds to the Co_3O_4 (assuming complete transformation of the cobalt metal into oxide). Thus the cobalt-metal content is calculated accordingly.

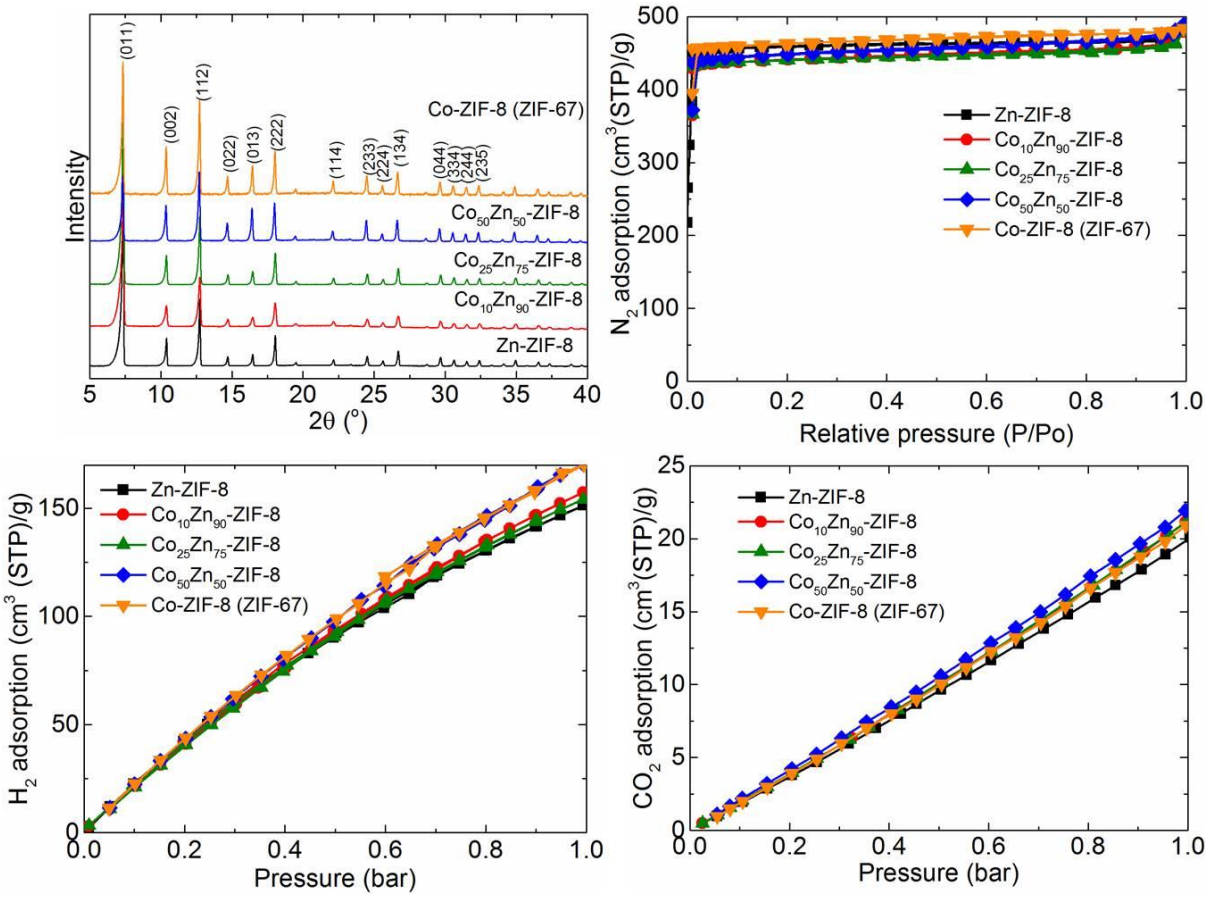

Figure S11. PXRD patterns (top left), 77 K N_2 sorption isotherms (top right), 77 K H_2 uptake isotherms (bottom left) and 298 K CO_2 uptake isotherms (bottom right) of precursor ZIF-8s; Co_xZn_{100-x}-ZIF-8 with x = 100, 50, 25, 10 and 0. All are characteristics of isostructural framework crystalline samples.

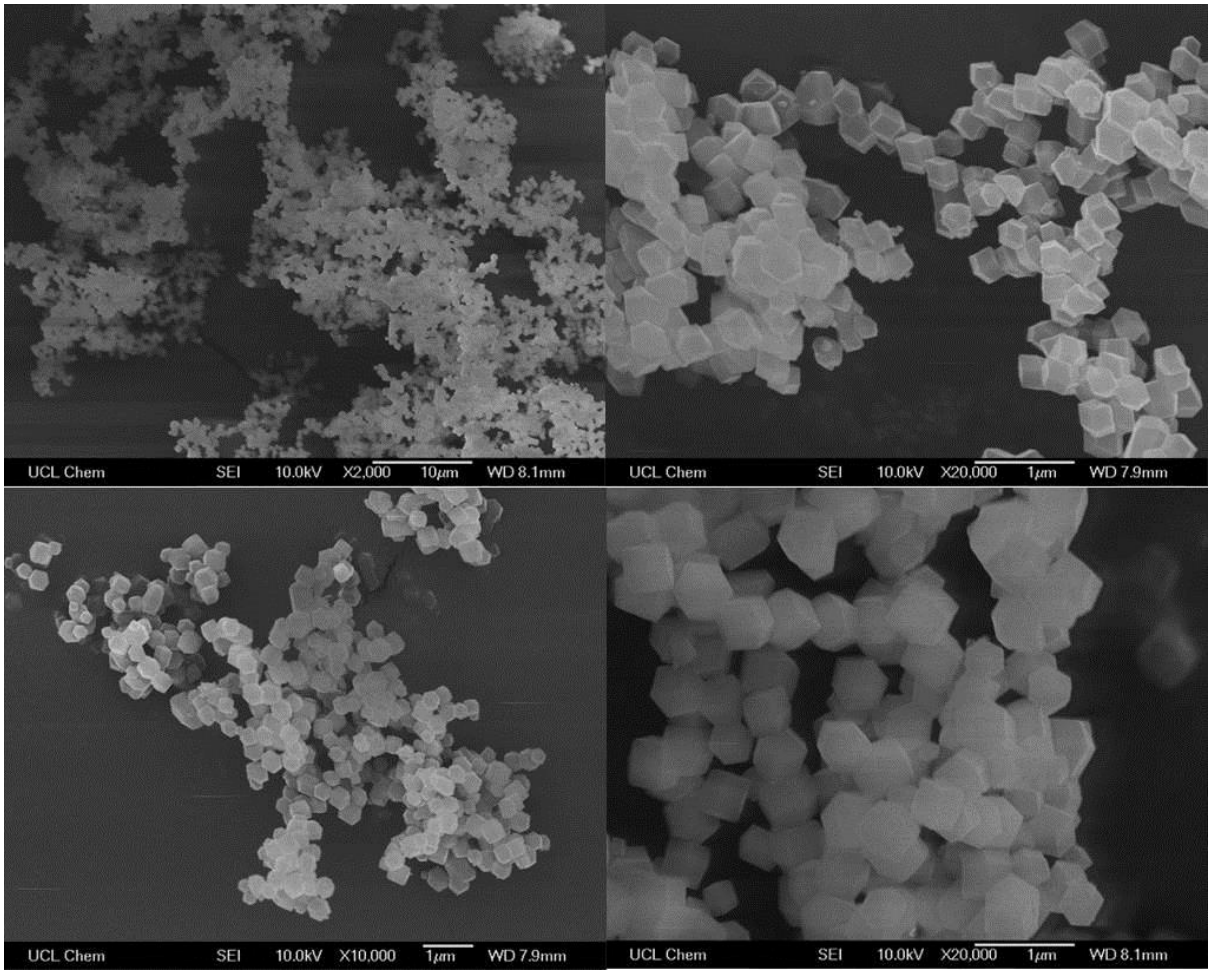

Figure S12. SEM images of ZIF-8, showing well-structured crystallites.

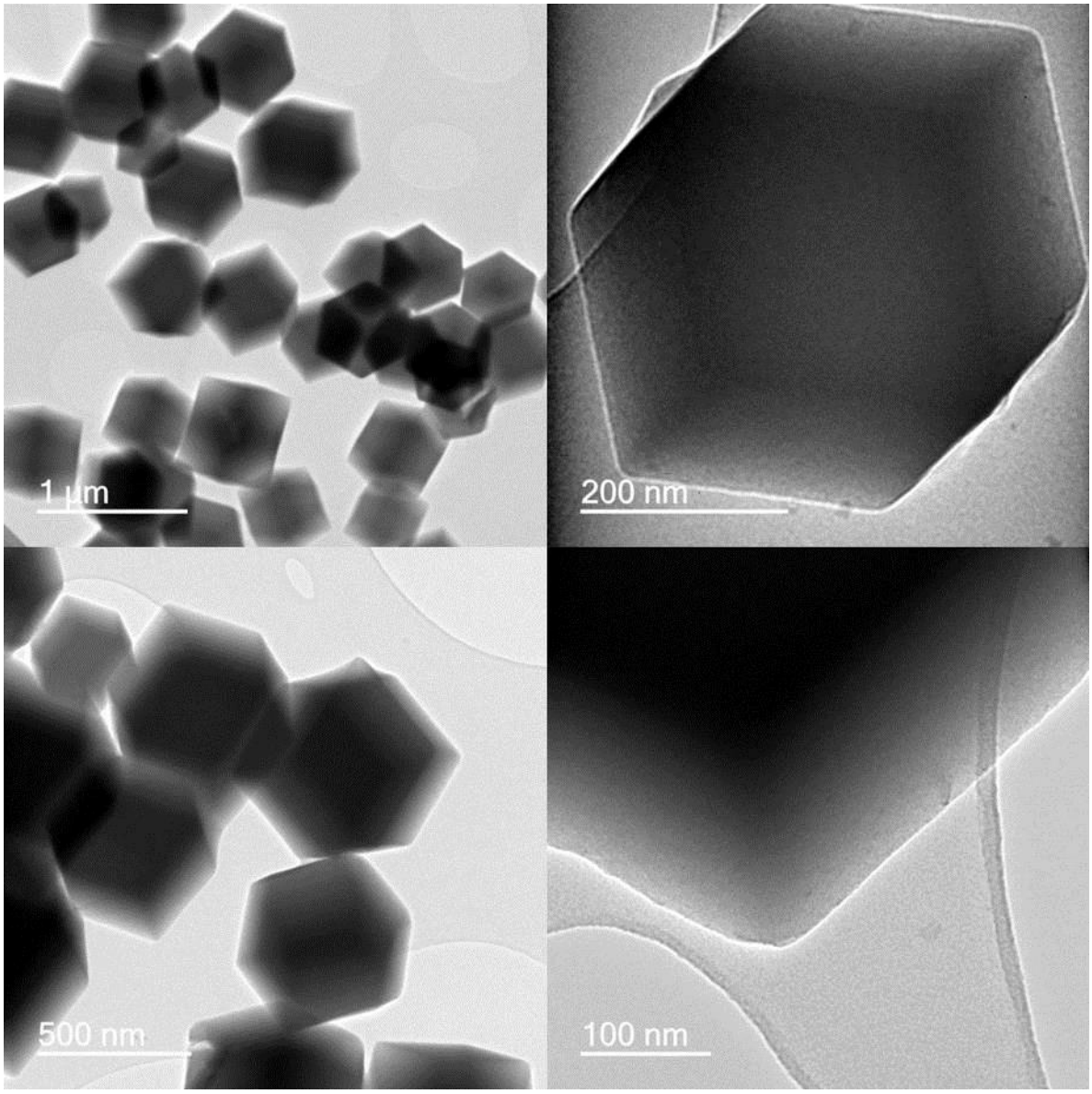

Figure S13. TEM images at different magnification of $Co_{25}Zn_{75}$-ZIF-8, showing well-structured crystallites similar to the ZIF-8 as observed at SEM.

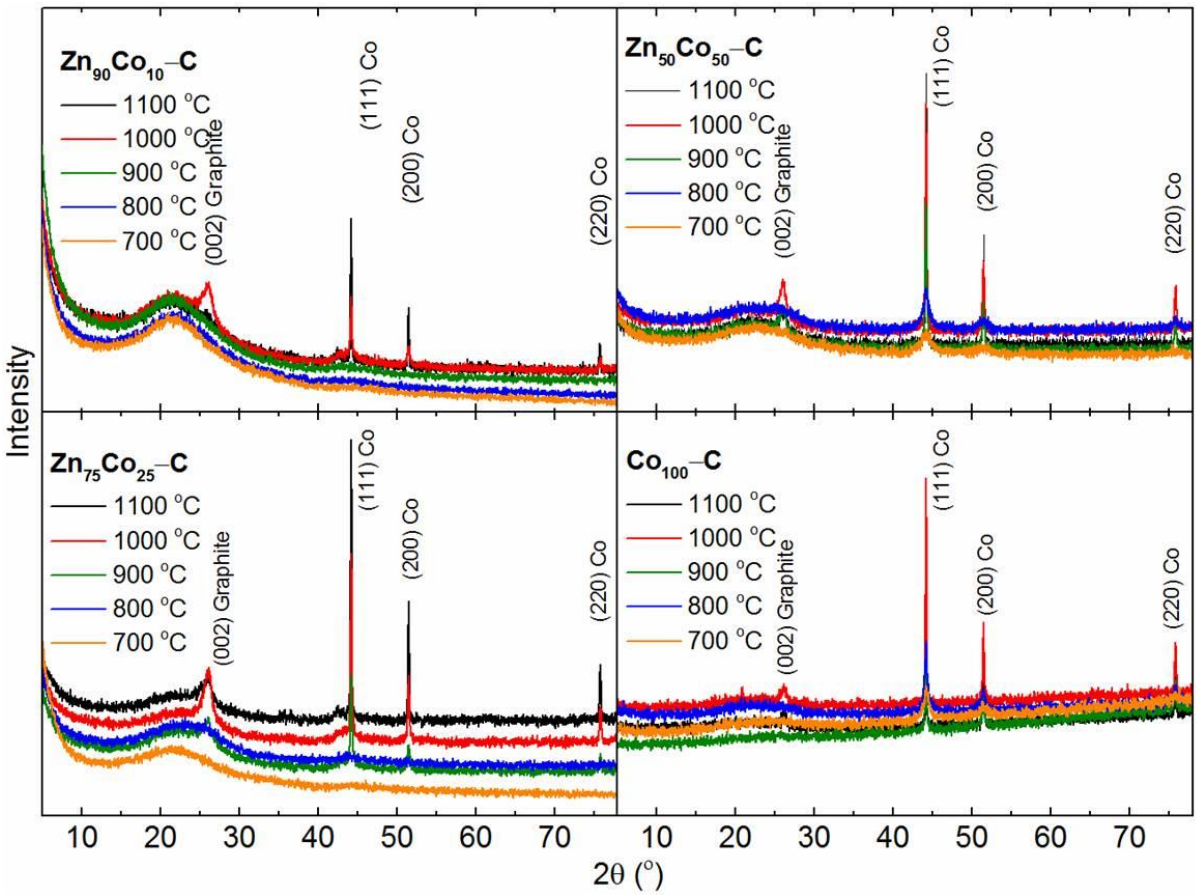

Figure S14. PXRD patterns of NPCs of $Co_{10}Zn_{90}$-C (top left), $Co_{25}Zn_{75}$-C (bottom left), $Co_{50}Zn_{50}$-C (top right) and Co_{100}-C (bottom right) at a carbonization temperature of (700, 800, 900, 1000, 1100) °C for 10h in each case. See that all the sharp and intense diffraction peaks are assigned to a pure phase fcc Co(0) [see JCPDS 15-0806 for fcc cobalt and JCPDS 05-0727 for hcp cobalt]. The crystallization of carbon (see a growing graphitic (002) peak at 2θ of ~26°) is seen with increasing carbonization temperature /or cobalt substitution for zinc in ZIF-8 at or above 800 °C. Also note that the crystallization or clustering of cobalt is seen with increasing carbonization temperature as observed with increased intensity of diffraction peaks. Also see that at low cobalt concentrations, e.g., x = 10 & 25, the crystalline/clustered cobalt peaks appear only at higher carbonization temperatures of ≥900 °C.

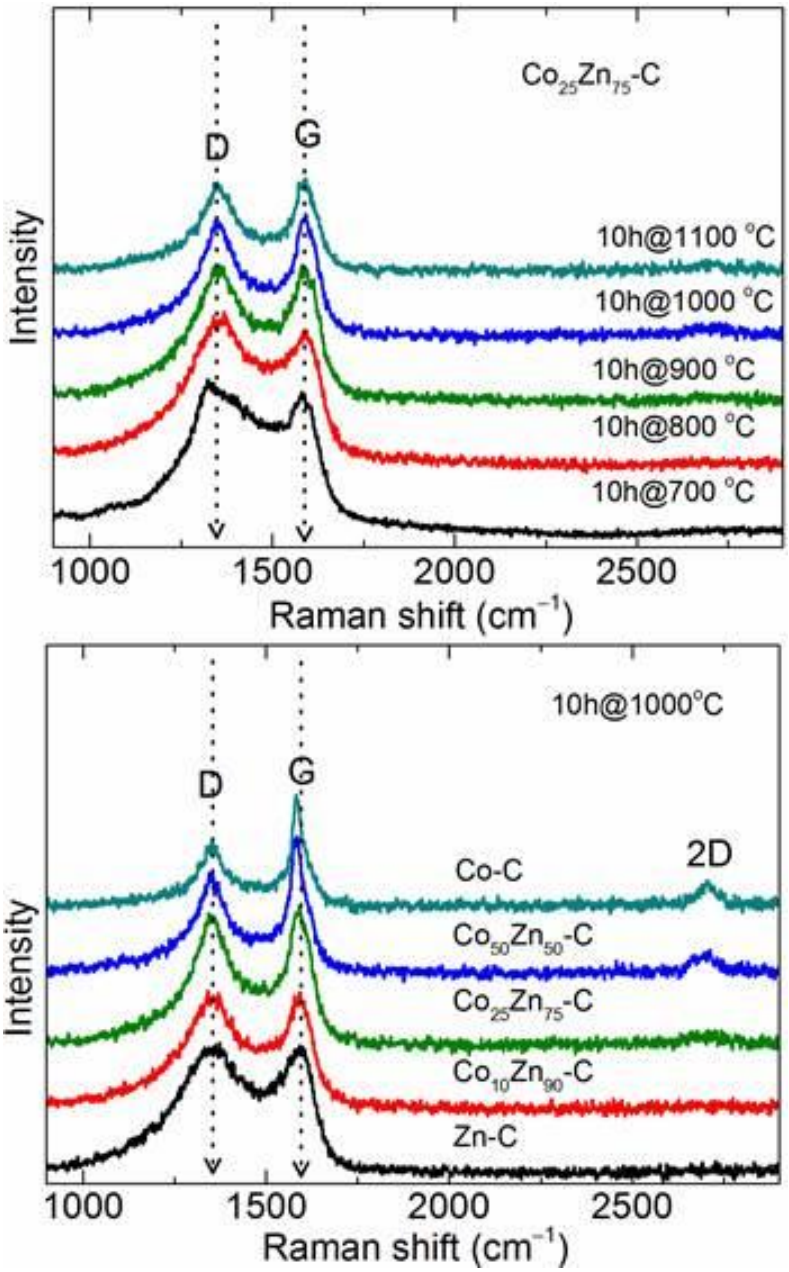

Figure S15. Raman spectra of $Co_{25}Zn_{75}$–C at different temperatures (top) and Co_xZn_{100-x}–C1000 (bottom). Graphitization can be seen by sharp Raman D and G bands at Raman shift of ≈1354 cm^{-1} and ≈1583 cm^{-1}, respectively when going from Zn_{100}–C to Co_{100}–C. The appearance of a second order 2D band at ≈2700 cm^{-1} is a signature for ordered layered structure [ref. Sa6,Sa7].

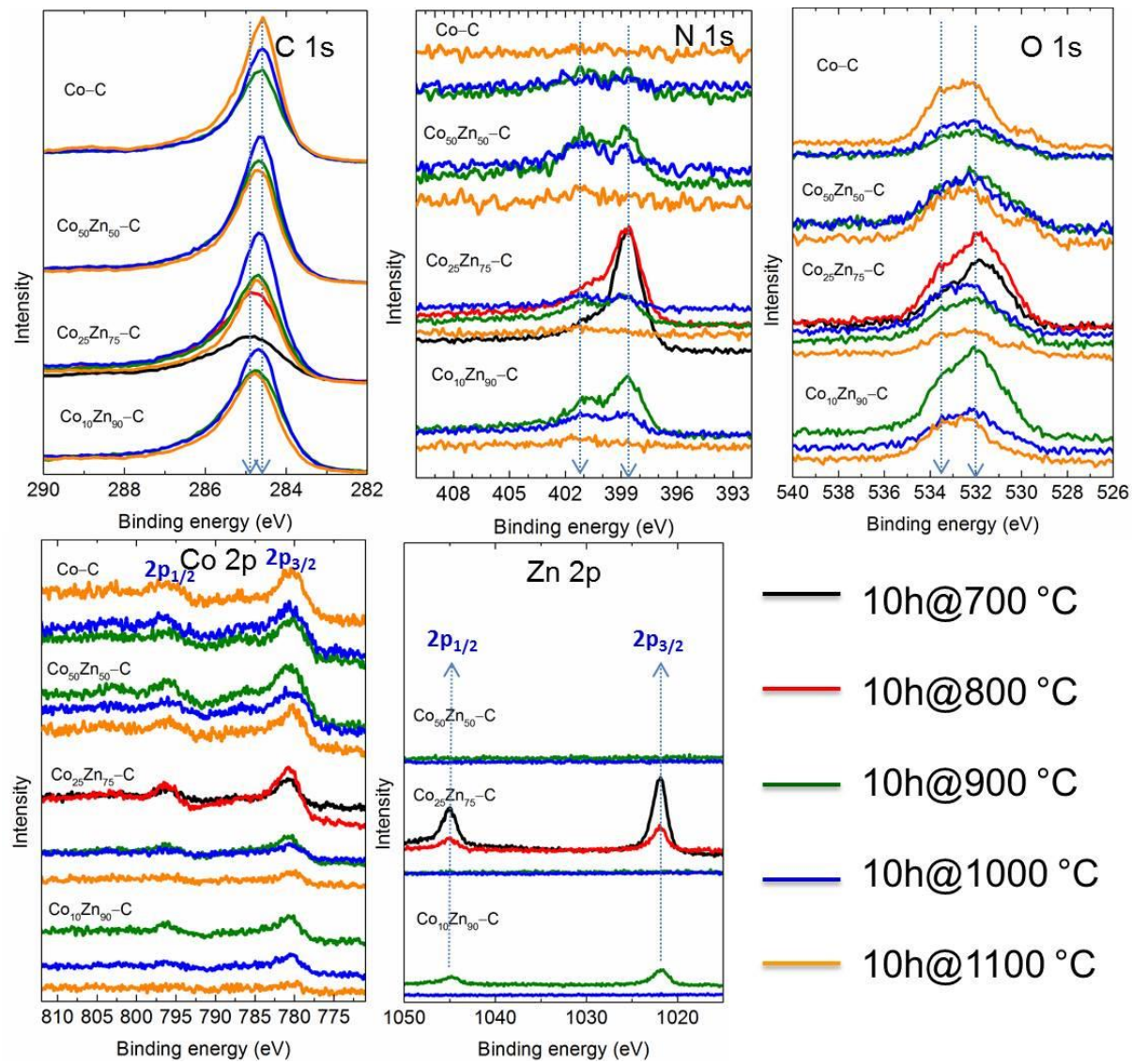

Figure S16. In clock wise, C 1s, N 1s, O 1s, Zn 2p and Co 2p XPS core level spectra of Co_xZn_{100-x}-NPCs derived at (700, 800, 900, 1000, 1100) °C for 10 h. Set of samples from same ZIF-8 composition are grouped together. The C 1s peak shift from a binding energy (BE) of ~284.9 eV to a BE of 284.6 eV with increasing cobalt substitution and carbonization temperature is an indication of transformation of more nitrogen containing NPCs (e.g., at 700 °C) to a pure phase graphitic sp^2 carbon (e.g., at 1100 °C). This loss of nitrogen functionality is clearly visible in N 1s spectra, where a dominant pyridinic type nitrogen in imidazolate ligand peak at BE of 398.6 eV and 700 °C is completely lost at 1100 °C due to temperature induce simultaneous decomposition and conversion to graphitic nitrogen, a new and weak peak at higher BE of 401 eV. O 1s spectra show broad, two to three peak behaviour suggest C−O (at BE of >533 eV, a second most contributor) and Co−O (BE of ~530 eV, very weak & least contributor) bonding in addition to major atmospheric adsorbed oxygen at BE of ~532 eV. Zn 2p spectra show the samples are zinc free at temperatures at (for x = 25 or higher) or above (for x = 10) 900 °C. The Co 2p with two satellite peaks positioned close to the main $2p_{3/2}$ and $2p_{1/2}$ peaks suggest a surface oxidized cobalt and is assigned to Co(II)O.

Table S3. XPS based elemental concentrations in Co_xZn_{100-x}-ZIF-8 derived carbons, carbonized at different temperatures with same 10 h annealing time.

Sample	C (at%)	N (at%)	O (at%)	Co (at%)*	Zn (at%)
$Co_{25}Zn_{75}$-C700	70.0	18.0	9.0	0.4	2.6
$Co_{25}Zn_{75}$-C800	79.0	10.0	9.0	1.0	1.0
$Co_{25}Zn_{75}$-C900	90.0	4.5	5.0	0.4	-
$Co_{25}Zn_{75}$-C1000	93.0	2.3	4.5	0.2	-
$Co_{25}Zn_{75}$-C1100	96.0	0.5	4.0	-	-
$Co_{50}Zn_{50}$-C900	93.0	2.8	3.3	0.7	-
$Co_{50}Zn_{50}$-C1000	95.0	1.3	3.3	0.2	-
$Co_{50}Zn_{50}$-C1100	96.0	0.5	3.5	0.3	-
$Co_{10}Zn_{90}$-C900	86.0	5.5	8.0	0.2	0.3
$Co_{10}Zn_{90}$-C1000	92.0	3.8	4.0	0.2	-
$Co_{10}Zn_{90}$-C1100	94.0	0.5	5.5	-	-
Co_{100}-C1000	95.5	0.2	4.0	0.3	-
Zn_{100}-C1000	86.0	5.5	9.0	-	0.5

* Due to the formation of cobalt -core and carbon-shell the XPS cannot report true cobalt content in the sample, mainly because of the carbon shielding effect. But the actual cobalt -content in the carbonized samples is reported with thermogravimetric analysis at **Figure S28**.

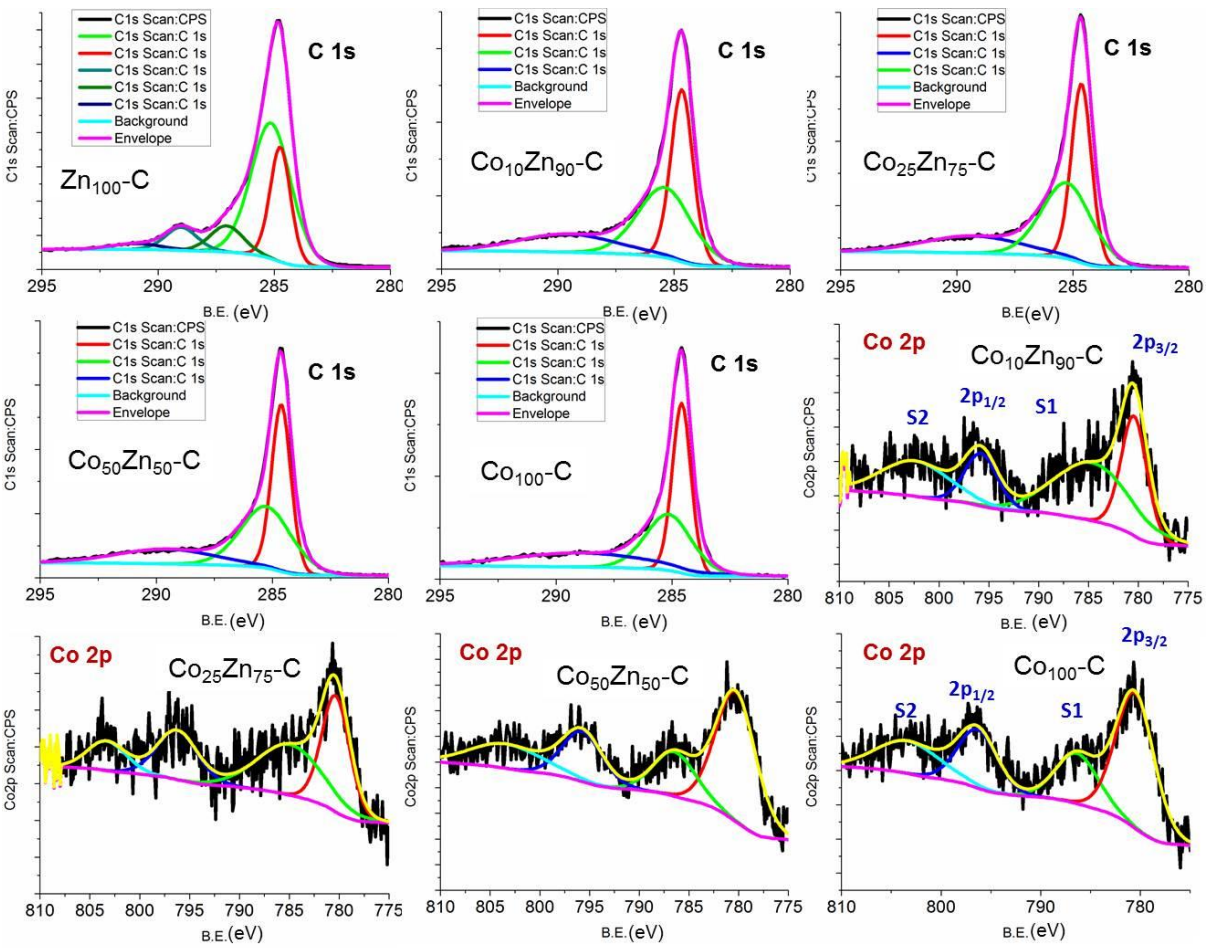

Figure S17. The deconvolution of C 1s and Co 2p spectra and peak fittings of Co_xZn_{100-x}-C1000. This shows relative changes of individual contributions, to say the gradual decrease of dominating C−O and C−N contributions with peaks at or above BE of 285 eV in C 1s spectra of Zn_{100}-C1000 is seen with increasing substitutional cobalt. At highest cobalt, the C 1s spectra consist mostly of graphitic sp^2 carbon. The Co 2p spectra with two main peak positions at BE of ~780.3 eV and ~796 eV with adjacent satellite peaks at (between 784 & 786) eV and ~803.3 eV, suggest surface oxidized cobalt in its 2^+ oxidation state, i.e., CoO [Ref. Sa8,Sa9,Sa10].

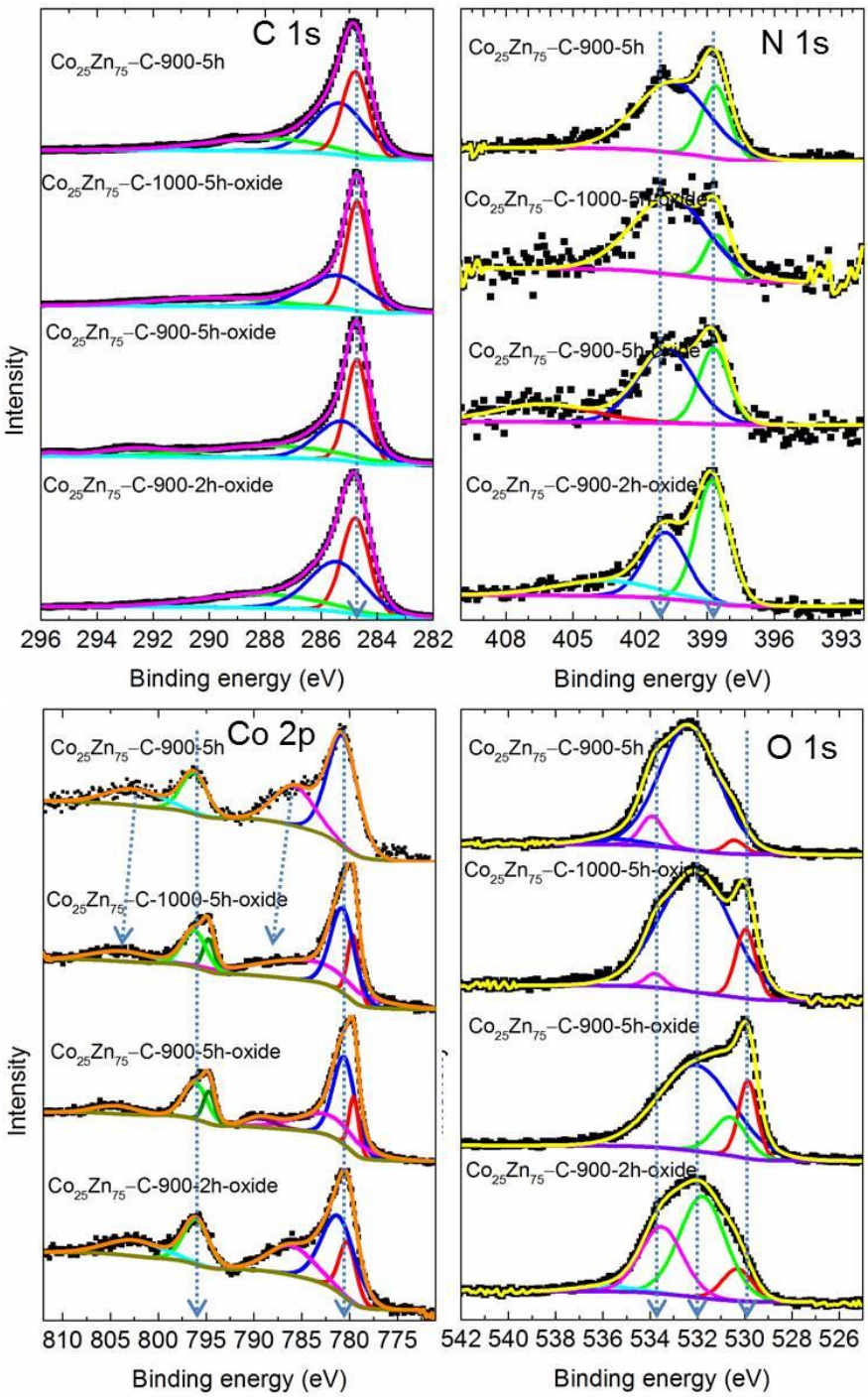

Figure S18. Peak fittings of C 1s, N 1s, O 1s and Co 2p spectra (in clock wise direction) of $Co_{25}Zn_{75}$-C900 and $Co_{25}Zn_{75}$-C1000 samples. The control oxidation of samples is represented with –oxide (which is nothing but Co_3O_4/C). The C 1s peak fittings suggest oxygen and nitrogen containing carbon (see new shoulders at BE of >285 eV). The two and three peak behaviour of N 1s spectra show majority of pyridinic nitrogen-type (peak at BE of 398.9 eV) in addition to graphitic nitrogen-(second major peak at BE of 401 eV) and oxidized nitrogen-(a weak peak at BE of >405 eV) type. O 1s show peaks at ~530 eV, 532.3 eV and 533.7 eV corresponding to Co^{2+}–O, adsorbed oxygen and sp^3 C–O, respectively. The Co 2p spectra for controlled oxidized samples are in good agreement with the Co_3O_4 [Ref. Sa8,Sa9,Sa10].

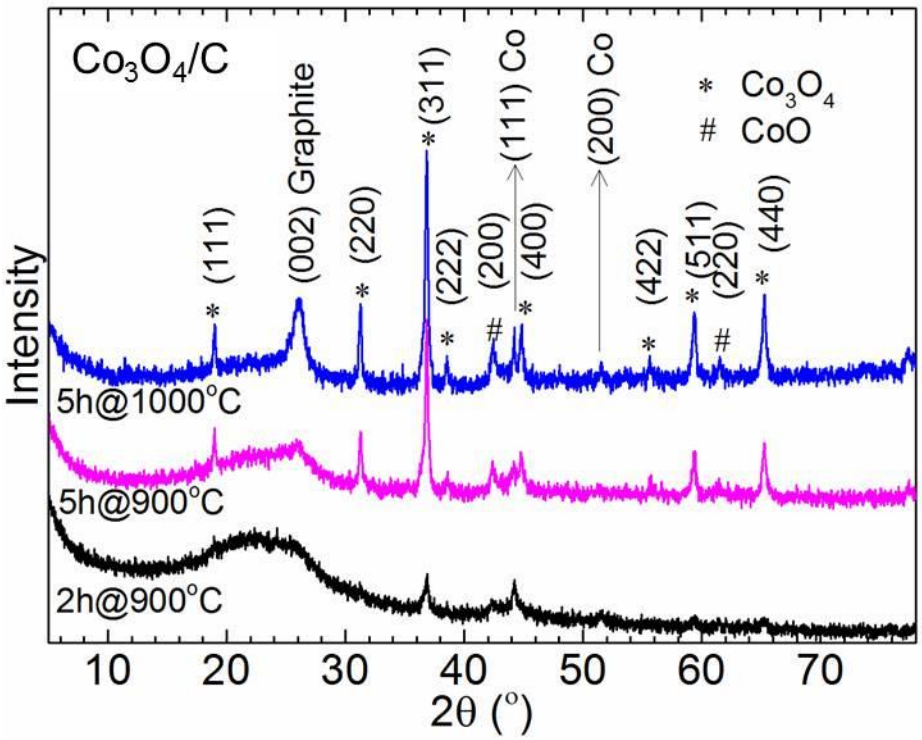

Figure S19. The PXRD patterns of controlled oxidized $Co_{25}Zn_{75}$-C900 and $Co_{25}Zn_{75}$-C1000 samples show predominantly a cubic spinel Co_3O_4 (*) phase (space group Fd3m) (JCPDS card no. 43-1003), with a little evidence for fcc cobalt and CoO (#) [Ref. Sa11].

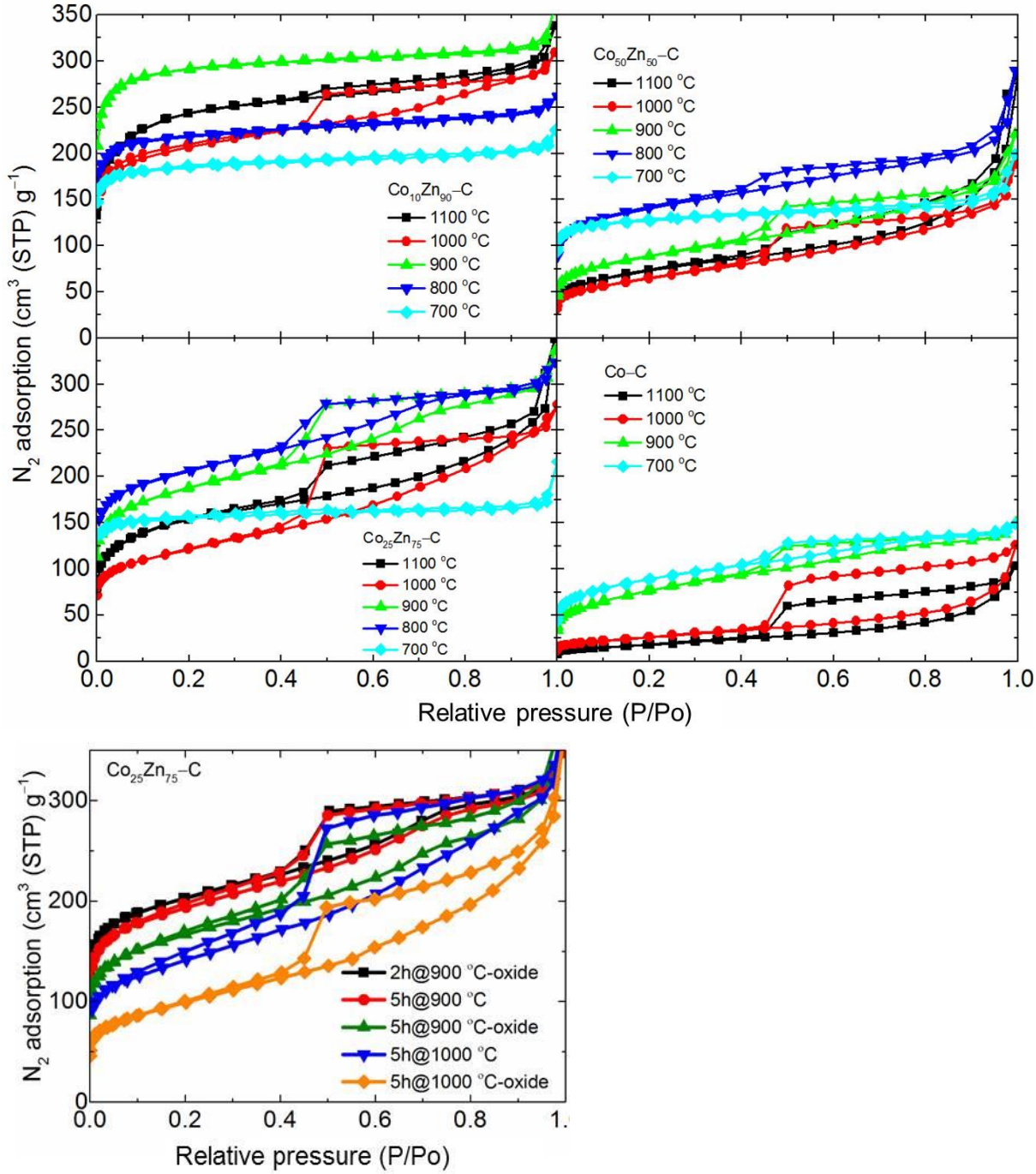

Figure S20. 77 K N_2 sorption isotherms of all the Co_xZn_{100-x}-NPCs obtained at carbonization temperature of (700, 800, 900, 1000, 1100) °C for 10 h (top four). See that a considerably reduced N_2 uptake with increasing substitutional cobalt for zinc. This is also true with the carbonization temperature at or above 800 °C, suggesting a cobalt-induced graphitization. This is also observed with opening the hysteresis gap between adsorption and desorption isotherms. Bottom: comparative isotherms of $Co_{25}Zn_{75}$-C900 NPCs after control carbonization and oxidation. The control oxidation of samples is represented with –oxide (which is nothing but Co_3O_4/C). See that after oxidation the samples show a reduced uptake due to the loss of sample in the form of gasification, $C + O_2 \rightarrow CO_2$ during control oxidation.

Table S4. The porosity and gas uptake in all precursor ZIFs and its NPCs. The control oxidation of samples is represented with –oxide (which is nothing but Co_3O_4/C).

S. No.	Sample description	BET Specific surface area (m^2 g^{-1})	Total pore volume (cm^3 g^{-1})	H_2 uptake at 77 K and 1 bar (cm^3(STP) g^{-1})	CO_2 uptake at 298 K and 1 bar (cm^3(STP) g^{-1})
1	ZIF−8	1795.0	0.746	151.0	20.0
2	$Co_{10}Zn_{90}$−ZIF−8	1723.0	0.741	157.0	21.0
3	$Co_{25}Zn_{75}$−ZIF−8	1722.0	0.740	154.0	21.0
4	$Co_{50}Zn_{50}$−ZIF−8	1750.0	0.756	170.0	22.0
5	Co−ZIF−8	1800.0	0.748	170.0	21.0
6	$Co_{10}Zn_{90}$−C700-10h	740.0	0.348	152.0	67.0
7	$Co_{10}Zn_{90}$−C800-10h	860.0	0.405	170.0	70.0
8	$Co_{10}Zn_{90}$−C900-10h	1140.0	0.557	218.0	77.0
9	$Co_{10}Zn_{90}$−C1000-10h	774.0	0.478	160.0	45.0
10	$Co_{10}Zn_{90}$−C1100-10h	910.0	0.521	203.0	55.0
11	$Co_{25}Zn_{75}$−C700-10h	627.0	0.334	139.0	65.0
12	$Co_{25}Zn_{75}$−C800-10h	764.0	0.502	149.0	53.0
13	$Co_{25}Zn_{75}$−C900-10h	685.0	0.520	121.0	36.0
14	$Co_{25}Zn_{75}$−C1000-10h	437.0	0.430	74.0	20.0
15	$Co_{25}Zn_{75}$−C1100-10h	562.0	0.541	86.0	22.0
16	$Co_{50}Zn_{50}$−C700-10h	495.0	0.308	109.0	47.0
17	$Co_{50}Zn_{50}$−C800-10h	678.0	0.449	100.0	33.0
18	$Co_{50}Zn_{50}$−C900-10h	310.0	0.342	49.0	15.0
19	$Co_{50}Zn_{50}$−C1000-10h	226.0	0.292	32.0	8.0
20	$Co_{50}Zn_{50}$−C1100-10h	266.0	0.441	41.0	11.0
21	Co_{100}−C700-10h	320.0	0.230	58.0	15.0
22	Co_{100}−C900-10h	275.0	0.232	37.0	9.0
23	Co_{100}−C1000-10h	96.0	0.195	14.0	3.0
24	Co_{100}−C1100-10h	70.0	0.160	16.0	3.0
25	$Co_{25}Zn_{75}$−C900-2h-oxide	747.0	0.551	135.0	52.0
26	$Co_{25}Zn_{75}$−C900-5h	717.0	0.537	-	-
27	$Co_{25}Zn_{75}$−C900-5h-oxide	607.0	0.588	145.0	39.0
28	$Co_{25}Zn_{75}$−C1000-5h	500.0	0.598	-	-
29	$Co_{25}Zn_{75}$−C1000-5h-oxide	360.0	0.551	69.0	23.0

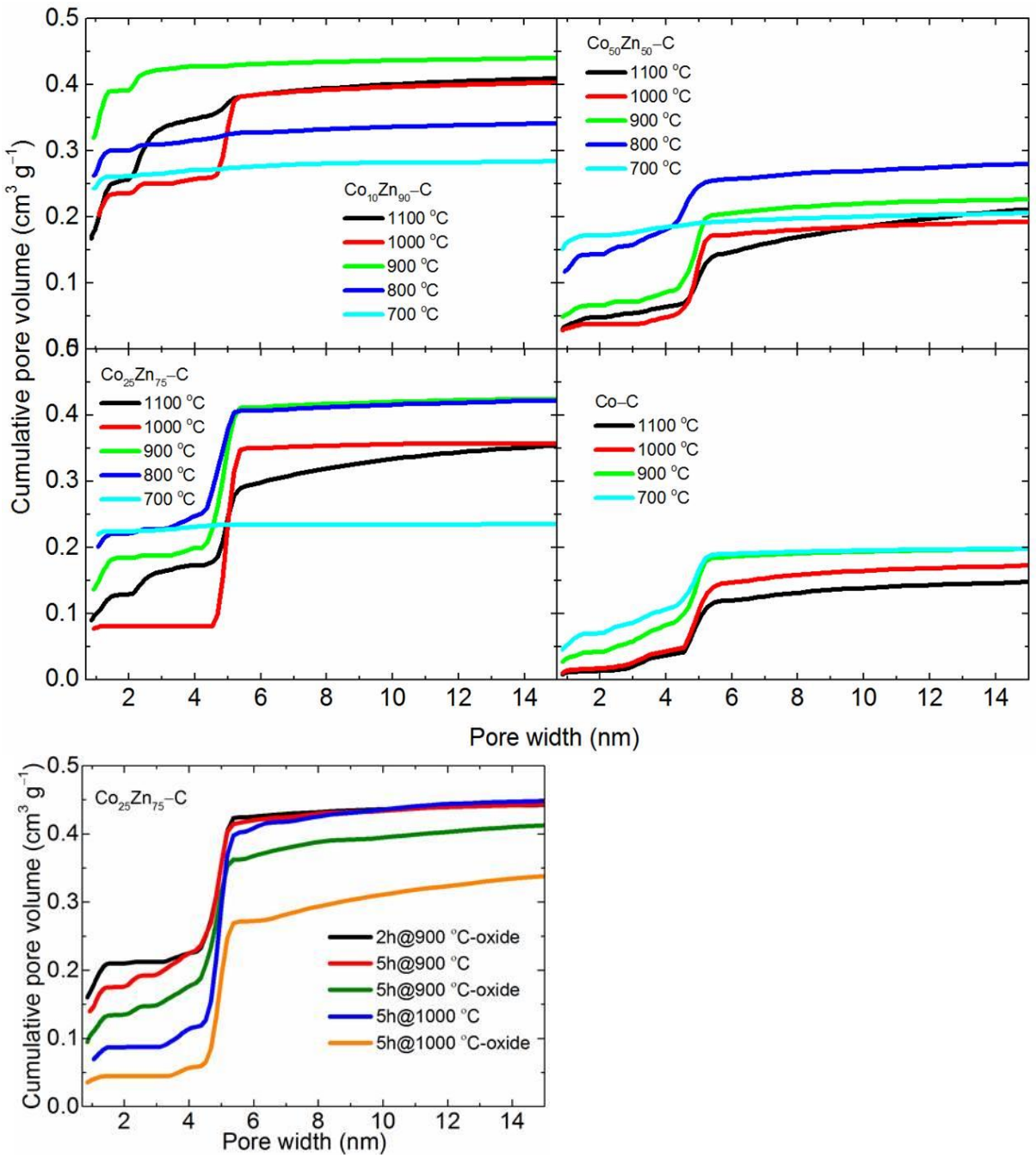

Figure S21. 77 K N_2 sorption isotherms QSDFT derived cumulative pore volume plots against pore width of all the Co_xZn_{100-x}-NPCs obtained at carbonization temperature of (700, 800, 900, 1000, 1100) °C for 10 h (top four) and after control carbonization and oxidation of $Co_{25}Zn_{75}$-C900 NPCs (bottom). The control oxidation of samples is represented with –oxide (which is nothing but Co_3O_4/C). See that a considerably reduced pore volume with increasing substitutional cobalt for zinc. This is also true with the carbonization temperature at or above 800 °C suggesting a cobalt-induced graphitization. The step-like change suggesting a single pore-type of ~5 nm.

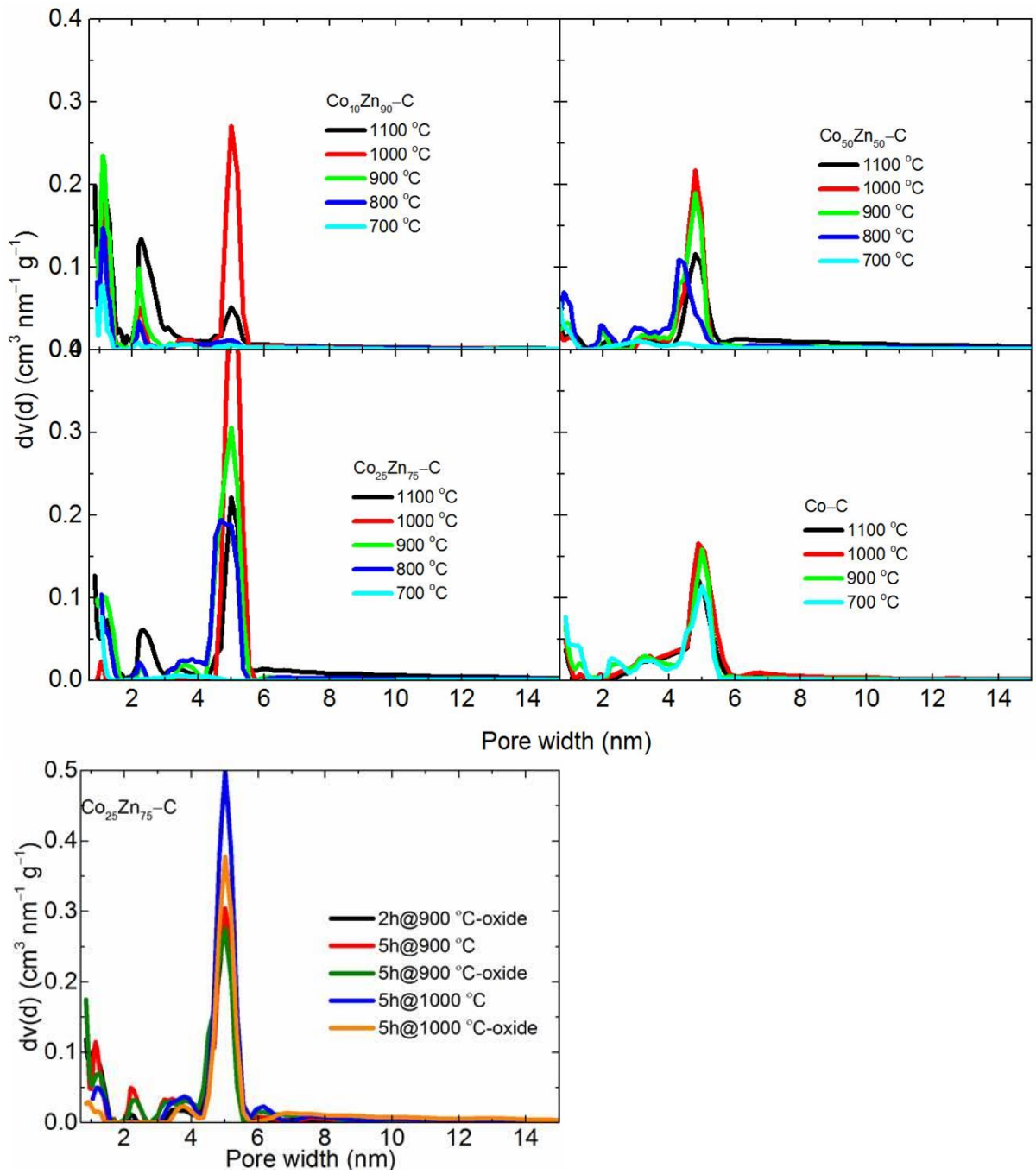

Figure S22. 77 K N_2 sorption isotherms QSDFT derived pore size distribution plots of all the Co_xZn_{100-x}-NPCs obtained at carbonization temperature of (700, 800, 900, 1000, 1100) °C for 10 h (top four) and after control carbonization and oxidation of $Co_{25}Zn_{75}$-C900 NPCs (bottom). The control oxidation of samples is represented with –oxide (which is nothing but Co_3O_4/C). See that shift of the pore size from microporous region to mesoporous region with increasing substitutional cobalt for zinc. Most of the cases a single type pore at ~5 nm in width is observed.

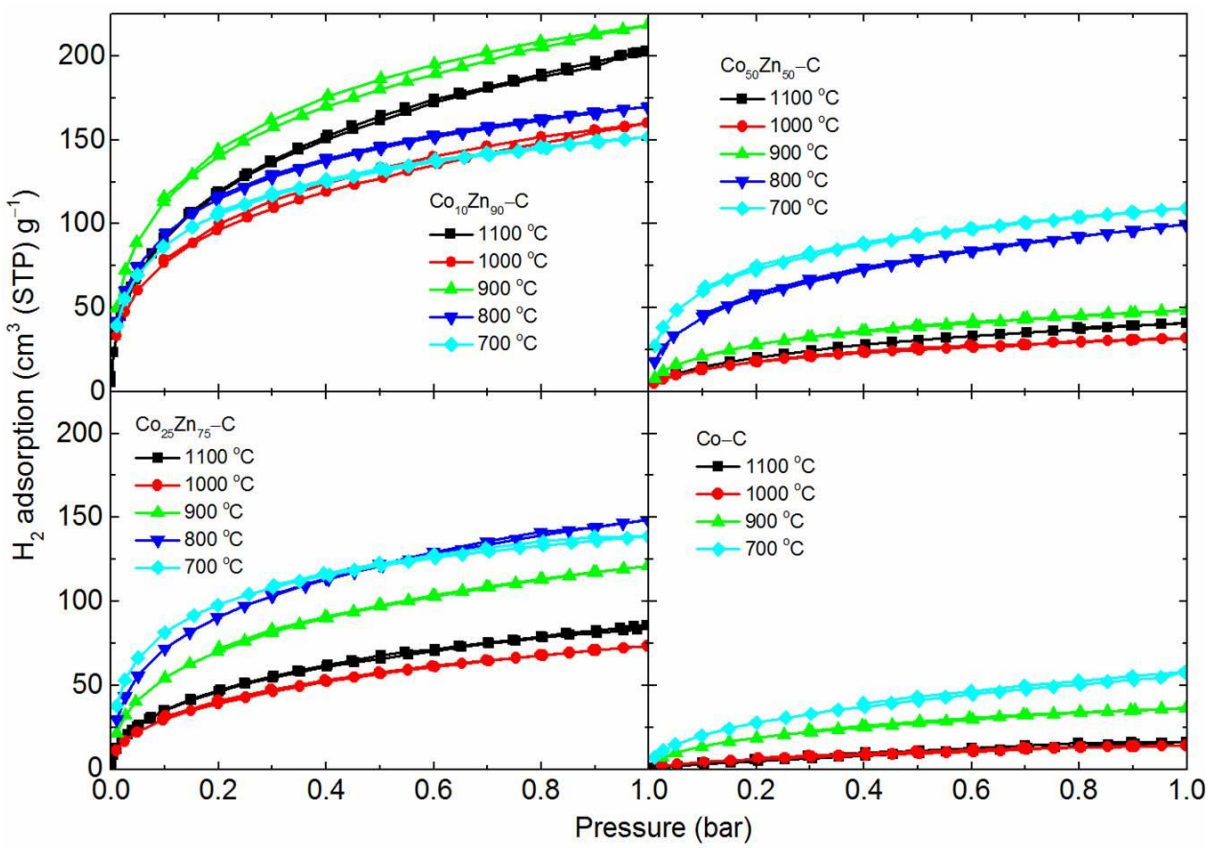

Figure S23. 77 K H_2 uptake isotherms of all the Co_xZn_{100-x}-NPCs obtained at carbonization temperature of (700, 800, 900, 1000, 1100) °C for 10 h. See that a considerably reduced uptake with increasing substitutional cobalt for zinc. A clear influence of microporosity and nitrogen-functionality (high uptake), and a graphitization (low uptake) is seen.

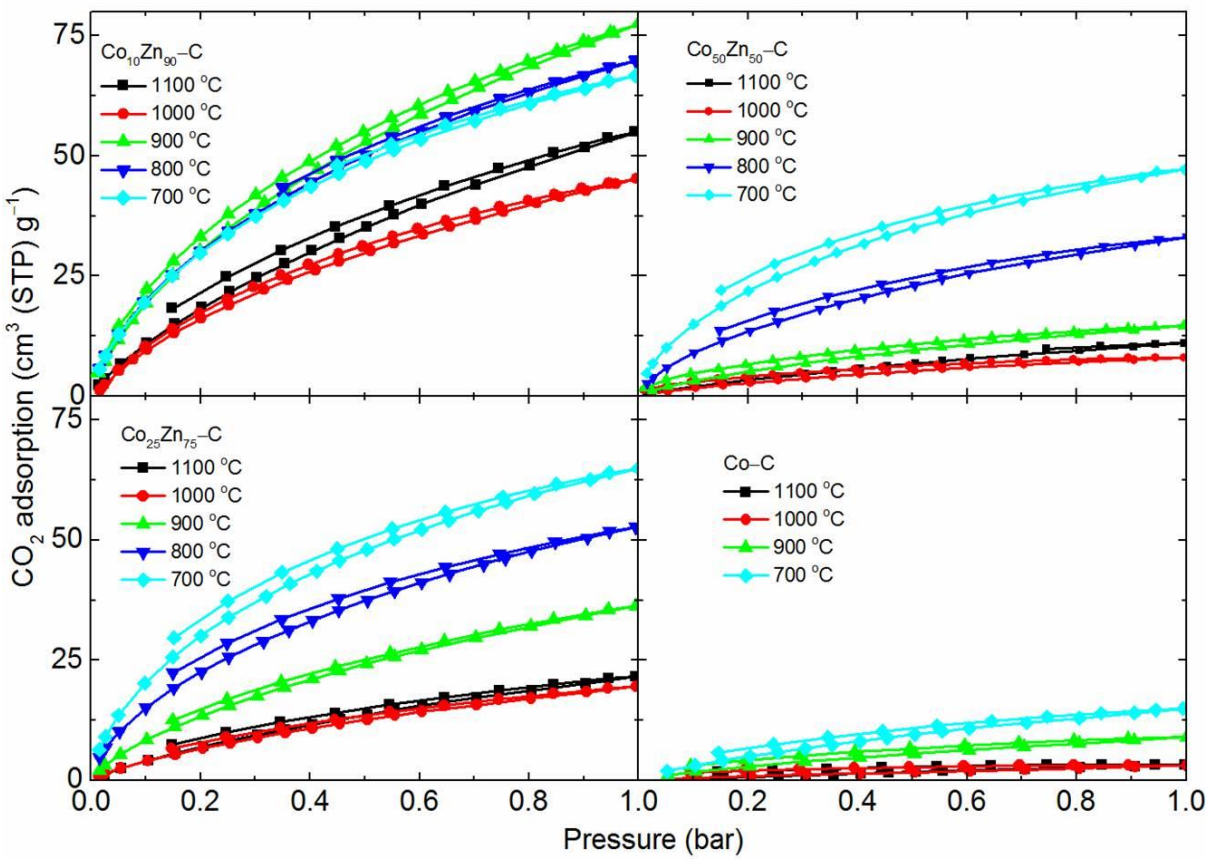

Figure S24. 298 K CO_2 uptake isotherms of all the Co_xZn_{100-x}-NPCs obtained at carbonization temperature of (700, 800, 900, 1000, 1100) °C for 10 h. See that a considerably reduced uptake with increasing substitutional cobalt for zinc.

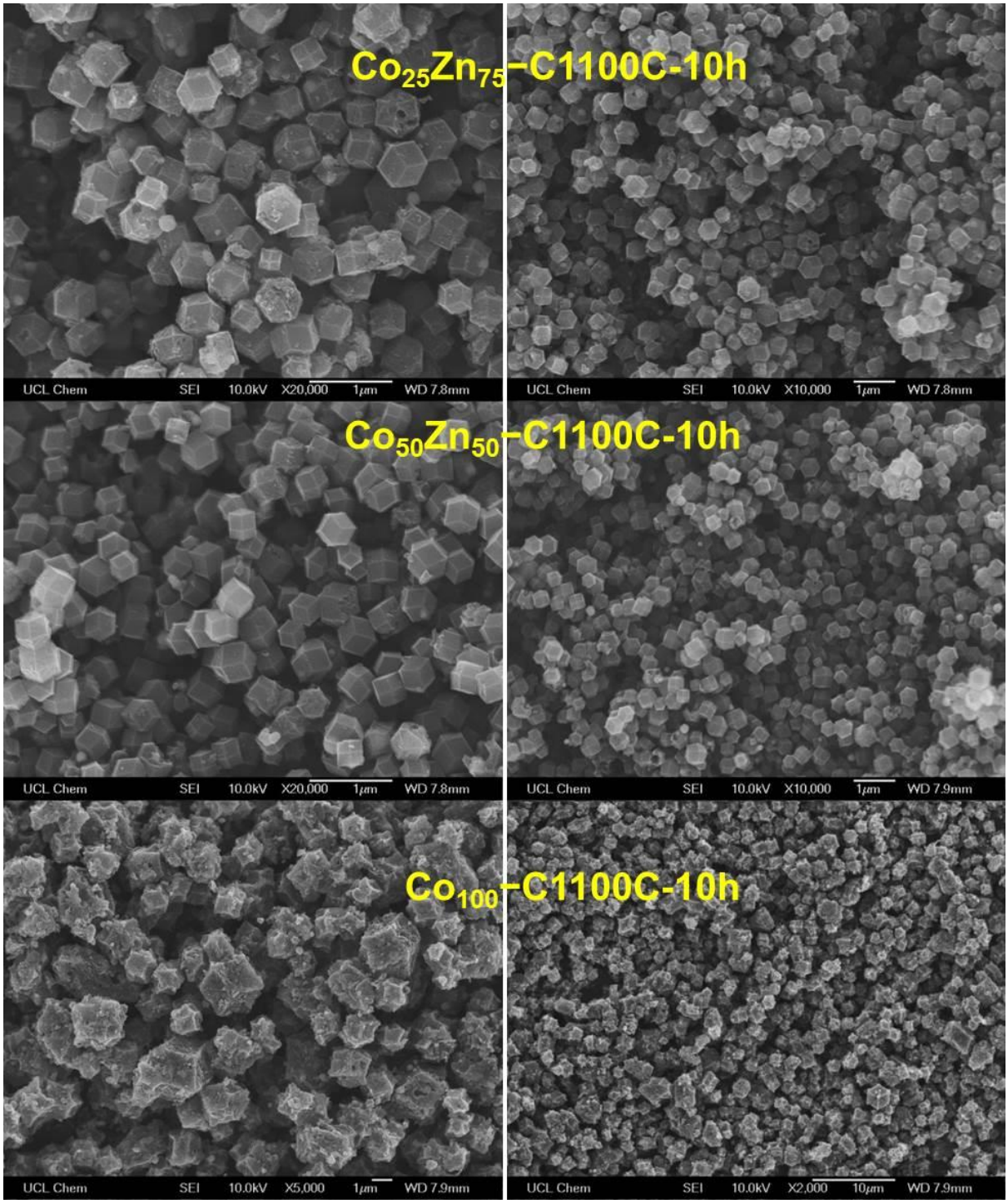

Figure S25. SEM images of NPCs obtained at 1100 °C; $Co_{25}Zn_{75}$-C1100 (top), $Co_{50}Zn_{50}$-C1100 (middle), Co_{100}-C1100 (bottom). The crystallites preserve the morphology of precursor ZIFs. The transition to a highly graphitized nature can be seen at change in morphology of Co_{100}-C1100.

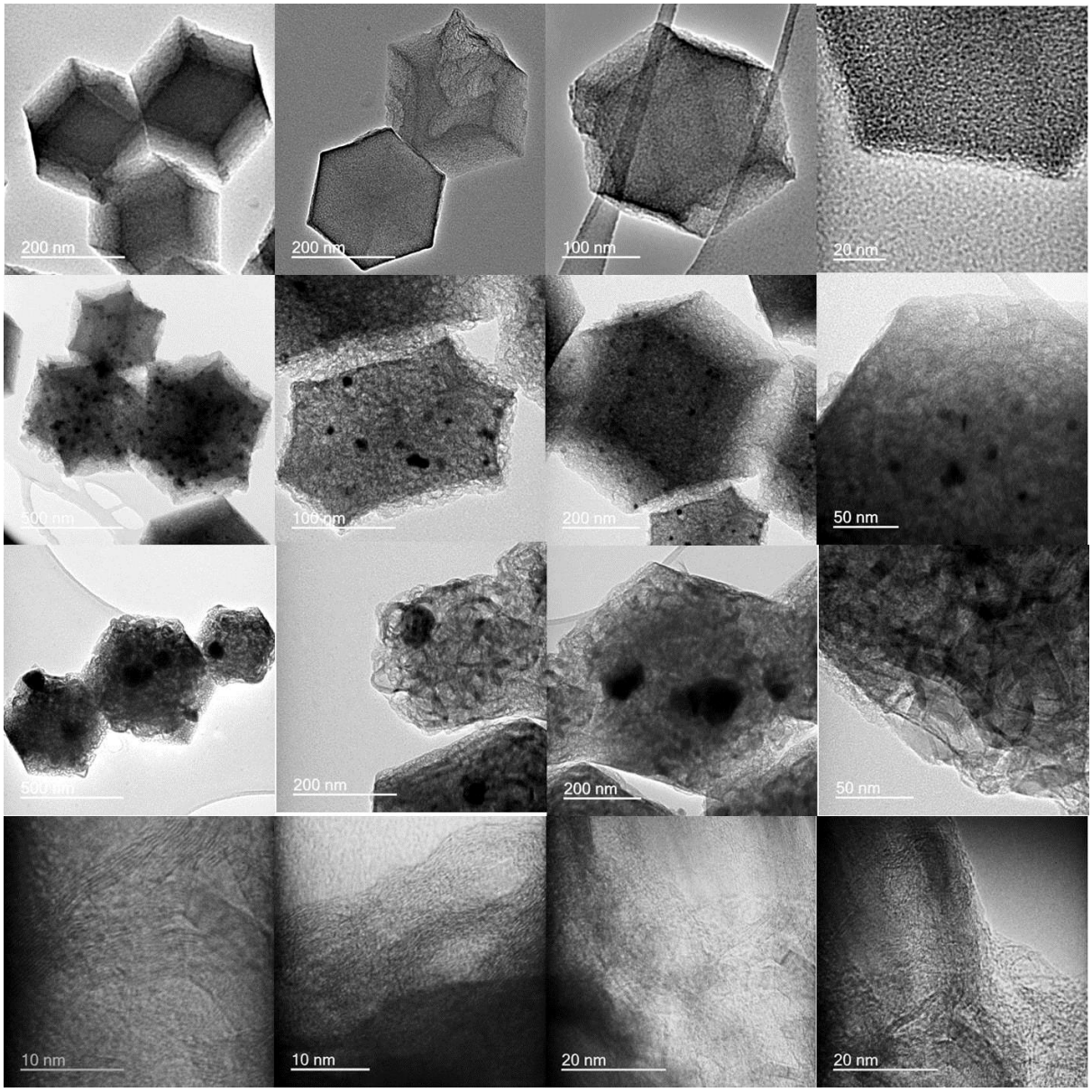

Figure S26. TEM images of NPCs of Zn_{100}-C1000-10h (top row), $Co_{25}Zn_{75}$-C800-10h (second row from top) and $Co_{25}Zn_{75}$-C1000-10h (second bottom row). A clear change in morphology of carbon is seen from amorphous type in Zn_{100}-C1000-10h (metal free) to ordered graphitic type in $Co_{25}Zn_{75}$-C1000-10h (bottom row). Also see **Figures S4 & S5** for TEM images of Zn_{100}- C1000 & Co_{100}-C1000. The finely distributed Co/Zn-metal centres in $Co_{25}Zn_{75}$-C800-10h become agglomerated at $Co_{25}Zn_{75}$-C1000-10h.

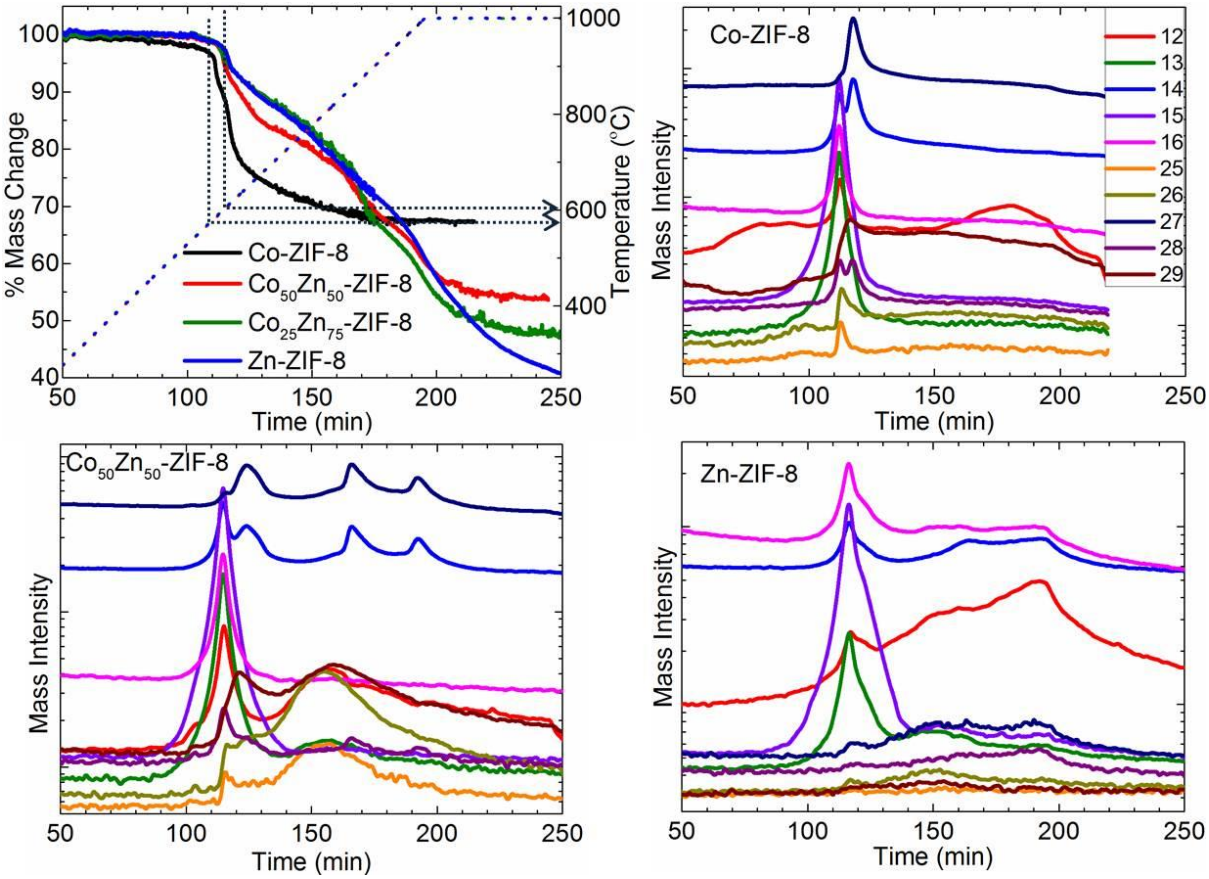

Figure S27. A combined TG (top-left) – MS (right & bottom-left) analysis shows the mechanism of structure transition during thermolysis of Co_xZn_{100-x}-ZIF-8. A framework decomposition/carbonization temperature is seen at ≈600 °C (less than 600 °C in case Co-ZIF-8), and evolution of various decomposed gaseous mixtures; C, C_xH_y, C_xN_y or both, $H_zC_xN_y$, identified by atomic mass unit (amu); 12-C, 13-CH, 14-CH_2, 15-CH_3, 16-CH_4, 25-HC_2, 26-C_2H_2 or CN, 27-HCN, 28-H_2CN or N_2, 29-H_2CNH. Note that majority of N-free hydrocarbon signals in MS around 600 °C are mainly due to evaporation of free rotational methyl group on the imidazolate and the actual decomposition of imidazolate ring is seen at above 600 °C with the release of combination of CNH radicals [Ref. Sa12]. The increase in TG residual mass at 1000 °C is in good agreement with the increased Co substitutional concentration for volatile zinc. Also note that the increased cobalt concentration leads to a rapid ligand degradation/mass loss at reduced temperatures than ZIF-8.

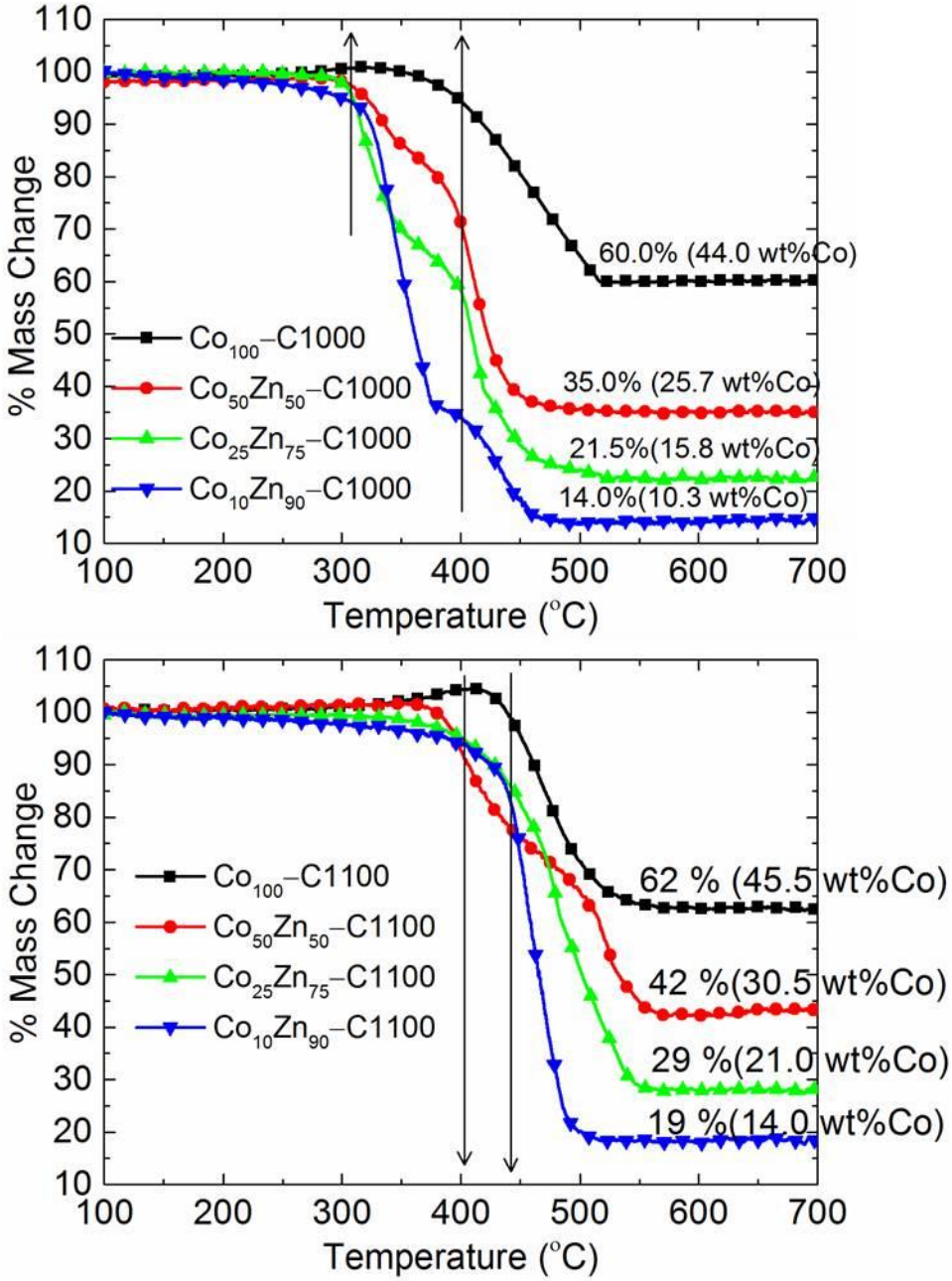

Figure S28. TG plots of Co_{100}–, $Co_{50}Zn_{50}$–, $Co_{25}Zn_{75}$– and $Co_{10}Zn_{90}$–NPCs, synthesised at 1000 °C for 10 h (top) and 1100 °C for 10 h (bottom). The measurements were carried out with a heating rate of 3 °C per minute and under flowing air to burnout the carbon to get true cobalt concentration that is embedded in the carbon matrix. The residual weights at or above 600 °C corresponding to the Co_3O_4 (assuming complete transformation of the cobalt metal in to oxide). Thus the cobalt-metal content is calculated accordingly.

The carbonization temperature, 1000 °C (top) and 1100 °C (bottom) as well as cobalt-induced graphitization is clearly understood with two-stage TG mass loss (for 1000 °C samples) or enhanced thermal stability (for 1100 °C samples). The mass loss indicates the gasification of carbon; $C + O_2 \rightarrow CO_2$. In case of 1000 °C samples, at first stage, the sample start burning at ~300 °C is amorphous carbon. The graphitized carbon is relatively stable and starts burning at 100 °C higher temperature.

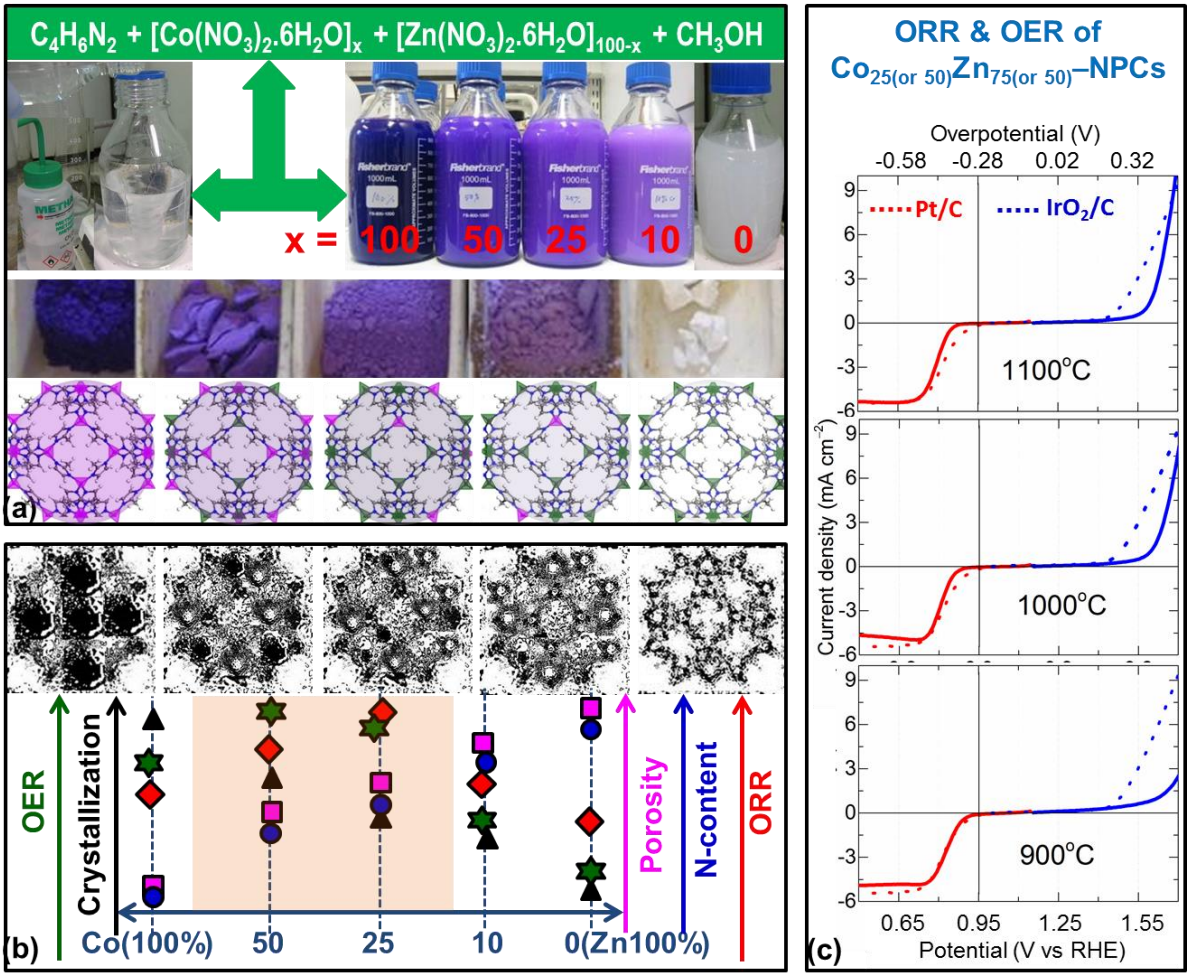

Figure S29. Synthesis, structural and electrochemical characteristics of ZIFs and NPCs: **a)** Sample preparation of Co_xZn_{100-x}–ZIF–8 with a different precursor and metal salt concentrations, x = 100, 50, 25, 10 & 0, respectively, represents from left to right. The precursor solution mixtures in bottles (top row) and ZIF powders (middle row), and local pore structures (bottom row), respectively are represented with digital photographs and wire-frames of ligand and metal-centres. Colour codes: grey-carbon, blue-nitrogen, white-hydrogen, pink-cobalt, and green-zinc. **b)** Characteristic, structure-property relationships of carbonized products of Co_xZn_{100-x}–ZIF–8. Note that evaporation of Zn metal (at 910 °C) results remains open framework, high porosity, and amorphous carbon structure. Continuous introduction of Co metal results in cobalt embedded (black spots), graphitized structure of reduced porosity and N-content. The best ORR and OER properties are observed at intermediate Co/Zn concentrations than simple Co–or Zn–ZIF–8 derived ones. **c)** Electrochemical performance of the optimized NPCs with high activity for ORR at ≤900 °C (equivalent to Pt/C) and high activity for OER at ≥1000 °C (lower or equal overpotentials IrO_2/C [Ref. Sa13] at benchmark current density of 10 mA cm^{-2}).

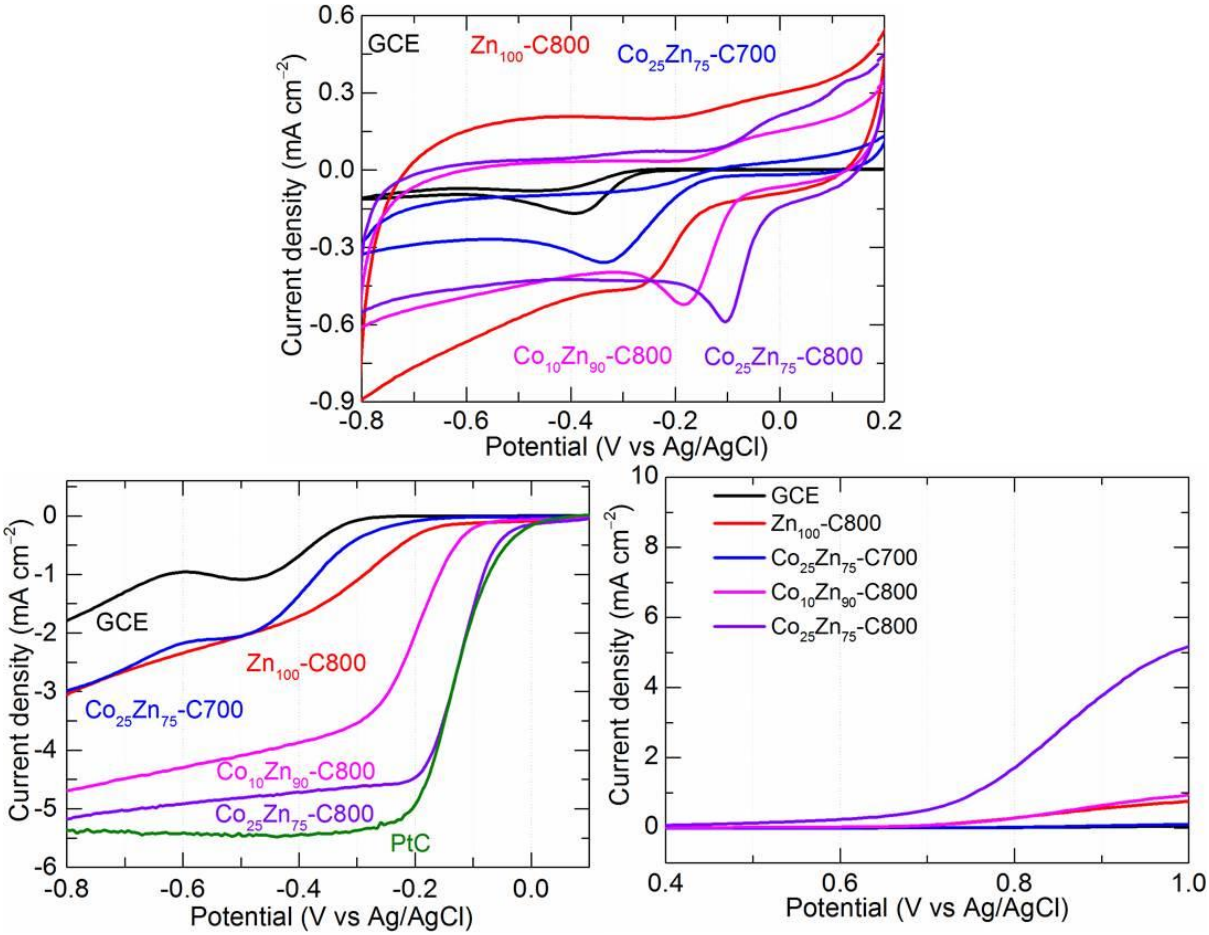

Figure S30. Influence of cobalt-substitution on electrocatalytic activity of NPCs derived at 700 °C and 800 °C for 10 h. A considerably enhanced ORR and OER (at 1600 rpm) activity is seen with increasing the cobalt substitution at a given same synthesis temperature of 800 °C. For example, the Zn_{100}-C800 without cobalt shows a poor ORR or OER performance. The slow increase in current density of LSV curves suggests a two-electron reduction reaction of O_2 to OOH^- (see **Figure S7**). In contrast, the $Co_{25}Zn_{75}$-C LSV curves show a sharp increase and reach saturation. The ORR LSV curves also show a more positive half-wave potential equivalent to the commercial Pt/C thus indicating a significant enhancement in catalysis dominated by a four-electron (4e) process and O_2 is reduced to OH^- (see **Figure S7**). The ORR activity is also identified at CV curves with developing cathodic current density shifting towards a more positive potential. The bare glassy carbon electrode (GCE) is also measured. Except $Co_{25}Zn_{75}$-C800 sample, all other samples show no catalytic activity for OER.

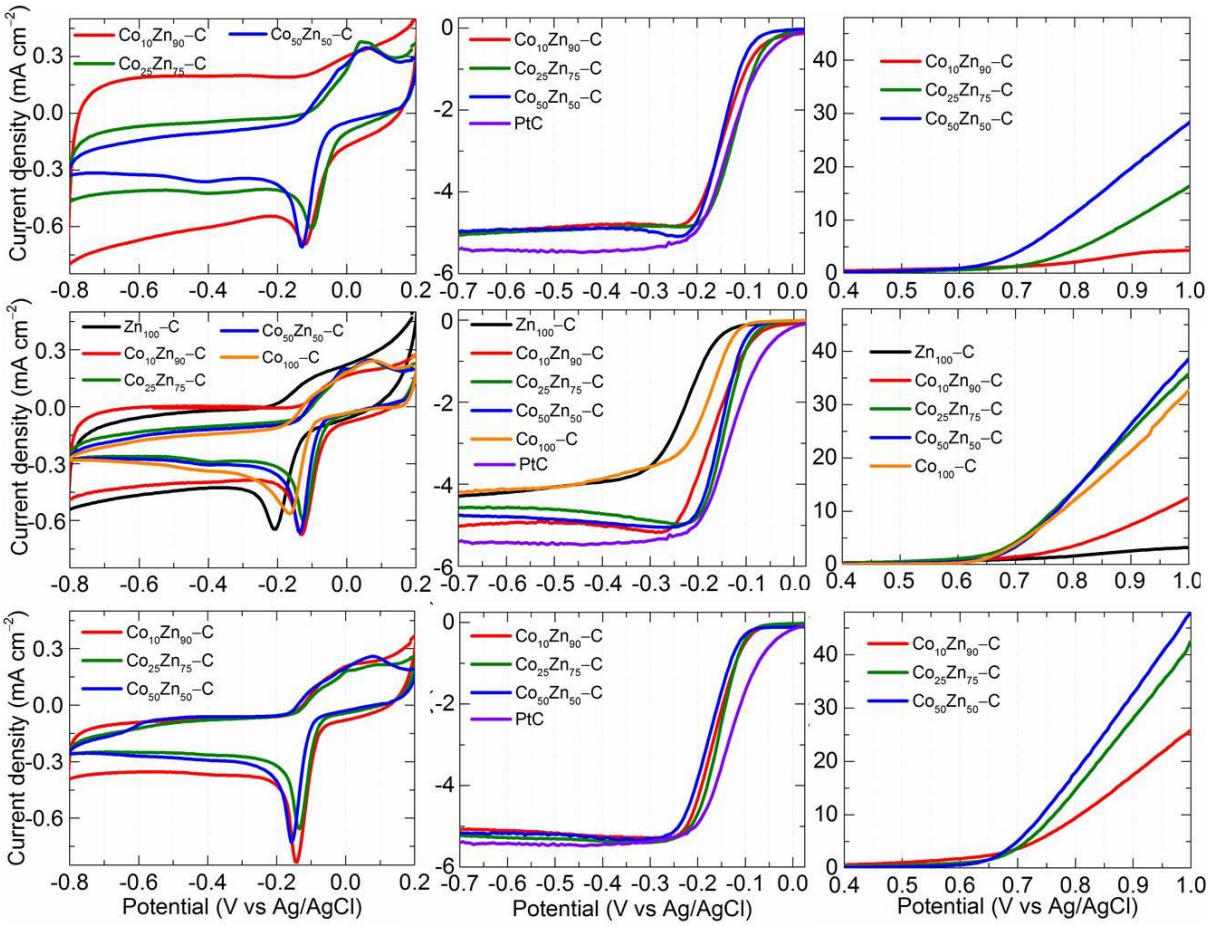

Figure S31. ORR and OER catalytic performance of the Co_xZn_{100-x}-NPCs; the sample are grouped together with same carbonization temperature of 900 °C, 1000 °C and 1100 °C for 10 h, respectively from top, middle and bottom panels. In each case going from left to right shows CV, ORR LSV (at 1600 rpm) and OER LSV (at 1600 rpm) curves. The best ORR performance (see the onset LSV and CV cathodic current peak potentials at more positive side) is observed for $Co_{25}Zn_{75}$-NPCs at any carbonization temperature. The onset and half-wave potentials of LSV curves of $Co_{25}Zn_{75}$-C900 are very close to the commercial Pt/C. Also note that increase in carbonization temperature show shift in onset ORR potentials towards more negative side, but without any considerable change in limiting current density and slopes or half-wave potentials meaning that the samples still show a definite 4e reaction mechanism (**Figure S33**). Whereas, compared to the 900 °C samples the 1000 °C and 1100 °C carbonized samples show highly enhanced OER performance. Also note that the concentration of cobalt is the key at particular synthesis temperature. The best performance for ORR is seen at 900 °C carbonized sample, $Co_{25}Zn_{75}$-C900-10h and best OER is seen for 1100 °C carbonized sample, $Co_{50}Zn_{50}$-C1100-10h.

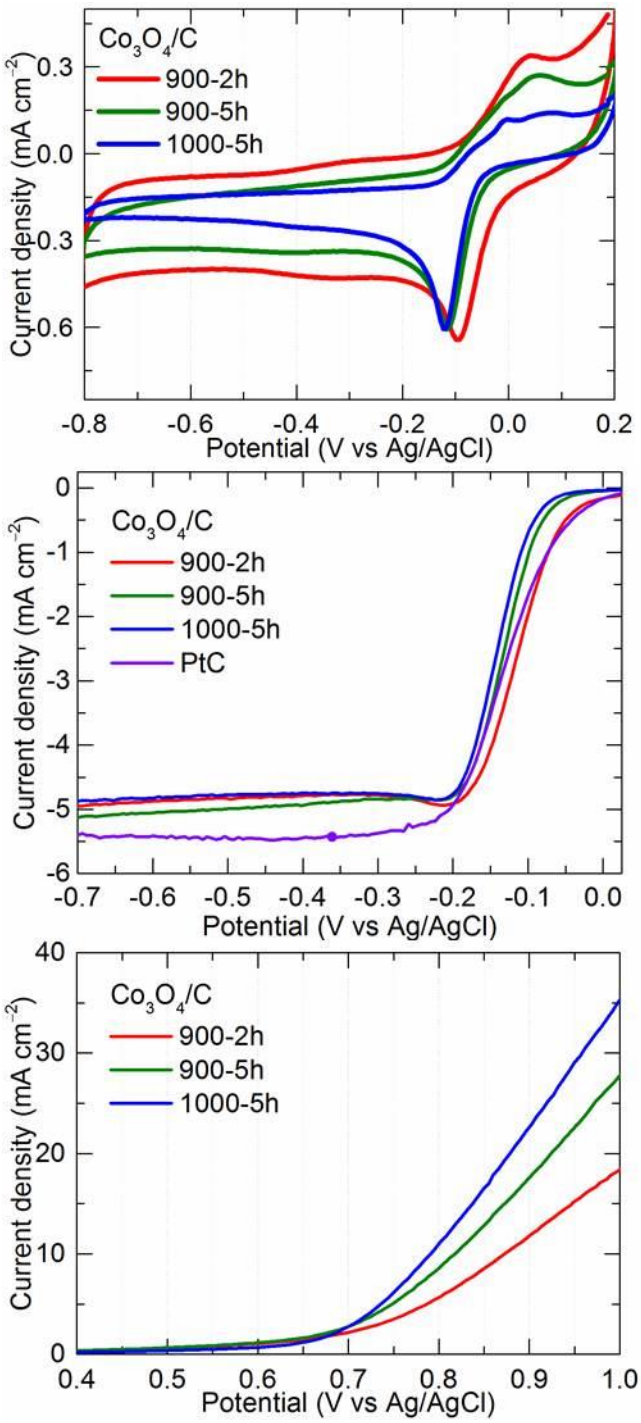

Figure S32. CV curves of $Co_{25}Zn_{75}$-NPCs at 900 °C and 1000 °C synthesized by control oxidation. The effect of increased carbonization time and temperature is clearly seen, which is directly attributed to the simultaneous loss of nitrogen-content, graphitization and loss of porosity. Clearly, more nitrogen content in 2h carbonized sample at 900 °C exhibits best ORR activity, whereas increased graphitization dramatically enhances the OER performance (see 1000 °C).

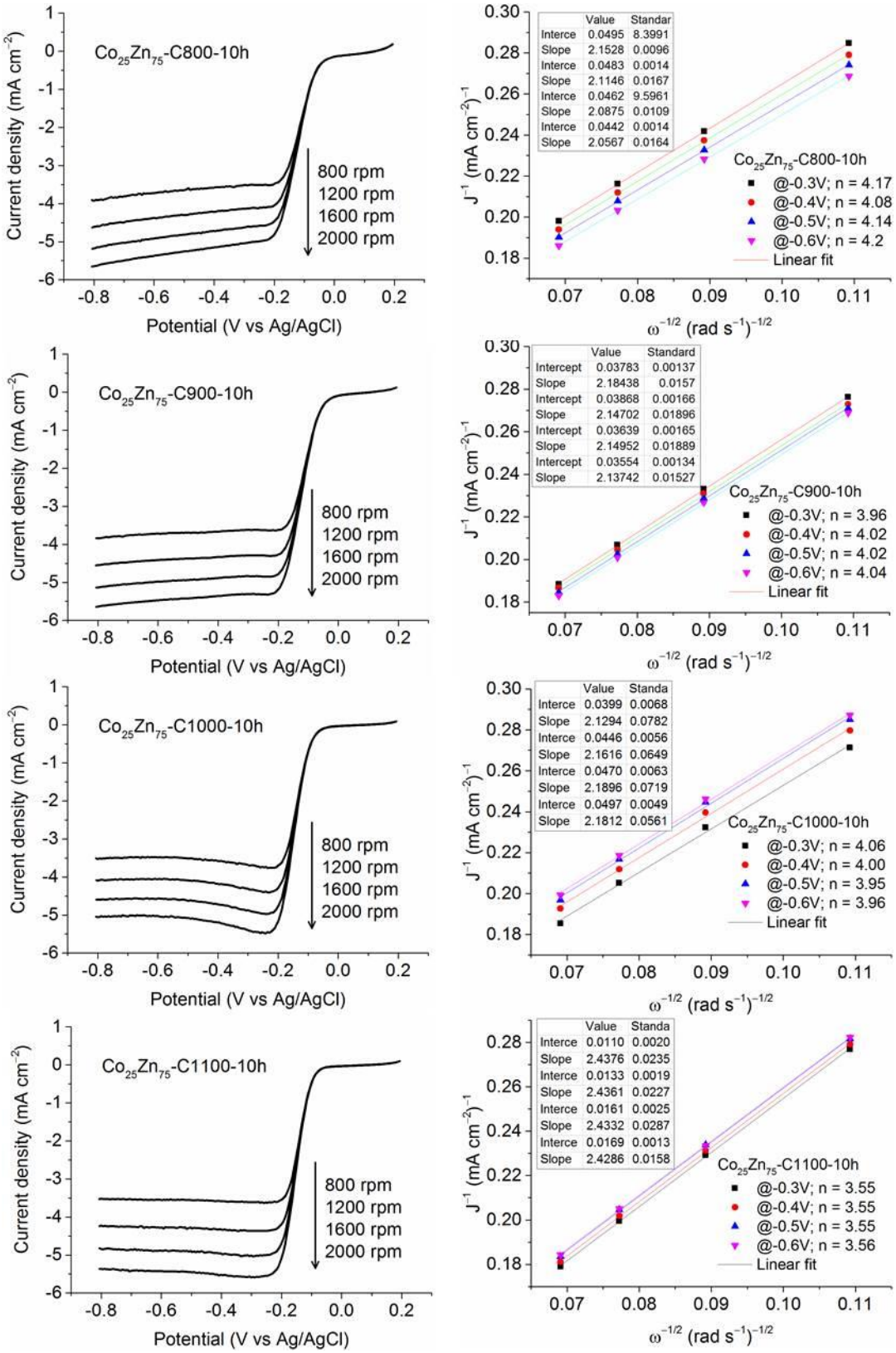

Figure S33. ORR LSV curves at different rotating speeds (left panel) and its derived Koutechy-Levich plots with linear fittings at different potentials in the equilibrium region (right panel) for $Co_{25}Zn_{75}$-NPCs synthesized at (800, 900, 1000 and 1100) °C for 10 h (in a sequence of top to bottom).

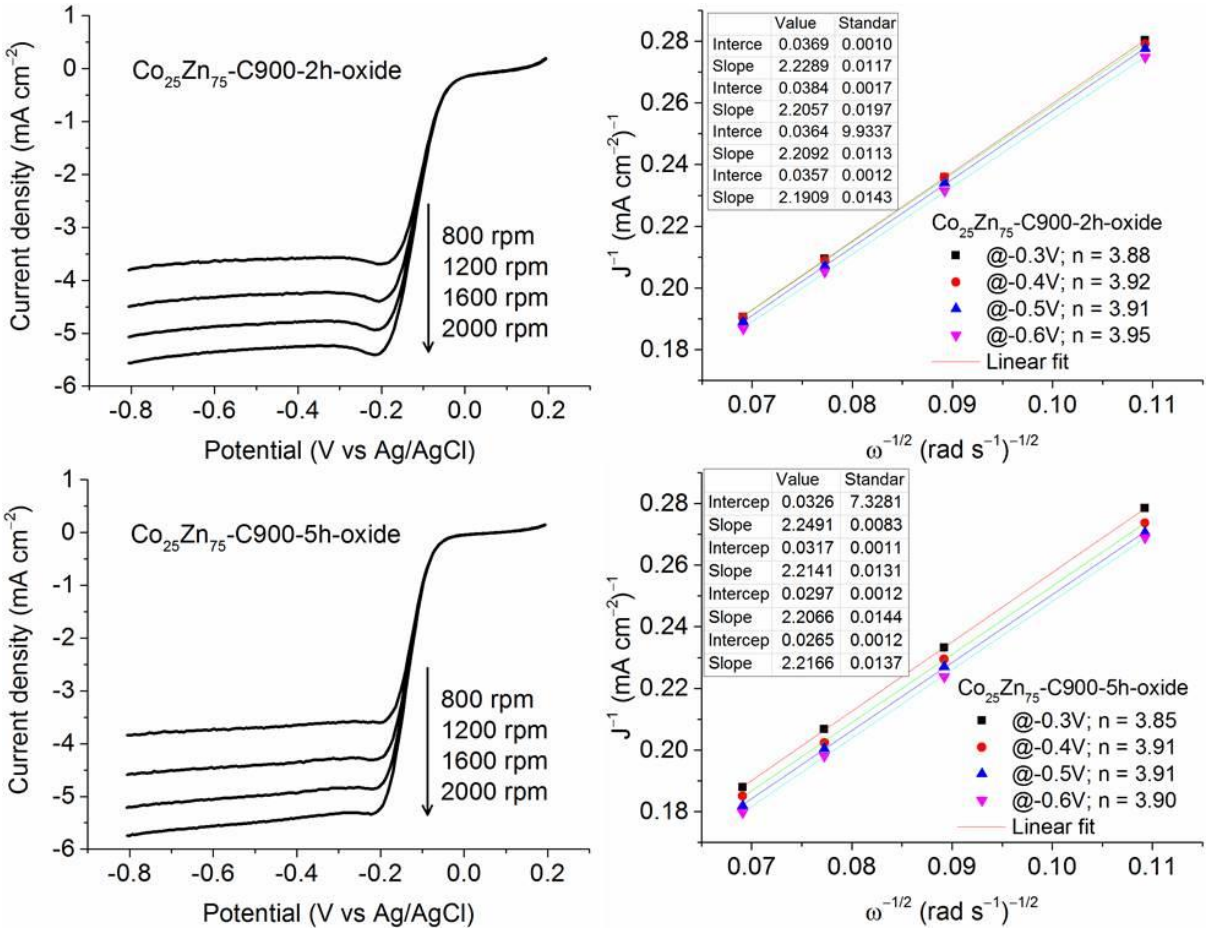

Figure S34. ORR LSV curves of Co_3O_4/C NPCs derived from $Co_{25}Zn_{75}$-C900 (represented with –oxide) (left panel) and its derived Koutechy-Levich plots with linear fittings at different potentials in the equilibrium region (right panel).

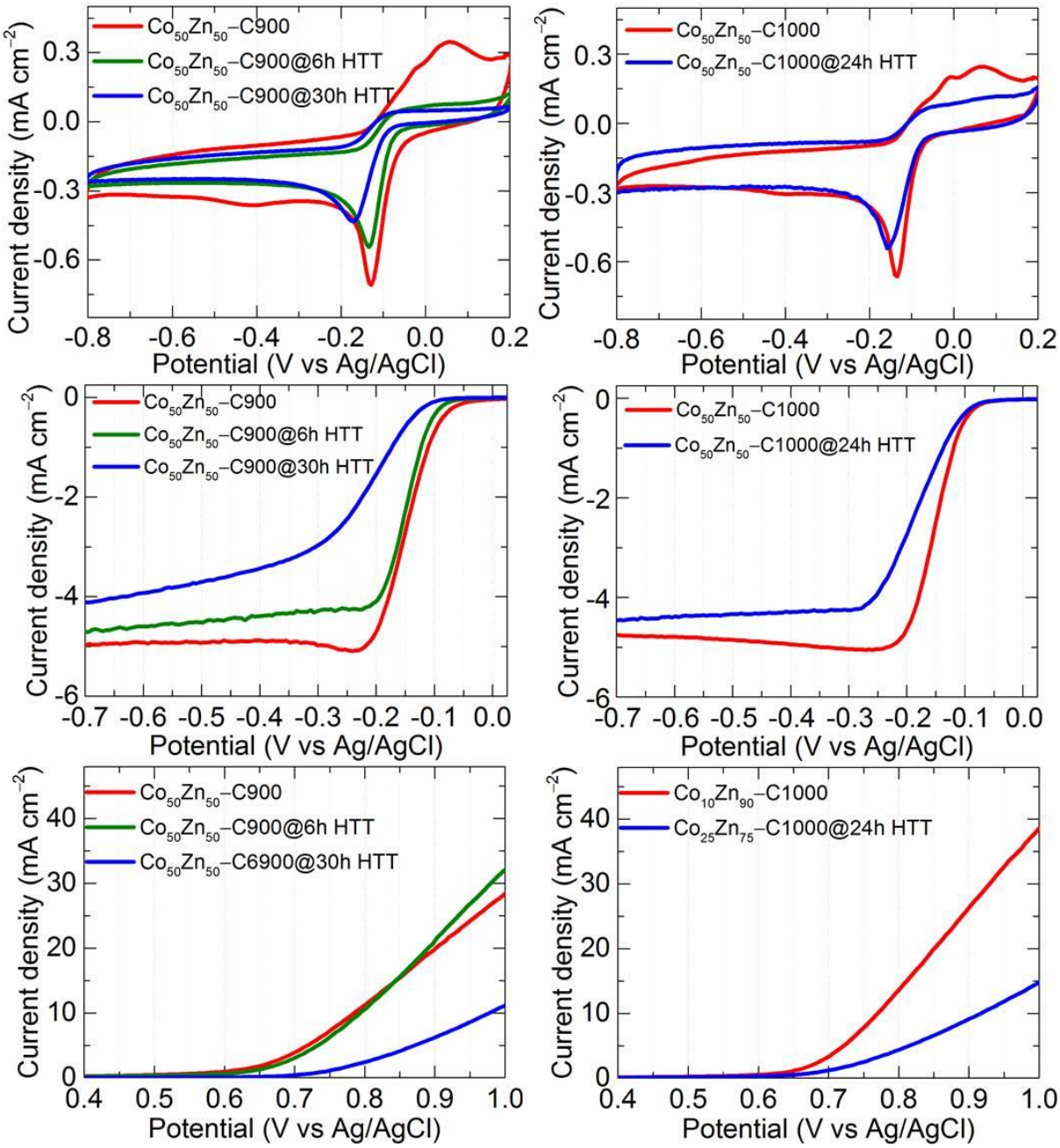

Figure S35. ORR (top and middle) & OER (bottom) performance of hydrothermally treated (HTT) $Co_{50}Zn_{50}$-C900-10h (left panel) & $Co_{50}Zn_{50}$-C1000-10h (right panel). The reduced performance of HTT carbons is seen at both the ORR and OER plots, which are characterized by shift of the CV cathodic current peak and LSV onset reduction to a more negative (or positive for OER) potentials, reduced current density at both ORR and OER. All the CV and LSV curves were measured with a potential sweep at 10 mV s^{-1}. The LSV curves for ORR and OER are shown at 1600 rpm. The increased surface oxide layer thickness on the cobalt core, i.e., CoO@Co-NPCs, reduces the performance for both the ORR [is in good agreement with the Guo et al. [Ref. Sa14] and OER.

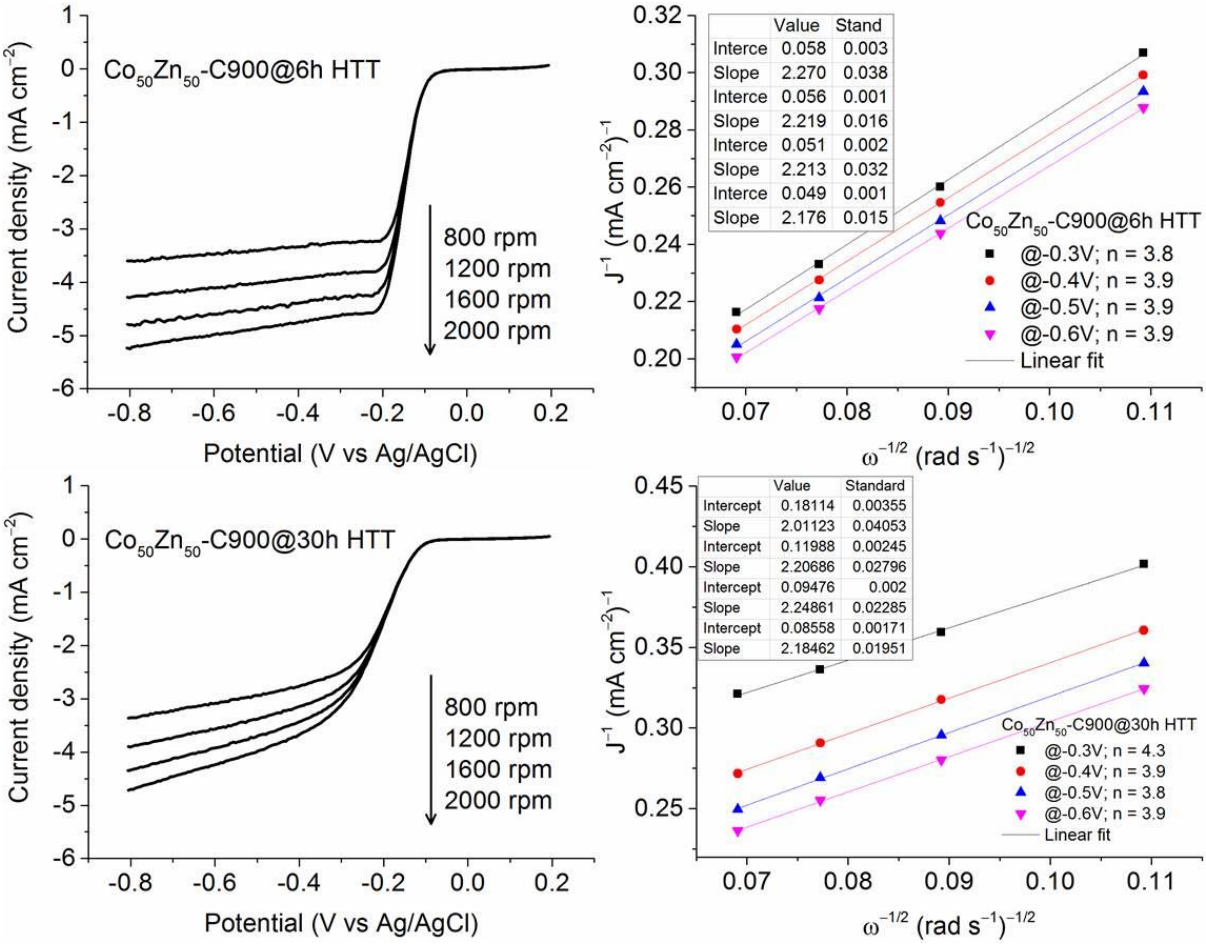

Figure S36. ORR LSV curves (left panel) and its derived Koutechy-Levich plots with linear fittings at different potentials in the equilibrium region (right panel) for post-synthesis hydrothermally treated $Co_{50}Zn_{50}$-C900-10h. Note that still it exhibits a 4e ORR but with considerably reduced limiting current density, and enhanced onset and half-wave potential and slope of the curves.

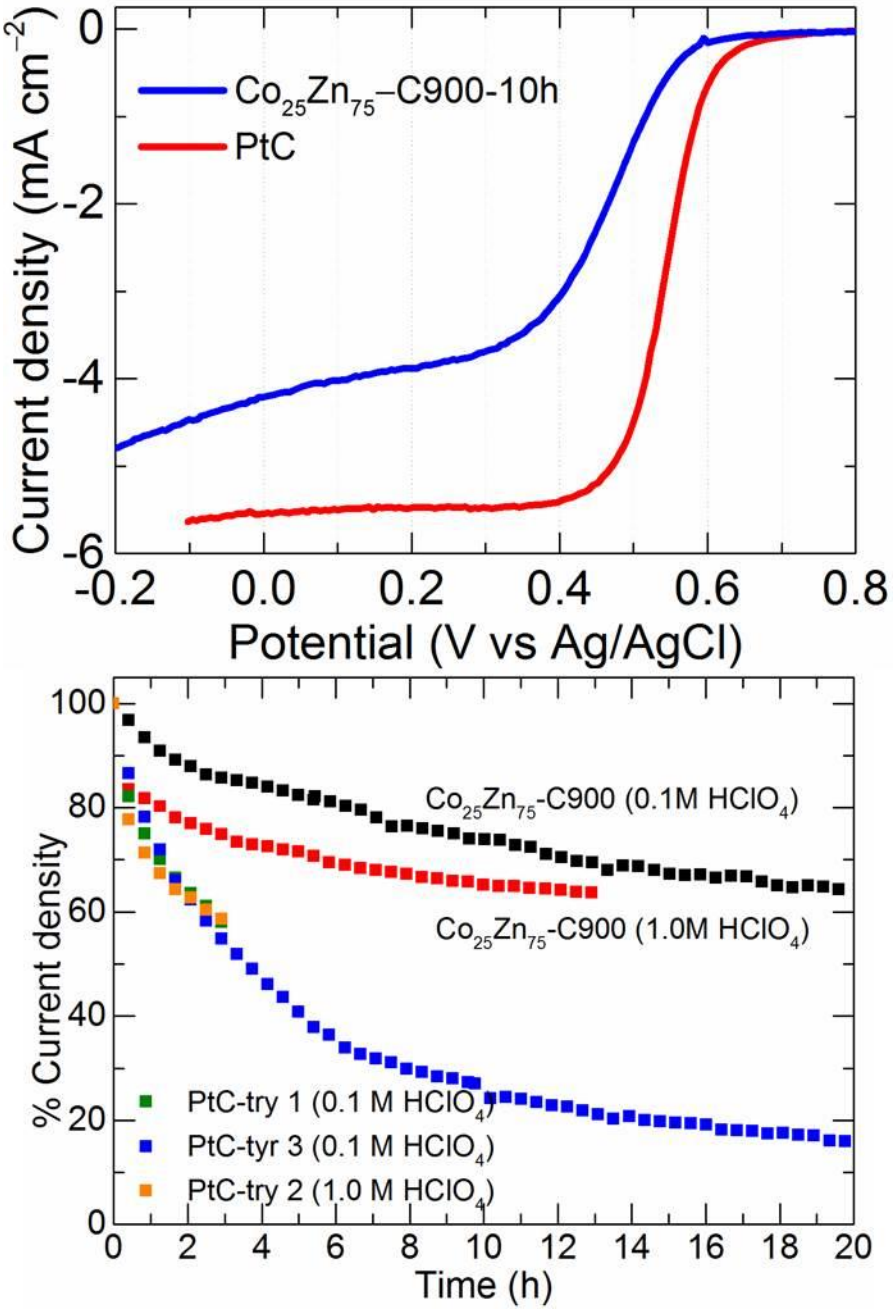

Figure S37. ORR response of $Co_{25}Zn_{75}$-C900 and reference PtC in acidic ($HClO_4$) electrolyte: LSV curves at 1600 rpm with a scan rate of 10 mV s^{-1} in 0.1M $HClO_4$ (top) and stability (current density vs time) response measured at 0.3 V (vs Ag/AgCl in 0.1M and 1.0M $HClO_4$) and 1600 rpm (bottom) [Ref. Sd4].

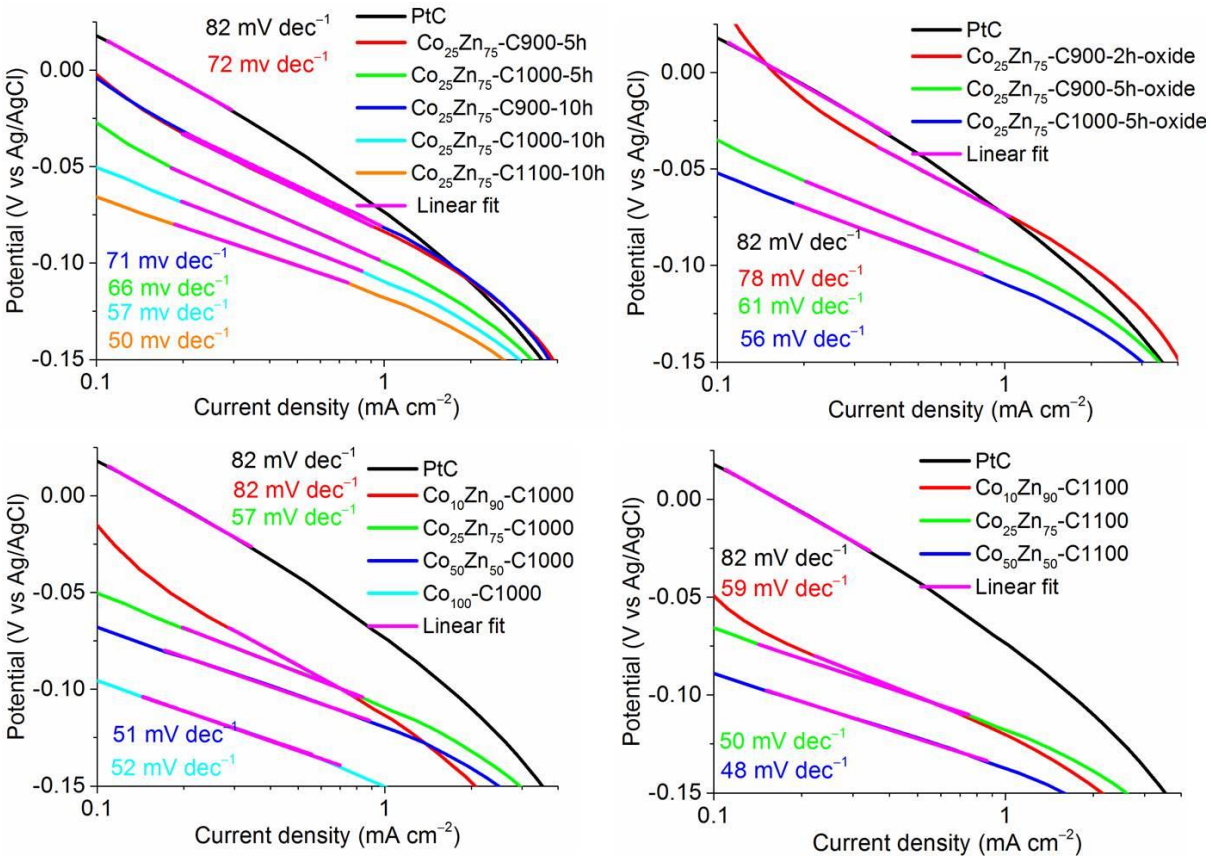

Figure S38. Tafel plots (applied potential vs log(current density) of OER LSV at 1600 rpm) of Co_xZn_{100-x}–NPCs. Top: left & right shows $Co_{25}Zn_{75}$–NPCs (with different carbonization conditions) without & with controlled oxidation (represented with –oxide). Bottom: left and right shows Co_xZn_{100-x}–C1000-10h and Co_xZn_{100-x}–C1100-10h, respectively. The Tafel slopes are identified with linear fittings in purple colour. See that all the NPCs exhibit much smaller slopes than Pt/C standard, indicating rapid reduction kinetics.

Table S5. The linear fitting parameters and electron transfer number in O_2 reduction, derived from Koutecky-Levich plots at different potentials between −(0.3 and 0.6) V vs Ag/AgCl. The control oxidation of samples is represented with –oxide (which is nothing but Co_3O_4/C).

S. No.	Sample	Potential (V vs Ag/AgCl)	Linear fitting parameters		n, electron transfer
			Slope	Intercept	
1	Pt/C	−0.3	2.13	0.021	4.06
		−0.4	2.17	0.016	3.98
		−0.5	2.17	0.016	3.98
		−0.6	2.23	0.012	3.87
2	Zn_{100}-C900-6h	−0.4	2.68	0.094	3.22
		−0.5	2.44	0.087	3.55
3	Co_{100}-C900-6h	−0.4	2.33	0.028	3.71
		−0.5	2.28	0.033	3.79
4	Zn_{100}-C1000-10h	−0.4	2.78	0.038	3.11
		−0.5	2.69	0.038	3.22
		−0.6	2.61	0.037	3.32
5	Co_{100}-C1000-10h	−0.4	2.34	0.077	3.69
		−0.5	2.32	0.066	3.73
		−0.6	2.30	0.065	3.77
6	$Co_{25}Zn_{75}$-C800-10h	−0.3	2.15	0.049	4.01
		−0.4	2.11	0.048	4.09
		−0.5	2.09	0.046	4.14
7	$Co_{25}Zn_{75}$-C900-2h-oxide	−0.3	2.23	0.037	3.88
		−0.4	2.21	0.038	3.92
		−0.5	2.21	0.036	3.91
		−0.6	2.19	0.036	3.95
8	$Co_{25}Zn_{75}$-C900-5h-oxide	−0.3	2.25	0.033	3.85
		−0.4	2.21	0.032	3.91
		−0.5	2.21	0.030	3.92
		−0.6	2.22	0.026	3.90
9	$Co_{25}Zn_{75}$-C900-5h	−0.3	2.26	0.036	3.83
		−0.4	2.26	0.041	3.83
		−0.5	2.24	0.042	3.86
		−0.6	2.23	0.041	3.88
10	$Co_{25}Zn_{75}$-C900-10h	−0.3	2.18	0.038	3.96
		−0.4	2.15	0.039	4.03
		−0.5	2.15	0.036	4.02
		−0.6	2.14	0.036	4.05
11	$Co_{25}Zn_{75}$-C1000-10h	−0.3	2.13	0.040	4.06
		−0.4	2.16	0.045	4.00
		−0.5	2.19	0.047	3.95
		−0.6	2.18	0.050	3.97
12	$Co_{25}Zn_{75}$-C1100-10h	−0.3	2.44	0.011	3.55
		−0.4	2.44	0.013	3.55
		−0.5	2.43	0.016	3.55
		−0.6	2.43	0.017	3.56

Table S6. Half-wave potentials of ORR LSV curves at 1600 rpm. The control oxidation of samples is represented with –oxide (which is nothing but Co_3O_4/C).

Sample	Half-wave potential (mV)
Pt/C	72.0
Zn_{100}–C1000-10h	67.0
Co_{100}–C1000-10h	58.0
$Co_{25}Zn_{75}$–C900-2h-oxide	58.0
$Co_{25}Zn_{75}$–C900-5h	53.0
$Co_{25}Zn_{75}$–C900-10h	56.0
$Co_{25}Zn_{75}$–C1000-5h	52.0
$Co_{25}Zn_{75}$–C1000-10h	48.0
$Co_{25}Zn_{75}$–C1100-10h	45.0

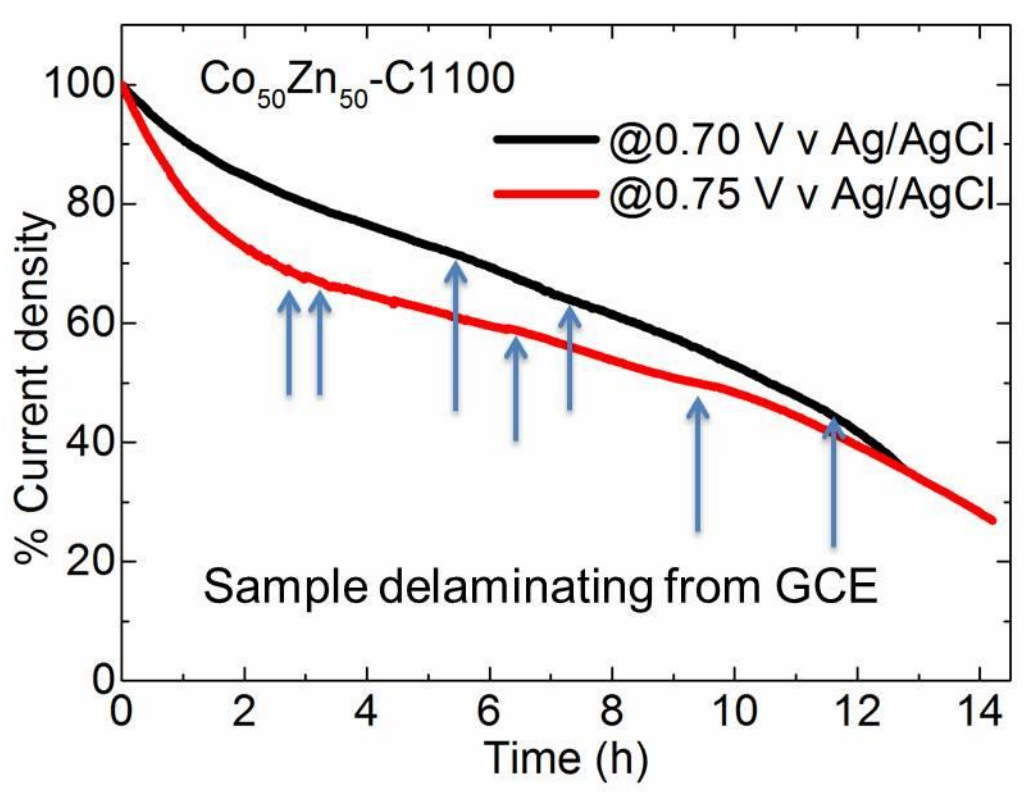

Figure S39. OER stability (current vs time chronoamperometric response) of $Co_{50}Zn_{50}$-C1100-10h recorded with applied potential of 0.70 and 0.75 V vs Ag/AgCl and rotating speed of 1600 rpm in 0.1M KOH.

The arrow marks show possibly detachment of the sample from the GCE (glassy carbon electrode). This problem is also reported by Xie et al. [ref Sa15]. It is attributed to the bubble formation and release. See that increased potential makes it easier detachment as it can produce more O_2. It is suggested that other methods, example a graphite electrode can prevent the detachment of catalyst layer thus the long-time measurement is possible.

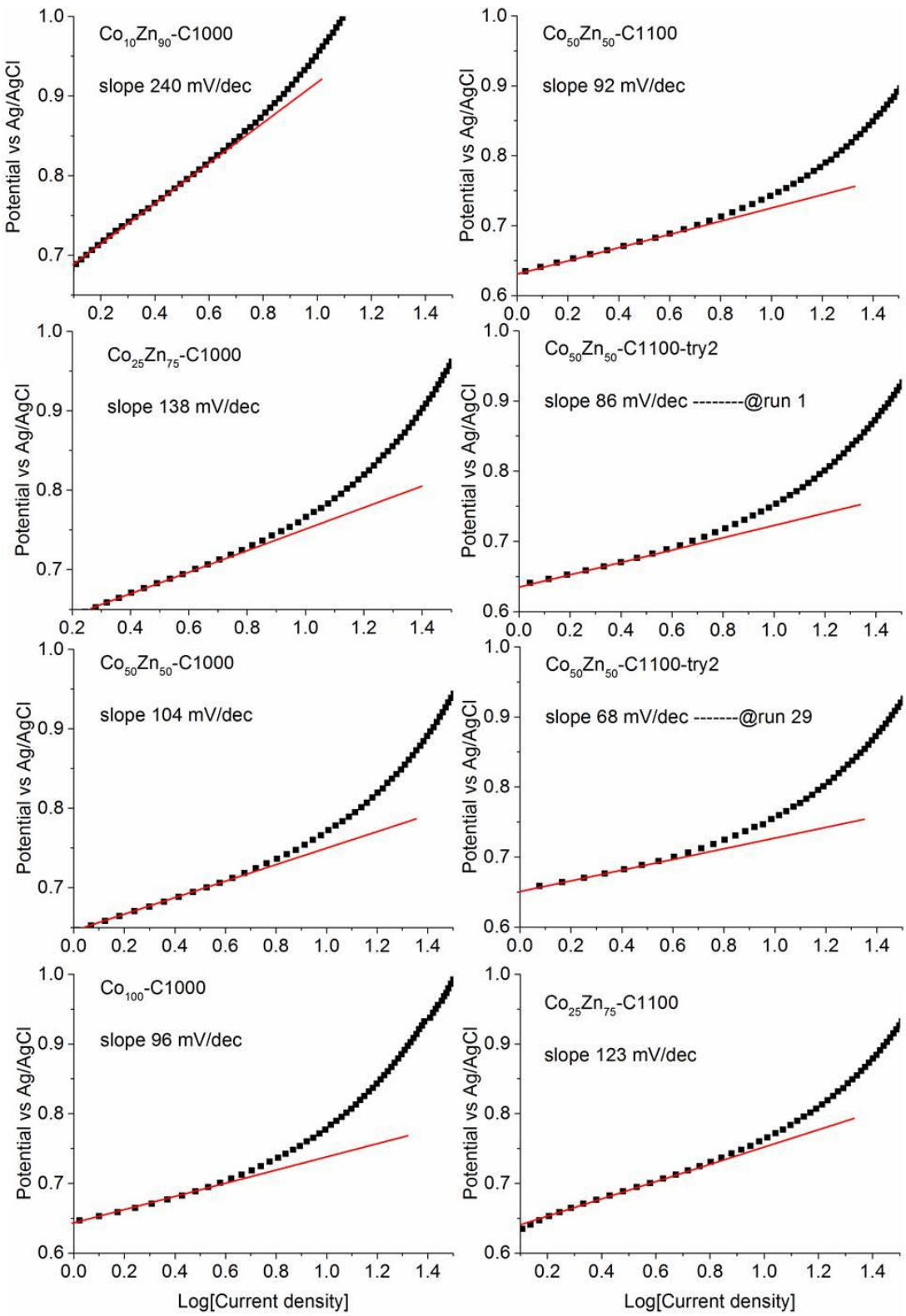

Figure S40. Tafel plots of OER LSV at 1600 rpm in 0.1M KOH: left panel is for Co_xZn_{100-x}-C1000-10h and right panel is for $Co_{50}Zn_{50}$-C1100-10h (try 1 and try 2 samples) & $Co_{25}Zn_{75}$-C1100-10h. See that at 1000 °C, a continuous drop in slope is seen with increasing cobalt-concentration.

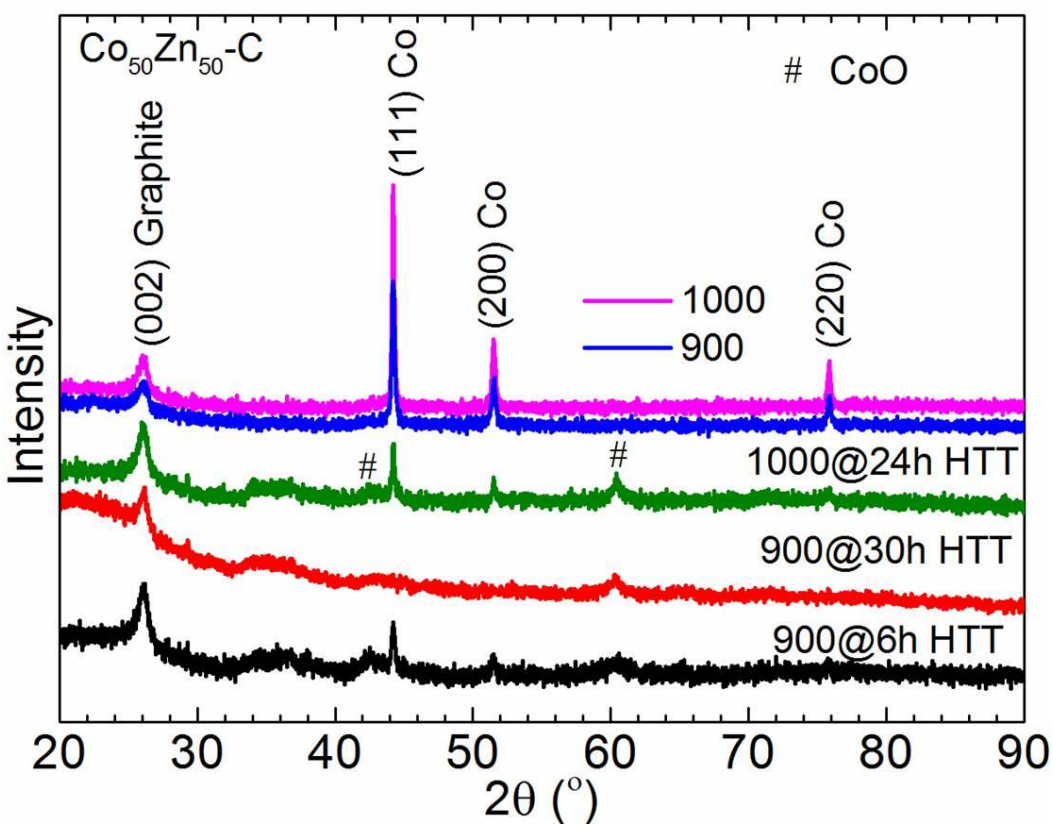

Figure S41. PXRD patterns of hydrothermally treated $Co_{50}Zn_{50}$-C900-10h & $Co_{50}Zn_{50}$-C1000-10h, the reduced intensity of fcc Co(0) is attributed to the surface grown cobalt(II) oxide, CoO layer, which is further seen at appearance of weak diffraction peaks, identified with #.

DFT Calculations & Discussion

Computational Method

The interaction of O_2 and the various reaction intermediates during the ORR reaction was determined using periodic Density Functional Theory (DFT), using the VASP code [Ref. Sf1]. A plane wave cutoff of 520 eV was selected, with the Projector Augmented Wave methods used to treat the core electrons [Ref. Sf2]. The GGA+*U* functional was used for structure optimization, thermodynamic calculation, and electronic structure analysis [Ref. Sf3]. As the 3*d* shell of the cobalt atom is strongly interacting, the *U* term was used to include the on-site repulsion energy. We use a *U* value of 4.0 eV, as this was found to accurately describe the electronic and magnetic structure of the cobalt carbide compounds Co_2C and Co_3C [Ref. Sf4]. Furthermore, as we use the Dudarev variant of the functional, our *U–J* value of 4.0 eV is very similar to that used by Jakob and Kotliar [Ref. Sf5]. Van der Waals interactions were included via the usage of the DFT-D2 method of Grimme *et al* [Ref. Sf6]. All atoms were fully relaxed until the change in force upon ionic displacement was less than 0.01 eV/Å, with the change in energies no greater than 10^{-5} eV. A monolayer of graphene was used to represent the carbon surface, we use a (6×6×1) hexagonal supercell formed from the primitive unit cell and composed of 72 carbon atoms. The lattice parameter of graphene was found to be 2.470 Å, and overestimate of 0.35% with experimental data and thus in very close agreement. All calculations were spin-polarised.

In order to model the ORR free energy diagram, we calculated structures and thermodynamics for the following processes:

$X+O_2(g) + (4H^+ + 4e^-) \leftrightarrow XO_2 + (4H^+ + 4e^-)$

$XO_2 + (4H^+ + 4e^-) \leftrightarrow XOOH + (3H^+ + 3e^-)$

$XOOH + (3H^+ + 3e^-) \leftrightarrow XO + H_2O + (2H^+ + 2e^-)$

$XO + H_2O + (2H^+ + 2e^-) \leftrightarrow XOH + H_2O + H^+ + e^-$

$XOH + H_2O + H^+ + e^- \leftrightarrow X + 2H_2O$

where X is the initial substrate structure (ideal graphene, Co_{DV}+N, or Co_{DV}+4N). The energies of O_2 and H_2O were taken in the gas phase, whereas the energy of $(H^+ + e^-)$ at pH = 0 and $V = 0$ was taken to be that of ½ H_2 [Ref. Sf7]. The energies at an applied potential V were corrected by $E(V) = E - neV$.

Results & Discussion

In order to ascertain what the particular mechanism is behind the unprecedented efficacy of this cheap electrocatalyst composed of abundant elements, we used GGA+U density functional theory calculations to determine the reaction pathway, using the method of Norskov *et al.* to determine the energy diagram for ORR for various applied potentials *V* [Ref. Sf7**]**. We do this for ideal graphene and two different structures for the cobalt-nitrogen doping graphene structure that is likely to form following carbonisation of microporous ZIF

at high temperature. Specifically, we consider cobalt and nitrogen incorporation into the carbon as substitution into a graphene lattice, as experiment indicates carbonisation forms graphitic microstructures. Recent theoretical work reports that the lowest energy structures for cobalt dopants involves entrapment inside a two atom carbon vacancy [Ref. Sf8**].** As cobalt has a significantly larger atomic radii than carbon this would ameliorate strain in the surrounding graphene lattice. Furthermore, we consider two different stoichiometries of nitrogen substitutional doping around the cobalt atom, minimal nitrogen doping with one nitrogen atom, (denoted Co_{DV}+N) and maximal nitrogen doping with four nitrogen atoms (denoted Co_{DV}+4N) (**Figure S42**). As there is a significant amount of emission of chemical species through the carbonisation process we expect the graphene lattice to be both defected and nitrogen poor. There is a strong tendency for nitrogen dopants to be adjacent to the cobalt dopant, as nitrogen substitution in the second nearest carbon atom to the dopant is 0.93 eV higher in energy. In the energetics calculations our results do not include entropic effects, but as we find in our calculations that the difference in barrier energies are significant thus the results are still indicative. As we are calculating energetics for ground state reaction intermediates between electron-transfer processes, this estimate for the barrier is a minimum value, the transition states between the stable intermediate will need to be overcome, with an additional energetic penalty.

As shown in **Figure S42** the four electron reduction of O_2 to form H_2O via the association reaction on ideal graphene has a significant barrier, 1.13 eV to form the OOH radical. Furthermore, the formation of OH groups on the graphene via proton attack is an endothermic process, at 1.44 eV above the ground state. This is the rate-determining step. All reaction intermediates are endothermic with respect to product and reactant. In contrast, for the Co_{DV}+4N structure all reaction intermediates are exothermic with respect to reactant and product. The largest activation barrier that needs to be overcome is the formation of OH groups by proton attack of oxygen, at 1.98 eV. The reaction for this structure has a large degree of exothermicity with a maximum energy release of 3.24 eV. As this result in heat release this induces inefficiencies that hinder the reduction process. Surprisingly, the most thermoneutral for ORR and with the smallest activation energy is the Co_{DV}+N structure. The largest barrier for ORR on this structure is the second proton attack of the OH functional group to form H_2O, with a barrier of 0.49 eV. Furthermore, the endothermic formation of the OOH intermediate has a small activation barrier of 0.22 eV. With the Sabatier criteria the kinetics are maximised when energy differences are minimized [Ref. Sf9]. Therefore the Co_{DV}+N structure has the best kinetics for electrochemical reduction of O_2 as the overall process is most thermoneutral

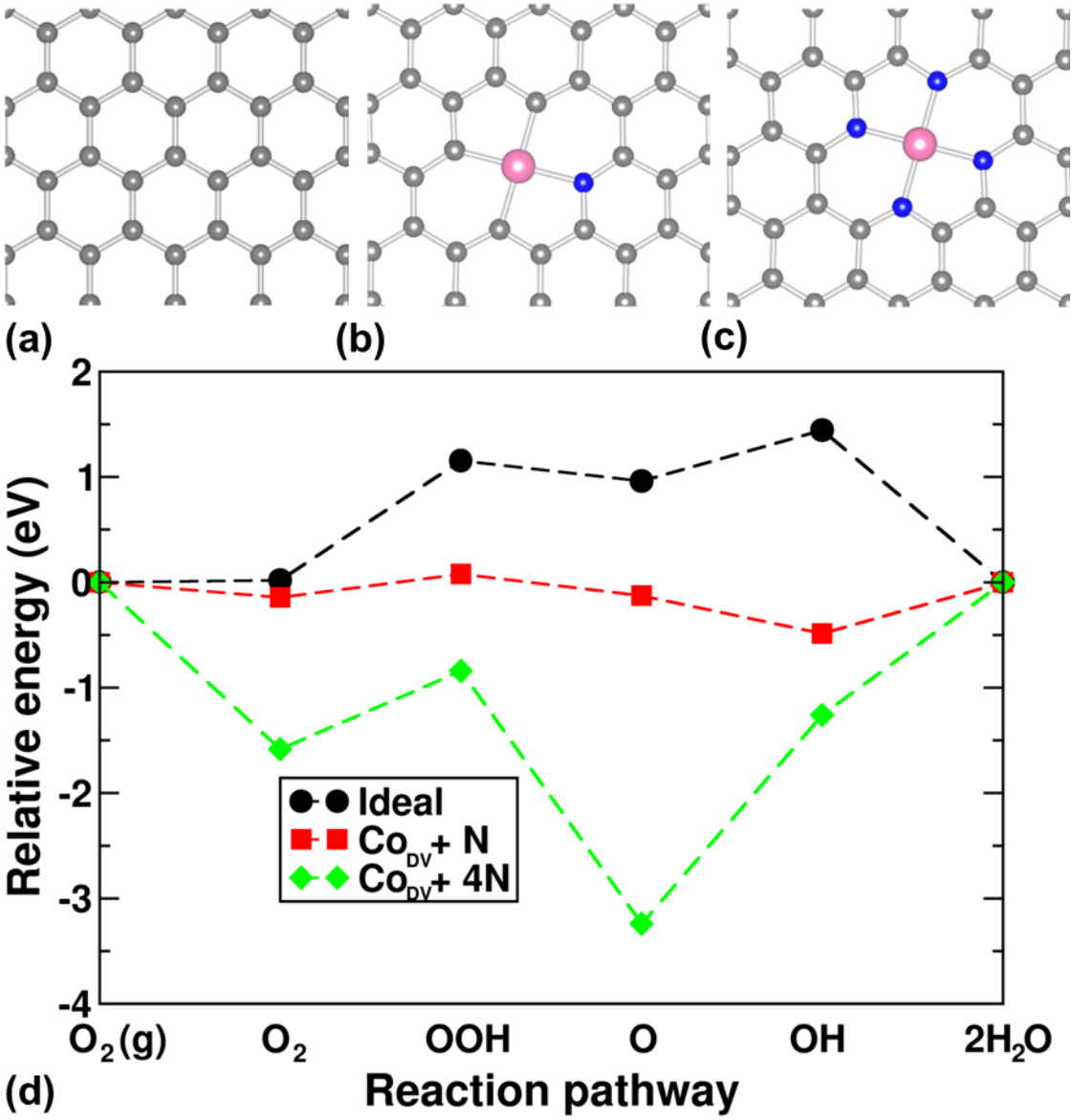

Figure S42. Atomic structures of the three model systems, **a)** ideal graphene, **b)** Co_{DV}+N, and **c)** Co_{DV}+4N. Carbon, cobalt and nitrogen atoms are represented by grey, pink and blue spheres, respectively. **d)** Energy diagram for ORR reaction for potential where product and reactant thermodynamics are the same, V = 1.265 V. Negative energies indicate exothermicity while positive energies indicate endothermicity. The electrochemical reaction proceeds from gaseous O_2 (left-hand-side), binding of the O_2, formation of the OOH, removal of OH^- with resulting single O atom bound to graphene, formation of OH by proton attack, and formation of H_2O (right-hand-side).

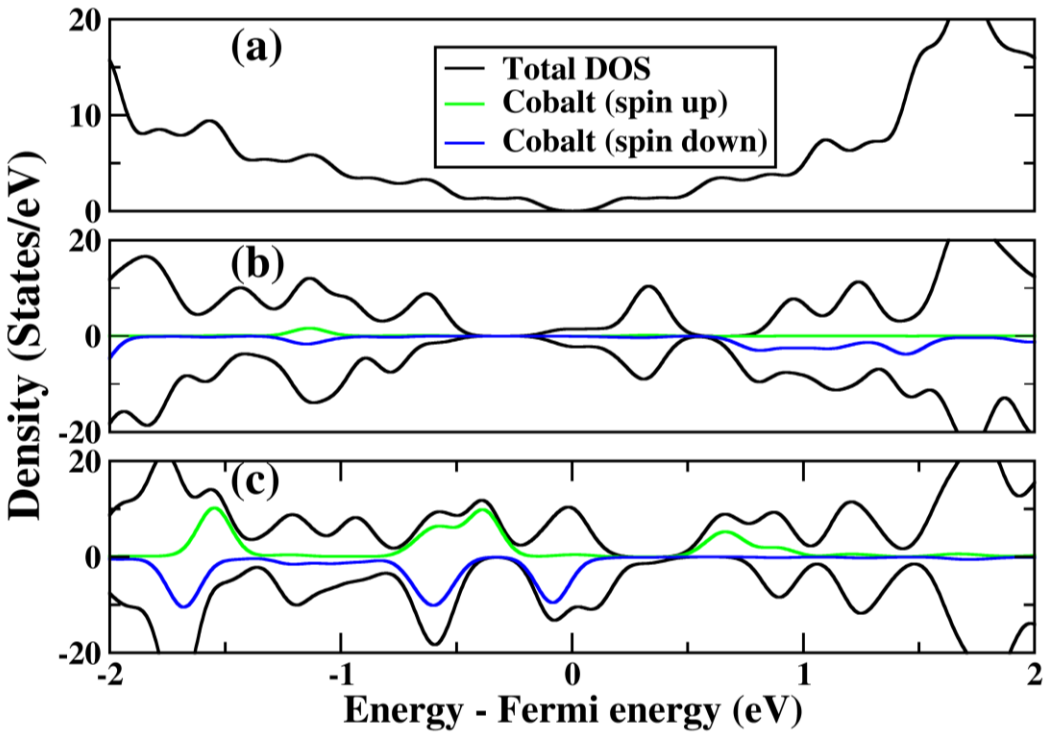

Figure S43. DOS plots for ideal graphene (a), Co_{DV}+N (b), and Co_{DV}+4N (c).

In order to determine the atomistic rationale behind this we calculated the DOS and the partial atomic charge using the Bader analysis for all three initial structures and the corresponding OH-binding structures [Ref. Sf10]. The cobalt atom has a larger positive charge in the Co_{DV}+N structure than in the Co_{DV}+4N structure, at +0.90 vs +0.74 *e* respectively. This reflects how in the latter structure the cobalt atom is surrounded by four electronegative nitrogen atoms that extract electronic density from the surrounding graphene lattice strongly, they are thus less likely to accept electronic density from the cobalt atom. Upon binding of the OH functional group to the graphene or cobalt-doped graphene the situation changes considerably. On the ideal graphene the oxygen atom of the hydroxyl group has a charge of –0.92*e*, whereas for the Co_{DV}+N structure and for the Co_{DV}+4N structure the oxygen atom has a charge of –1.04*e*. The oxygen atom extracts electronic density from the substrate, whether the graphene lattice or the cobalt dopant. For the former case this is clearly highly endothermic, resulting in the large endothermic energy of the intermediate. For the latter case the anion charge transfer would result from the cobalt dopant, resulting in a more exothermic binding energy. Importantly, there is much more charge transfer from the cobalt dopant in the Co_{DV}+4N model than the Co_{DV}+N model, the cobalt atom now has a charge of +1.11*e* for the former structure compared to +0.96*e* for the latter model. As the cobalt is more "metallic" in the original Co_{DV}+4N structure, it is more reactive than the Co_{DV}+N structure, hence the greater exothermicity of this reaction intermediate in the former structure. Further evidence of the combined effect of the cobalt and nitrogen dopants is demonstrated in the DOS, see **Figure S43.** Ideal graphene has little state density near the Fermi level, thus demonstrating the stability and the endothermicity for OH-binding or other reaction intermediate binding. The Co_{DV}+N structure has more state density near the Fermi level than the graphene, indicating a greater degree of reactivity, while the Co_{DV}+4N

structure has the most state density near the Fermi level, with a greater associated binding strength. Furthermore, the Co_{DV}+4N structure has a greater degree of cobalt state density present near the Fermi level, reflecting the increased reactivity of the cobalt atom due to the reduced and more metallic like nature of the atom in this structure. From the DOS and Bader analysis we find that nitrogen shields the cobalt dopant, allowing tuning of binding energy of reaction intermediates with respect to nitrogen content.

Table S7

Zero temperature energy diagram data (*V*=0)

System	Bare+2H_2O	Bare+O_2(g)	O_2 bind	OOH bind	O bind	OH bind
Ideal	-696.321382	-691.257692	-691.237522	-691.369423	-692.828585	-693.610591
Co_{DV}+N	-676.527455	-671.463765	-671.608291	-672.651440	-674.122570	-675.748050
Co_{DV}+4N	-676.652975	-671.589285	-673.172988	-673.695787	-677.361774	-676.647312

Table S8

Zero temperature energy diagram data (Corrected for equilibrium voltage *V* = 1.2659)

System	Bare+2H_2O	Bare+O_2(g)	O_2 bind	OOH bind	O bind	OH bind
Ideal	-696.3213	-696.3213	-696.30112	-695.16712	-695.360385	-694.876491
Co_{DV}+N	-676.527455	-676.527455	-676.671891	-676.449140	-676.654370	-677.013950
Co_{DV}+4N	-676.652975	-676.652975	-678.236588	-677.493487	-679.893574	-677.913212

Additional References

a.

1. J. Cravillon, R. Nayuk, S. Springer, A. Feldhoff, K. Huber, M. Wiebcke, Controlling zeolitic imidazolate framework nano- and microcrystal formation: insight into crystal growth by time-resolved in situ static light scattering, **Chem. Mater. 2011, 23, 2130.**
2. H. B. Wu, S. Wei, L. Zhang, R. Xu, H. H. Hng, X. W. Lou, Embedding sulfur in MOF-derived microporous carbon polyhedrons for lithium–sulfur batteries, **Chem. Eur. J. 2013, 19, 10804.**
3. W. Xia, R. Zou, L. An, D. Xia and S. Guo, A metal–organic framework route to in situ encapsulation of Co@Co_3O_4@C core@bishell nanoparticles into a highly ordered porous carbon matrix for oxygen reduction, **Energy Environ. Sci. 2015, 8, 568.**
4. J. Wang, K. Li, H. Zhong, D. Xu, Z. Wang, Z. Jiang, Z. Wu and X. Zhang, Synergistic effect between metal–nitrogen–carbon sheets and NiO nanoparticles for enhanced electrochemical water-oxidation performance, **Angew. Chem. Int. Ed. 2015, 54, 10530.**

5. S. Gadipelli and Z. X. Guo, Tuning of MOF-derived carbon with high activity, nitrogen functionality and yield – a case for superior CO_2 capture, **ChemSusChem, 2015, 8, 2123**.
6. G. Srinivas, C. A. Howard, S. M. Bennington, N. T. Skipper and M. Ellerby, Effect of hydrogenation on structure and superconducting properties of CaC_6, **J. Mater. Chem., 2009, 19, 5239.**
7. G. Srinivas, A. Lovell, N. T. Skipper, S. M. Bennington, K. Zynep and R. I. Smith, Ammonia absorption in calcium graphite intercalation compounds: *in situ* neutron diffraction, Raman spectroscopy and magnetization, **Phys. Chem. Chem. Phys., 2010, 12, 6253.**
8. http://srdata.nist.gov/xps/elm_in_comp_res.aspx?elm1=Co.
9. http://xpssimplified.com/elements/cobalt.php.
10. M. C. Biesinger, B. P. Payne, A. P. Grosvenor, L. W.M. Lau, A. R. Gerson and R. St.C. Smart, Resolving surface chemical states in XPS analysis of first row transition metals, oxides and hydroxides: Cr, Mn, Fe, Co and Ni, **Appl. Surf. Sci. 2011, 257, 2717**.
11. W. Chaikittisilp, N. L. Torad, C. Li, M. Imura, N. Suzuki, S. Ishihara, K. Ariga and Y. Yamauchi, Synthesis of nanoporous carbon–cobalt-oxide hybrid electrocatalysts by thermal conversion of metal–organic frameworks, **Chem. Eur. J. 2014, 20, 4217.**
12. S. Gadipelli, W. Travis, W. Zhou and Z. Guo, A thermally derived and optimized structure of ZIF-8 with giant enhancement in CO_2 uptake, **Energy Environ. Sci., 2014, 7, 2232.**
13. T. Y. Ma, J. L. Cao, M. Jaroniec and S. Z. Qiao, Interacting carbon nitride and titanium carbide nanosheets for high-performance oxygen evolution, **Angew. Chem. Int. Ed., 2015, 55, 1138.**
14. S. Guo, S. Zhang, L. Wu and S. Sun, Co/CoO nanoparticles assembled on graphene for electrochemical reduction of oxygen, **Angew. Chem. 2012, 124, 11940**.
15. K. Xie, J. Masa, E. Madej, F.i Yang, P. Weide, W. Dong, M. Muhler, W. Schuhmann and W. Xia, Co_3O_4–MnO_2–CNT hybrids synthesized by HNO_3 vapor oxidation of catalytically grown CNTs as OER electrocatalysts, **ChemCatChem, 2015, 7, 3027.**

b. Literature of MOF/ZIF- alone derived NPCs

1. S. Ma, G. A. Goenaga, A. V. Call and D.-J. Liu, Cobalt imidazolate framework as precursor for oxygen reduction reaction electrocatalysts, **Chem. Eur. J. 2011, 17, 2063.**
2. X. Wang, J. Zhou, H. Fu, W. Li, X. Fan, G. Xin, J. Zheng and X. Li, MOF derived catalysts for electrochemical oxygen reduction, **Mater. Chem. A 2014, 2, 14064**.
3. N. L. Torad, R. R. Salunkhe, Y. Li, H. Hamoudi, M. Imura, Y. Sakka, C.-C. Hu and Y. Yamauchi, Electric double-layer capacitors based on highly graphitized nanoporous carbons derived from ZIF-67, **Chem. Eur. J. 2014, 20, 7895**.
4. D. Zhu, L. Li, J. Cai, M. Jiang, J. Qi and X. Zhao, Nitrogen-doped porous carbons from bipyridine based metal-organic frameworks: electrocatalysis for oxygen reduction reaction and Pt-catalyst support for methanol electrooxidation, **Carbon 2014, 79, 544.**

5. F. Zheng, Y. Yang and Q. Chen, High lithium anodic performance of highly nitrogen-doped porous carbon prepared from a metal-organic framework, **Nat. Commun. 2014, 5, 5261.**
6. S. Zhao, H. Yin, L. Du, L. He, K. Zhao, L. Chang, G. Yin, H. Zhao, S. Liu and Z. Tang, Carbonized nanoscale metal-organic frameworks as high performance electrocatalyst for oxygen reduction reaction, **ACSNano 2014, 8, 12660.**
7. J. Sanetuntikul and S. Shanmugam, Prussian blue-carbon hybrid as a non-precious electrocatalyst for the oxygen reduction reaction in alkaline medium, **Electrochimica Acta 2014, 119, 92.**
8. L. Zhang, Z. Su, F. Jiang, L. Yang, J. Qian, Y. Zhou, W. Li and M. Hong, Highly graphitized nitrogen-doped porous carbon nanopolyhedra derived from ZIF-8 nanocrystals as efficient electrocatalysts for oxygen reduction reactions, **Nanoscale 2014, 6, 6590**.
9. W. Chaikittisilp, N. L. Torad, C. Li, M. Imura, N. Suzuki, S. Ishihara, K. Ariga and Y. Yamauchi, Synthesis of nanoporous carbon–cobalt-oxide hybrid electrocatalysts by thermal conversion of metal–organic frameworks, **Chem. Eur. J. 2014, 20, 4217**.

c. Literature of MOF/ZIF-derived NPCs with the addition of extra functional precursor at pre-/post synthesis treatment

1. A. Aijaz, N. Fujiwara and Q. Xu, From metal−organic framework to nitrogen-decorated nanoporous carbons: high CO_2 uptake and efficient catalytic oxygen reduction, **J. Am. Chem. Soc. 2014, 136, 6790**.
2. P. Su, H. Xiao, J. Zhao, Y. Yao, Z. Shao, C. Li and Q. Yang, Nitrogen-doped carbon nanotubes derived from Zn–Fe-ZIF nanospheres and their application as efficient oxygen reduction electrocatalysts with in situ generated iron species, **Chem. Sci. 2013, 4, 2941**.
3. D. Y. Chung, K. J. Lee, S.-H. Yu, M. Kim, S. Y. Lee, O.-H. Kim, H.-J. Park and Y.-E. Sung, Alveoli-inspired facile transport structure of N-doped porous carbon for electrochemical energy applications, **Adv. Energy Mater. 2015, 5, 1401309.**
4. K. Strickland, E. Miner, Q. Jia, U. Tylus, N. Ramaswamy, W. Liang, M.-T. Sougrati, F. Jaouen and S. Mukerjee, Highly active oxygen reduction non-platinum group metal electrocatalyst without direct metal–nitrogen coordination, **Nat. Commun. 2015, 6, 7343.**
5. Y.-Z. Chen, C. Wang, Z.-Y. Wu, Y. Xiong, Q. Xu, S.-H. Yu and H.-L. Jiang, From bimetallic metal-organic framework to porous carbon: high surface area and multicomponent active dopants for excellent electrocatalysis, **Adv. Mater. 2015, 27, 5010**.
6. D. Zhao, J.-L. Shui, L. R. Grabstanowicz, C. Chen, S. M. Commet, T. Xu, J. Lu and D.-J. Liu, Highly efficient non-precious metal electrocatalysts prepared from one-pot synthesized zeolitic imidazolate frameworks, **Adv. Mater. 2014, 26, 1093.**
7. P. Zhang, F. Sun, Z. Xiang, Z. Shen, J. Yun and D. Cao, ZIF-derived in situ nitrogen-doped porous carbons as efficient metal-free electrocatalysts for oxygen reduction reaction, **Energy Environ. Sci. 2014, 7, 442.**
8. X. Li, Y. Fang, X. Lin, M. Tian, X. An, Y. Fu, R. Li, J. Jin and J. Ma, MOF derived Co_3O_4 nanoparticles embedded in N-doped mesoporous carbon layer/MWCNT hybrids: extraordinary bi-functional electrocatalysts for OER and ORR, **J. Mater. Chem. A, 2015, 3, 17392.**

9. B. Chen, R. Li, G. Ma, X. Gou, Y. Zhu and Y. Xia, Cobalt sulfide/N,S codoped porous carbon core–shell nanocomposites as superior bifunctional electrocatalysts for oxygen reduction and evolution reactions, **Nanoscale, 2015, 7, 20674.**
10. J.-S. Li, S.-L. Li, Y.-J. Tang, M. Han, Z.-H. Dai, J.-C. Bao and Y.-Q. Lan, Nitrogen-doped Fe/Fe_3C@graphitic layer/carbon nanotube hybrids derived from MOFs: efficient bifunctional electrocatalysts for ORR and OER, **Chem. Commun. 2015, 51, 2710.**
11. T. Palaniselvam, B. P. Biswal, R. Banerjee and S. Kurungot, Zeolitic imidazolate framework (ZIF)-derived, hollow-core, nitrogen-doped carbon nanostructures for oxygen-reduction reactions in PEFCs, **Chem. Eur. J. 2013, 19, 9335**.
12. S. Pandiaraj, H. B. Aiyappa, R. Banerjee and S. Kurungot, Post modification of MOF derived carbon via g-C_3N_4 entrapment for an efficient metal-free oxygen reduction reaction, **Chem. Commun. 2014, 50, 3363**.
13. P. Pachfule, V. M. Dhavale, S. Kandambeth, S. Kurungot and R. Banerjee, Porous-organic-framework-templated nitrogen-rich porous carbon as a more proficient electrocatalyst than Pt/C for the electrochemical reduction of oxygen, **Chem. Eur. J. 2013, 19, 974.**
14. J.-S. Li, S.-L. Li, Y.-J. Tang, K. Li, L. Zhou, N. Kong, Y.-Q. Lan, J.-C. Bao and Z.-H. Dai, Heteroatoms ternary-doped porous carbons derived from MOFs as metal-free electrocatalysts for oxygen reduction reaction, **Sci. Rep. 2014, 4, 5130.**
15. W. Zhang, Z.-Y. Wu, H.-L. Jiang and S.-H. Yu, Nanowire-directed templating synthesis of metal−organic framework nanofibers and their derived porous doped carbon nanofibers for enhanced electrocatalysis, **J. Am. Chem. Soc. 2014, 136, 14385.**
16. A. Kong, Q. Lin, C. Mao, X. Bu and P. Feng, Efficient oxygen reduction by nanocomposites of heterometallic carbide and nitrogen-enriched carbon derived from the cobalt-encapsulated indium–MOF, **Chem. Commun. 2014, 50, 15619.**
17. Z. Xiang, D. Wang, Y. Xue, L. Dai, J.-F. Chen and D. Cao, PAF-derived nitrogen-doped 3D carbon materials for efficient energy conversion and storage, **Sci. Rep. 2015, 5, 8307**.
18. J. Xi, Y. Xia, Y. Xu, J. Xiao and S. Wang, (Fe,Co)@nitrogen-doped graphitic carbon nanocubes derived from polydopamine encapsulated metal–organic frameworks as a highly stable and selective non-precious oxygen reduction electrocatalyst, **Chem. Commun. 2015, 51, 10479**.
19. J. Li, Y. Chen, Y. Tang, S. Li, H. Dong, K. Li, M. Han, Y.-Q. Lan, J. Bao and Z. Dai, Metal–organic framework templated nitrogen and sulfur co-doped porous carbons as highly efficient metal-free electrocatalysts for oxygen reduction reactions, **J. Mater. Chem. A 2014, 2, 6316**.
20. E. Proietti, F. Jaouen, M. Lefèvre, N. Larouche, J. Tian, J. Herranz and J.-P. Dodelet, Iron-based cathode catalyst with enhanced power density in polymer electrolyte membrane fuel cells, **Nat. Commun. 2011, 2, 416.**
21. H. B. Wu, S. Wei, L. Zhang, R. Xu, H. H. Hng, X. W. Lou, Embedding sulfur in MOF-derived microporous carbon polyhedrons for lithium–sulfur batteries, **Chem. Eur. J. 2013, 19, 10804.**
22. H. Hu, L. Han, M. Yu, Z. Wang and X. W. Lou, Metal–organic-framework-engaged formation of Co nanoparticle-embedded carbon@Co_9S_8 double-shelled nanocages for efficient oxygen reduction, **Energy Environ. Sci., 2016, 9, 107**.

d. Literature of MOF/ZIF-derived NPCs with template directed or GO addition

1. W. Zhang, Z.-Y. Wu, H.-L. Jiang and S.-H. Yu, Nanowire-directed templating synthesis of metal−organic framework nanofibers and their derived porous doped carbon nanofibers for enhanced electrocatalysis, **J. Am. Chem. Soc. 2014, 136, 14385.**
2. H. Zhong, J. Wang, Y. Zhang, W. Xu, W. Xing, D. Xu, Y. Zhang and X. Zhang, ZIF-8 derived graphene-based nitrogen-doped porous carbon sheets as highly efficient and durable oxygen reduction electrocatalysts, **Angew. Chem. Int. Ed. 2014, 53, 14235.**
3. J. Wei, Y. Hu, Z. Wu, Y. Liang, S. Leong, B. Kong, X. Zhang, D. Zhao, G. P. Simone and H. Wang, A graphene-directed assembly route to hierarchically porous Co–Nx/C catalysts for high performance oxygen reduction, **J. Mater. Chem. A 2015, 3, 16867.**
4. J. Wei, Y. Hu, Y. Liang, B. Kong, J. Zhang, J. Song, Q. Bao, G. P. Simon, S. P. Jiang and H. Wang, Nitrogen-doped nanoporous carbon/graphene nano-sandwiches: synthesis and application for efficient oxygen reduction, **Adv. Funct. Mater. 2015, 25, 5768**.
5. Y. Hou, T. Huang, Z. Wen, S. Mao, S. Cui and J. Chen, Metal-organic framework-derived nitrogen-doped core-shell-structured porous Fe/Fe_3C@C nanoboxes supported on graphene sheets for efficient oxygen reduction reactions, **Adv. Energy Mater. 2014, 4, 1400337**.

e. Literature of MOF/ZIF-derived NPCs with acid washing

1. A. Aijaz, N. Fujiwara and Q. Xu, From metal−organic framework to nitrogen-decorated nanoporous carbons: high CO_2 uptake and efficient catalytic oxygen reduction, **J. Am. Chem. Soc. 2014, 136, 6790**.
2. D. Y. Chung, K. J. Lee, S.-H. Yu, M. Kim, S. Y. Lee, O.-H. Kim, H.-J. Park and Y.-E. Sung, Alveoli-inspired facile transport structure of N-doped porous carbon for electrochemical energy applications, **Adv. Energy Mater. 2015, 5, 1401309.**
3. Y.-Z. Chen, C. Wang, Z.-Y. Wu, Y. Xiong, Q. Xu, S.-H. Yu and H.-L. Jiang, From bimetallic metal-organic framework to porous carbon: high surface area and multicomponent active dopants for excellent electrocatalysis, **Adv. Mater. 2015, 27, 5010**.
4. W. Xia, R. Zou, L. An, D. Xia and S. Guo, A metal–organic framework route to in situ encapsulation of Co@Co_3O_4@C core@bishell nanoparticles into a highly ordered porous carbon matrix for oxygen reduction, **Energy Environ. Sci. 2015, 8, 568**.
5. D. Zhao, J.-L. Shui, L. R. Grabstanowicz, C. Chen, S. M. Commet, T. Xu, J. Lu and D.-J. Liu, Highly efficient non-precious metal electrocatalysts prepared from one-pot synthesized zeolitic imidazolate frameworks, **Adv. Mater. 2014, 26, 1093.**
6. J. Tang, R. R. Salunkhe, J. Liu, N. L. Torad, M. Imura, S. Furukawa and Y. Yamauchi, Thermal conversion of core−shell metal−organic frameworks: a new method for selectively functionalized nanoporous hybrid carbon, **J. Am. Chem. Soc. 2015, 137, 1572.**
7. T. Palaniselvam, B. P. Biswal, R. Banerjee and S. Kurungot, Zeolitic imidazolate framework (ZIF)-derived, hollow-core, nitrogen-doped carbon nanostructures for oxygen-reduction reactions in PEFCs, **Chem. Eur. J. 2013, 19, 9335**.
8. J. Wei, Y. Hu, Z. Wu, Y. Liang, S. Leong, B. Kong, X. Zhang, D. Zhao, G. P. Simone and H. Wang, A graphene-directed assembly route to hierarchically porous Co–Nx/C catalysts for high performance oxygen reduction, **J. Mater. Chem. A 2015, 3, 16867.**
9. J. Wei, Y. Hu, Y. Liang, B. Kong, J. Zhang, J. Song, Q. Bao, G. P. Simon, S. P. Jiang and H. Wang, Nitrogen-doped nanoporous carbon/graphene nano-sandwiches:

synthesis and application for efficient oxygen reduction, **Adv. Funct. Mater. 2015, 25, 5768**.
10. X. Zhao, H. Zhao, T. Zhang, X. Yan, Y. Yuan, H. Zhang, H. Zhao, D. Zhang, G. Zhu and X. Yao, One-step synthesis of nitrogen-doped microporous carbon materials as metal-free electrocatalysts for oxygen reduction reaction, **J. Mater. Chem. A 2014, 2, 11666**.
11. D. Zhao, J.-L. Shui, C. Chen, X. Chen, B. M. Reprogle, D. Wang and D.-J. Liu, Iron imidazolate framework as precursor for electrocatalysts in polymer electrolyte membrane fuel cells, **Chem. Sci. 2012, 3, 3200.**
12. B. Y. Xia, Y. Yan, N. Li, H. B. Wu, X. W. Lou and X. Wang, A metal–organic framework-derived bifunctional oxygen electrocatalyst, **Nat. Energy, 2016, 1, 15006**.

f. References for Simulations

1. G. Kresse and J. Furthmüller, Efficient iterative schemes for *ab initio* total-energy calculations using a plane-wave basis set, **Phys. Rev. B 1996, 54, 11169.**
2. P. E. Blöchl, Projector augmented-wave method, **Phys. Rev. B 1994, 50, 17953.**
3. G. A. Botton, S. Y. Savrasov, C. J. Humphreys and A. P. Sutton, **Phys. Rev. B, 1998, 57, 1505.**
4. K. J. Carroll, Z. J. Huba, S. R. Spurgeon, M. Qian, S. N. Khanna, D. M. Hudgins, M. L. Taheri and E. E. Carpenter, Magnetic properties of Co_2C and Co_3C nanoparticles and their assemblies, **Appl. Phys. Lett. 2012, 101, 012409.**
5. D. Jakob and G. Kotliar, Orbital selective and tunable Kondo effect of magnetic adatoms on graphene: correlated electronic structure calculations, **Phys. Rev. B. 2010, 82, 085423.**
6. S. Grimme, Semiempirical GGA-type density functional constructed with a long-range dispersion correction, **J. Comput. Chem. 2006, 27, 1787.**
7. J. K. Nørskov, J. Rossmeisl, A. Logadottir, L. Lindqvist, J. R. Kitchin, T. Bligaard and H. Jónsson, Origin of the overpotential for oxygen reduction at a fuel-cell cathode, **J. Phys. Chem. B 2004, 108, 17886.**
8. A. T. Raji, E. B.Lombardi, Stability, magnetic and electronic properties of cobalt–vacancy defect pairs in graphene: a first-principles study, **Physica B 2015, 464, 28.**
9. Y. Jiao, Y. Zheng, M. Jaroniec and S. Z. Qiao, Origin of the electrocatalytic oxygen reduction activity of graphene-based catalysts: a roadmap to achieve the best performance, **J. Am. Chem. Soc., 2014, 136, 4394**.
10. W. Tang, E. Sanville and G. Henkelman A grid-based Bader analysis algorithm without lattice bias, **J. Phys.: Condens. Matter, 2009, 21, 084204.**